RHODES UNIVERSITY

Where leaders learn

A mineralogical, geochemical and metallogenic study of unusual Mn/Na/Ba assemblages at the footwall of conglomeratic iron-ore at farm *Langverwacht*, Northern Cape Province of South Africa.

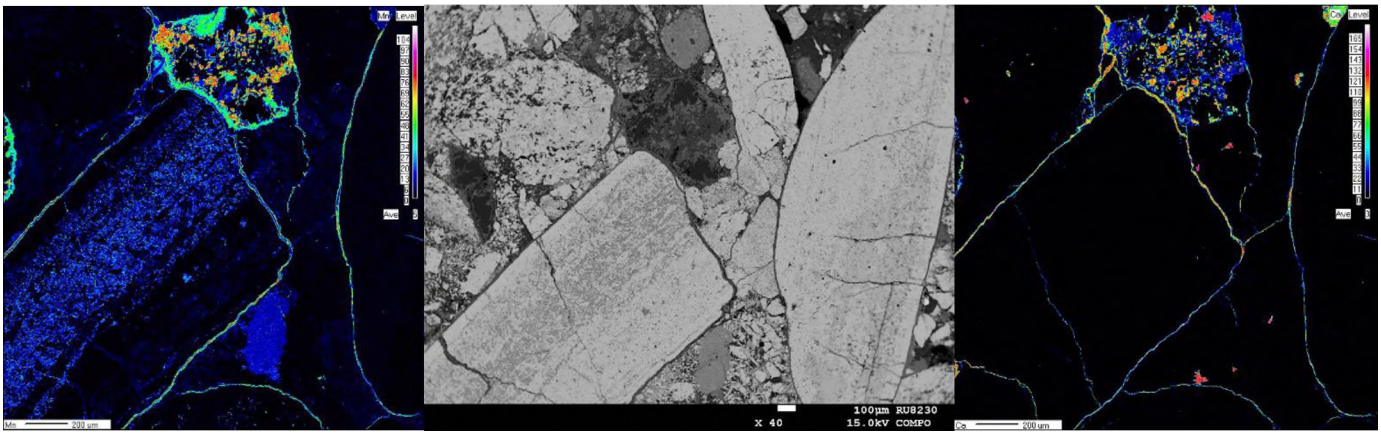

James Rodney Bursey

Thesis submitted in fulfilment of the requirements for the degree of

MASTER OF SCIENCE

in the Department of Geology, Rhodes University.

Submitted in January 2018.

Supervised by: Prof Harilaos Tsikos

RHODES GEOLOGY

Abstract

The Postmasburg Manganese Field (PMF), located in the Northern Cape province of South Africa, plays host to significant deposits of iron and manganese that have been utilized since their discovery in 1922 by Captain L.T. Shone. Further afield, lies the massive high-grade manganese deposit of the Kalahari Manganese Field (KMF), which drew attention away from the PMF after its discovery. These deposits are not limited to iron and manganese ore, but contain significant assemblages of alkali-rich rocks – which is the focus of this study.

The existence of alkali-rich assemblages beneath conglomeratic iron-ore on farm *Langwervacht*, has come under investigation in this study, and in particular, the enrichment of these rocks in Ba, Na and Mn. Petrographic analysis of the clast-supported conglomerate unit (ore-zone), has uncovered the presence of vugs (up to 8mm across) which contain barite, K-feldspar and fluorapatite. In addition to this, the ore-zone of one of the three boreholes contains late carbonate veins (kutnohorite), which travel along Fe-clast boundaries, and exploit clast-fractures and areas of weakness. Further down, within the 'enriched-zone' of alkalis, the mineralogy is more diverse – containing elevated concentrations of Ba, Na and Mn. Seventeen distinct minerals containing these three key elements have been identified – along with one solid-solution series in the form of hollandite-coronadite. The existence of minerals such as natrolite, aegirine, albite, banalsite, barite, serandite, celsian and hollandite-coronadite are indicative of hydrothermal activity having influenced these rocks.

Bulk-geochemistry was used to compare the major and trace elements of each borehole and the associated units. Both the trace elements and the REE's from the ore-zone are enriched by an average of 5-10x relative to the BIF standard used – which immediately suggests an influx of elements. Compared to PAAS (Post Archaean Australian Shales), the ore-zone REE's are slightly depleted, but more importantly the profiles are very similar to that of the Mapedi shales achieved in previous studies. This result points towards a strong shale influence in the ore-zone protolith. Expectedly, many of the enriched-zone trace elements and REE's show far greater enrichment than what is observed in the ore-zone. Trace and Rare Earth Element profiles between the ore-zone and the enriched-zone are, however, generally correlative, with profiles reflecting similar enrichments and depletions for a given element – even within different rock units. This suggests that the hydrothermal fluid has moved in a general upward direction,

reacting with host-rock units, and relinquishing elements carried in solution – wherever conditions have been favourable for the accommodation of these elements.

This study has shed light on the relationship between the ore-zone and the enriched-zone, and results suggest that the process of alkali enrichment is not directly related to the process of upgrading of the iron ores. This is due to the extent of the alkali-enrichment below the ore-zone, as well as enrichment factors in some trace elements being superior to that of Fe_2O_3 in the ore-zone. Hence, both of these zones have both been affected by a later hydrothermal fluid. The source of the fluid is likely a mature basinal brine, of oxidized, alkaline nature – which leached elements (Ba, K, Na, Pb, Ca) from older rocks, and carried them in solution. On a local-scale, this fluid has exploited areas of weakness in the form of fractures, less consolidated conglomeratic material and crosscutting veins. Manganese and iron has been remobilized on a local scale – producing secondary textures and partitioning into phases such as Mn-rich calcite and serandite.

Comparisons to other studies in the PMF and KMF have revealed very similar alkali-rich assemblages, bearing many of the same minerals observed in this study – even within more manganiferous deposits. These findings have led to suggestions of a possible regional-scale hydrothermal overprint, which may have imparted a similar geochemical signal over the entire region – with the assistance of faults and unconformities. Of course, proving this is no mean feat, but current work on the source of barium in barite, using Sr isotopes from samples across the region may shed light on the source of at least one key element of these deposits.

Declaration

I declare that this thesis, titled "A mineralogical, geochemical and metallogenic study of unusual Mn/Na/Ba assemblages at the footwall of conglomeritic iron-ore at farm *Langverwacht*, Northern Cape Province of South Africa" is my own work, and information from other publications is adequately referenced. This thesis is being submitted in fulfilment for the Bachelor of Science in Master's degree in the Department of Geology, Rhodes University.

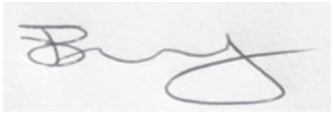

JAMES BURSEY

Table of Contents

Acknowledgements

A big thank you is extended to CIMERA for the funding of this project, and to Kumba for providing the samples. Next, I would like to thank my supervisor – Harilaos (Hari) Tsikos, for his unwavering support and guidance throughout the compilation of this project, as well as in previous years. His immense knowledge base, approachability, and friendly demeanor have made this project a pleasure – and it has been a privilege to get to know and work with such a remarkable supervisor! Hari is truly a pillar of strength in the Rhodes Geology Department.

I would like to thank Vuyokazi Nkayi, Ashleigh Goddard, Andrea King, Andile 'Chris' Pikoli, Thulani Royi, and Deon van Niekerk for their administrative and technical assistance at Rhodes University. Mareli Grobbelaar of Stellenbosch University is thanked for her assistance with the production of the XRF data used in this project. Thanks must go to Brenton Fairey for his help with processing the microprobe data.

I would like to thank my family for all their support. This thesis is dedicated to my parents, whose immense sacrifice has afforded me the opportunity to get to where I am today – I am forever grateful for that.

I would like to thank Ashleigh Bruce for her unconditional support during the development of this project. Mention must go to the Student Housemasters of St Andrew's Prep School, for their contribution to two awesome years during the development of this project – those memories will live with me forever! Lastly, I would like to thank the members of PRIMOR, with whom countless beverages and laughs were shared – together with geological discussion of course!

Chapter 1.

Introduction

The Northern Cape, and its respective Kalahari and Postmasburg Manganese Fields have long been a source of interest for the mining industry and academic fraternity alike – with the first journal publication of geological significance on the area being recorded in the year 1874, by the European explorer, G.W. Stow (Cairncross and Beukes, 2013). Mining in the Postmasburg Manganese Field (PMF) area would follow shortly after the discovery of manganese ores by Captain L.T. Shone in 1922 (Truter *et al.*, 1938; Gutzmer and Beukes, 1996). The initial boom was diluted in the 1980's, after attention turned to the high-grade ores of the Kalahari Manganese Field (KMF) and their economic potential.

The respective manganese fields mentioned above are not just rich in manganese, but iron too – the fourth most abundant crustal element. The iron was deposited over repeated sedimentary cycles, leading to the formation of large deposits. Although sedimentary rocks containing at least 15 wt % are considered by Boggs (2009) to be iron-rich, upgrading processes in the Northern Cape have significantly increased the commercial potential of the iron-ore in areas, many of which are actively mined today.

In the context of this study, the alkali-rich assemblage, which is located directly beneath a conglomeratic iron-ore body on farm *Langverwacht*, is the center of attention. This study aims to shed light on the processes which could lead to the formation of an alkali-assemblage of this nature being situated below iron-ore, and furthermore, to decipher what relationship (if any) exists between the ore-zone and the alkali-enriched-zone. The study area and borehole locations are displayed in Figure 1 below.

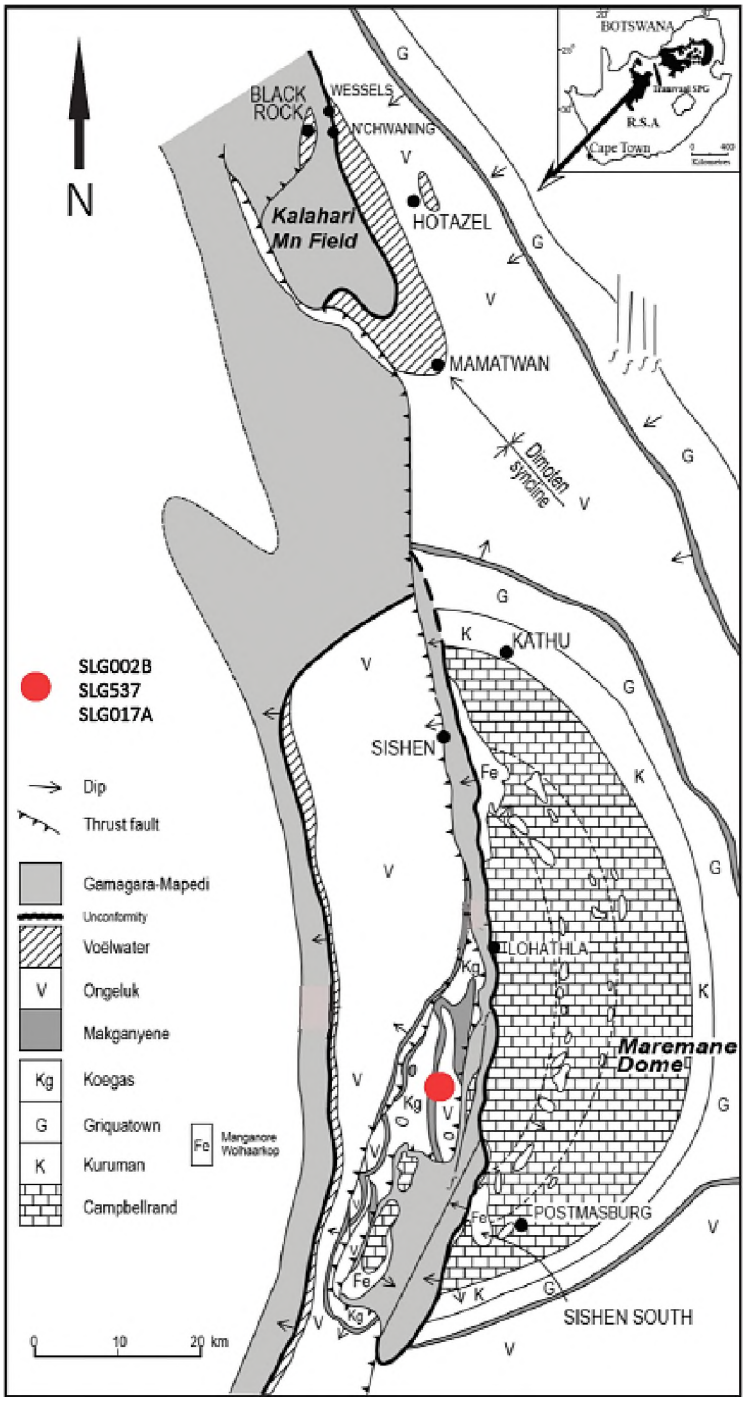

Figure 1: Regional map of the Transvaal Supergroup, including the locality of the 3 boreholes concerned in this study. (Modified after Moore *et al*. 2011).

1.1 Regional Geology

The Northern Cape Province of South Africa plays host to the well-documented Paleoproterozoic Transvaal Supergroup – which was deposited from 2.65-2.05Ga (Tsikos *et al.*, 2003). The Transvaal Supergroup is well preserved within the structure of the Kaapvaal Craton, an Archean tectonic unit which covers an area of roughly 1,200 km^2 (Tsikos *et al.*, 2003). The Transvaal Supergroup was initially deposited in a single sedimentary basin – reaching a total thickness of 12km in some areas, but has subsequently been split into two separate basins, by the introduction of basement rocks known as the Vryburg rise (Moore *et al*, 2001). This has produced two laterally correlative, but spatially separate basins, in the form of the Griqualand West and Transvaal basins – which occur to the east and west respectively.

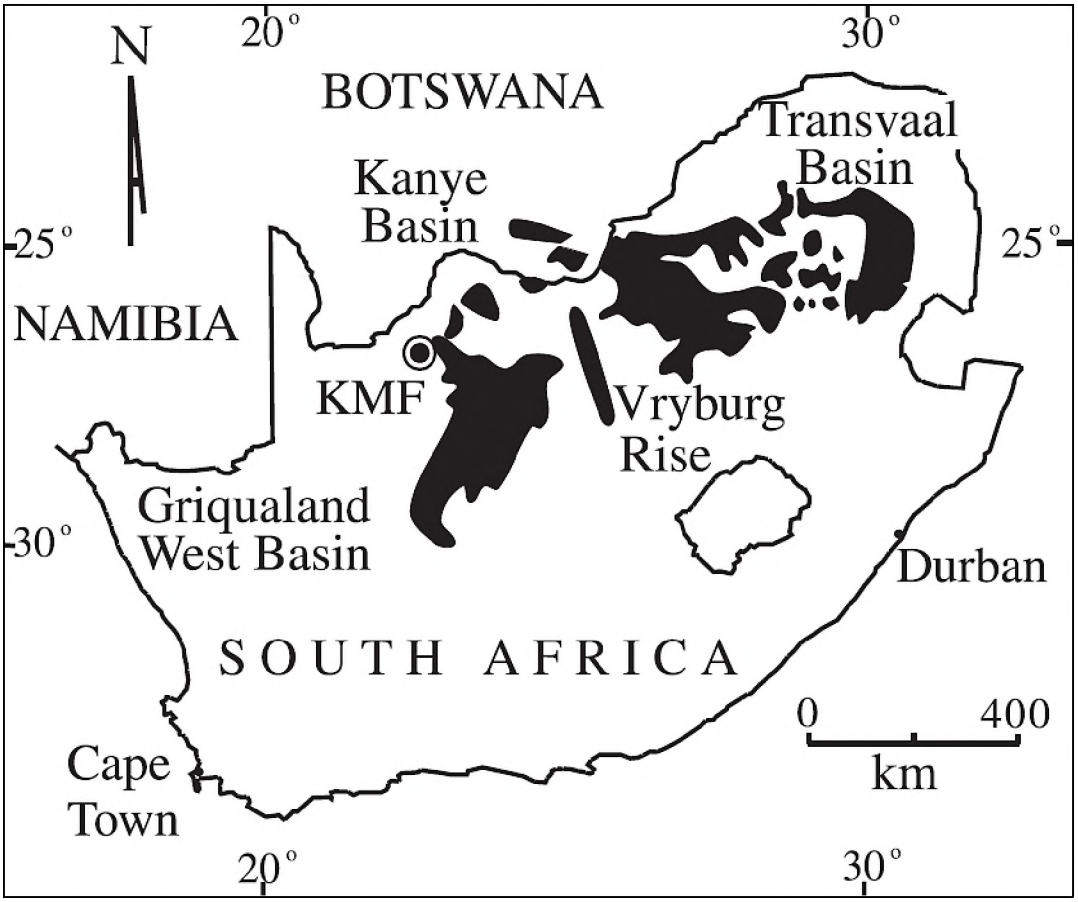

Figure 2: Map showing the separation of the Griqualand West Basin from the Transvaal Basin, with the Vryburg Rise in between. (From Tsikos *et al*, 2003)

The Griqualand West basin is comprised of two Supergroups, namely: the Transvaal Supergroup and the overlying Olifantshoek Supergroup. According to Holland and Beukes (1990), metamorphic conditions in this region have been limited to temperatures of 170 C° or less, and pressures of approximately 2 kbar.

The tectonic evolution of the area is relatively complex, and the formation of the Maremane Dome is arguably the most prominent indication of this. This dome is associated with the Kalahari orogeny, which lasted from 2220-2100 Ma (Alchin *et al.,* 2008; Papadopoulos, 2016). This event was characterized by east-west compression of the crustal material, resulting in extensive folding, erosion and uplift in the region (Alchin *et al.,* 2008). Following the Kalahari orogeny, erosion of folded strata resulted in the regional unconformity between the Transvaal Supergroup and the overlying Olifantshoek sediments (Grobbelaar *et al*., 1995). The Blackridge Thrust is another important feature of the tectonic history of the region, and developed as a result of the Kheis orogenic event, which deformed the Kheis Belt over the time period from 1830-1730 Ma (Tsikos *et al.*, 2003). The Blackridge thrust has a total displacement of at least 35km (Beukes and Smit, 1987; Gutzmer and Beukes, 1996b) and is responsible for duplicating certain strata of the Olifantshoek Supergroup (Grobbelaar *et al.,*1995).

The stratigraphy of the Transvaal Supergroup is summarized in Table 1 below, where the various formations and their predominant lithologies are highlighted.

Table 1: Stratigraphy of the Palaeoproterozoic Transvaal Supergroup (modified after Tsikos and Moore, 1997; Papadopoulos, 2016)

Supergroup	Group	Subgroup	Formation	Predominant Lithology
Transvaal	Postmasburg	Voëlwater	Mooidraai	Chert-baring carbonate
			Hotazel	BIF containing Mn ore
			Ongeluk	Andesitic pillow lavas
			Makganyene	Diamictite
	Ghaap	Koegas		Mudstones and wackes
		Asbestos Hills	Griquatown	Clastic BIF
			Kuruman	Microbanded BIF
		Campbellrand	Gamohaan	Carbonates ± shale, chert
			Kogelbeen	
			Klippen	
			Papkuil	
			Klipfonteinheuwel	
			Fairfield	
			Rievilo	
			Monteville	
		Schmidstdrif		Mudstones and wackes

1.2 Iron ore in the Transvaal Supergroup

South Africa is blessed with several high-grade BIF hosted deposits of chemical sedimentary origin, which formed over the period from ~2.6-2.2 Ga (Eriksson et al., 2006). However, most BIF deposits do not fall under the high-grade classification, at ~43 wt.% Fe_2O_3, and ~47 wt.% SiO_2, and therefore require processes of upgrading to achieve high grade status of >60 wt.% Fe (Smith and Beukes, 2006).

There are three main epigenetic processes which are considered to be responsible for the upgrading of the worlds BIF deposits, and these include: hydrothermal, supergene and supergene-modified hydrothermal deposits (Smith and Beukes, 2006). Well-known examples of hydrothermally upgraded BIF include the enormous Mt Tom Price deposit in Western Australia, while in South Africa, Thabazimbi is the closest equivalent. The development of hydrothermal iron ore is considered to be largely dependent on fault structures acting as a conduit for fluid flow, after which, two main processes are required for the upgrading process to occur. 1)

Leaching of silica from BIF by warm, highly saline fluids. 2) Recrystallization of iron-rich minerals to specularite and martite, as a result of moderately warm, low salinity, oxidized fluids (Taylor *et al*. 2001).

Previous experiments on the temperatures of the associated fluids required for leaching and upgrading of the BIF material have produced a relatively narrow range, from 150-320°C (Taylor *et al*. 2001). According to Beukes *et al*. (2003) the $\delta^{18}O$ of fluids involved has been estimated at -2‰ relative to SMOW, which suggests that the hydrothermal fluids linked to the upgrading of BIF are of meteoric origin, and have not interacted with silicate rocks.

The supergene-modified hydrothermal type is a classification given to deposits which are typically hydrothermal in nature, but have later experienced a significant supergene overprint – which has resulted in a large upgrade of the iron ore. These deposit types are typically comprised of soft, saprolitic ore, which overlies hydrothermally developed, harder, massive or laminated hematite ore (Dalstra and Guedes, 2004). An example of the supergene-modified hydrothermal type is the Noamundi deposit of India, whereby the supergene overprint is considered to have played a crucial role in upgrading the deposit in terms of both grade and tonnage (Dalstra and Guedes, 2004).

Although there remains debate around the genesis of the iron ores associated with the Maremane Dome in the Northern Cape, generally, they are considered to be of supergene origin. The Maremane Dome is a prominent regional anticlinal structure of the PMF, which is dominated by dolomitic carbonate rocks of the Campbellrand Subgroup, but also contains iron formations of the Asbesheuwels Subgroup, and manganese deposits that are karstic in nature (Moore *et al*, 2011; Costin *et al*, 2011). At present, there are four main mines which produce the bulk of South Africa's BIF hosted iron ore – all of which are located within the Maremane Dome. These include the Sishen and Khumani mines along the North of the Maremane Dome, and the Beeshoek and Kholomela mines in the South (Smith and Beukes, 2006). These four mines produced a total of 76.9 million tonnes of high grade hematite in 2014, while Thabazimbi produced 1.1 million tonnes in the same year (Smith and Beukes, 2006).

According to Smith and Beukes (2006), all of the iron deposits of the Maremane Dome are linked to the development of a regional erosional unconformity, referred to as either the pre-Gamagara or the Mapedi unconformity – which separates the Transvaal Supergroup from the

overlying Olifantshoek Supergroup. This unconformity is well-developed across the entire Griqualand West area, and is easily identifiable by the lateritic weathering profile observed in the rocks directly below it (Smith and Beukes, 2006). The unconformity is considered to have formed over the period 2.2-2.0 Ga. Folding and faulting prior to the development of the erosional unconformity resulted in the unconformity transecting a number of different lithologies, all of which were subsequently overlain by the deposition of the Gamagara/Mapedi red beds (Smith and Beukes, 2006).

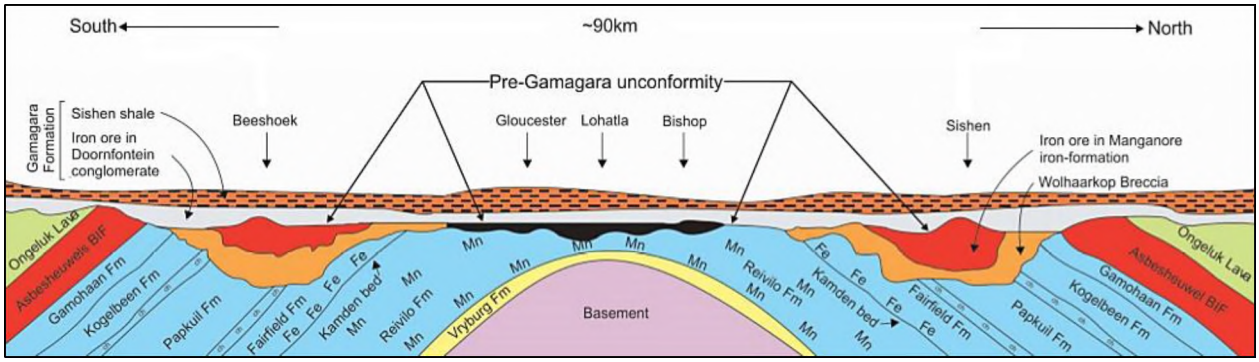

Figure 3: Cross-section through Maremane Dome. Modified after Smith and Beukes, (2006).

All of the associated high-grade hematite iron ores are located beneath the Gamagara/Mapedi unconformity, and have only developed in areas where the unconformity has intersected BIF (Smith and Beukes, 2006). Therefore, this is seen as proof for the supergene related upgrading of the BIF in these deposits. There are three main Iron Formations involved, namely: 1) Kuruman and Griquatown Iron Formations of the Asbesheuwels Subgroup. 2) Rooinekke Iron Formation of the Koegas Subgroup. 3) Hotazel Iron Formation of the Voëlwater Subgroup (Smith and Beukes, 2006). The supergene related ores typically consist of massive, laminated and brecciated iron ores. Large to super large deposits are constricted to areas where the Asbesheuwels Subgroup has slumped into karstic structures developed in the underlying dolomites – otherwise referred to as the Manganore Iron Formation (Beukes, 1978). Outside of the karstic slump structures, high-grade hematite iron ore beds are limited to just 1-2m thick (Smith and Beukes, 2006).

Further evidence for the supporting the supergene enrichment interpretation of these deposits is provided by Evans *et al.* (2001) who has determined that the ores were formed near the equator,

where warmer, more humid and tropical conditions would have favoured the processes of supergene enrichment.

1.3 Postmasburg Manganese Field

The samples used in this study are from the Western Belt of the Postmasburg Manganese Field, and therefore it is important to highlight some key aspects of this area and what is currently understood about this area, in terms of tectonic activity and processes of ore formation.

The PMF is located between the towns of Postmasburg and Kathu, and is strongly associated with the Maremane Dome. Initially, the PMF was South Africa's most important resource of manganese – until it was succeeded by the subsequent discovery and large-scale exploitation of the giant Kalahari Manganese Field (Gutzmer and Beukes, 1996b). As a result, current day mining of the PMF occurs on a relatively small scale (Gutzmer and Beukes, 1996b).

The PMF consists of two belts, which trend broadly N-S over the Maremane Dome, covering a distance of 65km (De Villiers, 1960; Gutzmer and Beukes, 1996b, Astrip and Tsikos, 1998; Costin *et al*, 2011). These two belts are mineralogically distinct from one another, and have been separated on the basis of their mineralogical composition and geological setting into the Western Belt of ferruginous ores, and the Eastern Belt of siliceous ores (Gutzmer and Beukes, 1996b). However, a third type of ore, which encompasses features of both the Eastern and Western Belts ('mixed-type') has been described in areas where these two belts meet – such as Rust-en-Vrede and King in the North (De Villiers, 1960; von Plehwe-Leisen and Klemm, 1995; Gutzmer and Beukes, 1996b). All three ore types occur within karstic sinkholes of the Campbellrand Group dolomites, but are highly variable in terms of size, shape and stratigraphy (Plehwe-Leisen and Klemm, 1995).

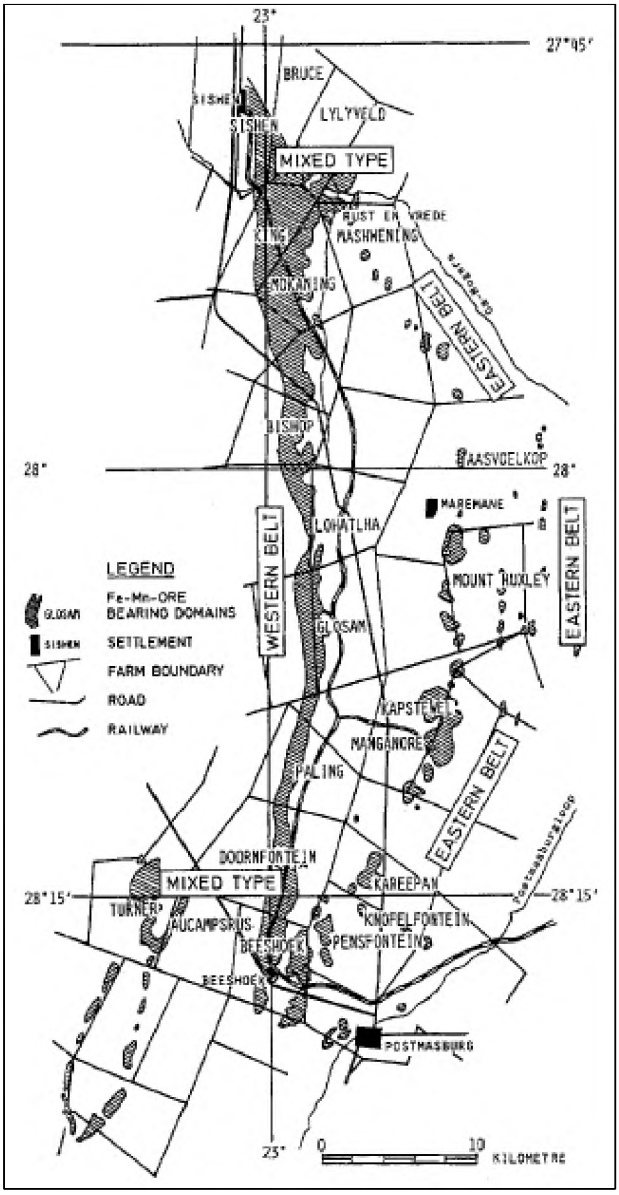

Figure 4: Sketch map of distribution on the three ore types in the PMF (From Leisen, 1987).

Evidently, the Eastern and Western Belts, and their associated characteristics are a function of the dome geometry. Their modes of formation and defining characteristics are presented in the sub-chapter below.

1.3.1 Genesis of the Eastern & Western Belt manganese ores

The manganese ores of the PMF are directly linked to the rising of the Maremane Dome above sea level – as a result of marine regression. Extended exposure of the dome, and subsequent erosion of the Ghaap Plateau dolomites (which contain significant concentrations of Mn and Fe (Gutzmer and Beukes, 1996a), resulted in the formation of karstic sinkholes (Plehwe-Leisen and Klemm, 1995). These karstic structures followed zones of tectonic weakness, typically along 10°, 50°and 150° directions (Plehwe-Leisen and Klemm, 1995).

The division of the ores into the Eastern and Western Belts is a function of the period of time that these areas experienced erosion for. According to Plehwe-Leisen and Klemm (1995), the Eastern Belt, which is comprised of the northern, southern and eastern portions of the Maremane Dome, was exposed up until Asbestos Hills time. During this period of exposure, erosion and karstification of the Fairfield Formation dolomites (which contain an average of 1-3 wt% MnO (Beukes, 1978) resulted in a Mn-rich residual ooze or 'wad' forming irregular shaped ore bodies at the base of the karstic structures (Gutzmer and Beukes, 1996a). The residual Mn ooze, coupled with silicified dolomite and chert chips make up what is known as the Wolhaarkop Breccia. Subsequent transgression kick-started the cycle of sedimentation once more, and the BIF strata of the Asbestos Hills subgroup were deposited (von Plehwe-Leisen and Klemm, 1995). In some areas, a collapse breccia commonly referred to as Blink-Klip Breccia formed as a result of collapsing of the karstic structures and the subsequent infilling of the overlying Asbestos Hills BIF strata (von Plehwe-Leisen and Klemm, 1995). Following an erosional unconformity, Fe-pebbles of the Doornfontein Conglomerate were deposited and conformably overlain by the deposition of the Gamagara Shales, which combine to form the Gamagara Shale Formation (Plehwe-Leisen and Klemm, 1995).

The Western Belt, however, was exposed for much longer than its eastern counterpart, and as a result, the dolomites were eroded as far down as the older Ulco Member – which contains 2-3 wt% Mn) (Beukes, 1978; von Plehwe-Leisen and Klemm, 1995). Due to being exposed for a longer period of time, the Asbestos Hills BIF sediments found in the Eastern Belt, are absent from the Western Belt. Instead, erosion in the Western Belt was succeeded by allochthonous deposition of the Doornfontein conglomerate into exposed karstic structures, followed by the

deposition of the Gamagara Shales (Plehwe-Leisen and Klemm, 1995). The Doornfontein conglomerate (interpreted by Van Schalkvyk and Beukes (1986) as an alluvial fan deposit) is thickest in the Northern and Southern ends of the Maremane Dome, where it is included as part of the iron reserve at Sishen and Beeshoek (Gutzmer and Beukes, 1996a).

1.3.2 The Eastern Belt

The ores of the Eastern Belt range mineralogically from fine-grained ores (partridgeite and braunite) to massive and vuggy bixbyite-rich ores (Costin *et al*, 2011). The matrix of the Wolhaarkop breccia is comprised of quartz, hematite and braunite, and transitions from being relatively more siliceous and ferruginous at the top, to more manganiferous at the base (Costin *et al*, 2011). Irregular shaped (lenticular to tabular) pockets of mineable manganese ore are typically located at the contact between the breccia and the dolomites (Boardman, 1964; Gutzmer and Beukes, 1996b) and according to de Villiers (1956), are particularly concentrated within steep cul-de-sacs along the karstic surface (Gutzmer and Beukes, 1996b). Smaller, lower grade ore bodies are located higher up in the breccia (Boardman, 1964; Gutzmer and Beukes, 1996b). Gutzmer and Beukes (1996b), have described the braunite dominated manganese ore as massive and dense, with grain size varying from fine to medium grained. Uncommonly, the ores can contain small vugs filled with cryptomelane and/or goethite, lined by euhedral braunite crystals (Gutzmer and Beukes, 1996b). According to Gutzmer and Beukes (1996b), the contact between the chert breccia and the manganese ore bodies is gradual, and typically characterized by an increase in manganiferous matrix to chert fragment ratio.

Von Plehwe-Leisen and Klemm (1995) describe a 'mixed type' ore in the Northern and Southern portions of the Maremane Dome. This ore type is considered to exhibit characteristics of both the Eastern and Western Belt – such as mineralization of the Wolhaarkop Breccia and shales, respectively (von Plehwe-Leisen and Klemm, 1995). However, Gutzmer and Beukes, (1996a), consider this ore type to be very similar to the Eastern Belt, and hence, do not recognize it as separate ore type altogether.

1.3.3 The Western Belt

Unlike like their Eastern counterparts, beds of the Western Belt are unexposed at the surface – which is a result of the Transvaal Supergroup being overlain by red beds of the Gamagara Formation – separated by a low angle unconformity (Gutzmer and Beukes 1996a). Due to the chert-free nature of the Ulco-Member dolomites, the Western Belt is silica deficient when compared to the Eastern Belt (von Plehwe-Leisen and Klemm, 1995). The Western Belt manganese ores are thickest within deep karstic structures, and reach a maximum thickness of around 17m at Lohatla – located in the central part of the Gamagara ridge (Gutzmer and Beukes, 1996a).

In a similar fashion to the Eastern Belt, the Mn-concentrations are highest near the contact with the dolomite, and decrease upwards into the Fe-rich shales (von Plehwe-Leisen and Klemm, 1995). According to von Plehwe-Leisen and Klemm (1995), two distinct periods of mineralization have occurred in the Western Belt – resulting in separate ore types. The most prominent is the basal manganese ore, which is residual and forms closest to the dolomite contact. The second involves well-layered manganese ores, which are strictly stratified, and occur higher up in the strata (von Plehwe- Leisen and Klemm, 1995). As one may expect, the dominant manganese mineral near to the dolomite contact is braunite, while bixbyite becomes more prevalent higher up in the layered ores – where the iron content is elevated due to the Fe-rich shales (von Plehwe-Leisen and Klemm, 1995). The second type is interpreted by von Plehwe-Leisen and Klemm (1995) to have formed as sea water precipitates, following the transgression of the Transvaal sea.

1.4 Hydrothermal activity and its influence on alkali-rich assemblages in the PMF and KMF

The widespread presence of alkali-rich minerals across the region has attracted attention from researchers for decades – particularly those interested in the potential effects that these fluids may have had on the ores of the region.

A number of rare silicates, reported to be linked to metasomatic processes of formation have been documented in the PMF. These include, norrishite, armbrusterite and the economically significant mineral sugilite (Moore *et al*, 2011). The presence of more common minerals, such as K-feldspar, aegirine, albite and serandite are further indications of metasomatic processes in this area.

The Kalahari Manganese Field is also not without its fair share of alkali-rich assemblages – reportedly of metasomatic origin. The origin, composition and nature of this fluid has been a subject of debate for some time. The similarity of the alkali assemblages at various locations has led to casual suggestions of a possible link between these deposits – in terms of their fluid source, on a regional scale – although it must be stressed that there is currently no evidence to support this. Furthermore, the possible effect of these fluids on the manganese and iron-ores of the region, and the associated processes of upgrading has yet to be clarified.

According to Gutzmer and Beukes (1995), the high-grade ores of the KMF, such as those located in the northernmost areas, are attributed to the influence of fault-controlled, saline, hydrothermal fluid circulation, which resulted in the leaching of carbonate material and subsequent upgrading of the Mn-ore (>44 wt% Mn). Gutzmer and Beukes (1997) have proposed that the interaction of the same saline fluid, is also responsible for the formation of a number of Na-bearing mineral species, such as sugilite and aegirine.

However, without dispelling the model of Gutzmer and Beukes (1995), Tsikos and Moore (2005) have subsequently analyzed the potential for the upgrading of the ore to have resulted from low-temperature, hydrothermal fluid-flow, concentrated along the unconformity between the Hotazel Formation and the overlying lesser quartzites of the Mapedi Formation (Olifantshoek Supergroup). According to Tsikos and Moore (2005), these two structurally controlled,

hydrothermal processes of ore-enrichment do not necessarily have to be mutually exclusive, and may have both played a part in the overall upgrading process.

The Hotazel Formation has reportedly undergone very low-grade metamorphism, and the mineral assemblage of the iron-formation typically consists of various amounts of quartz, magnetite, Fe^{2+} silicates and Ca-Fe-Mg carbonates (Tsikos *et al*, 2003). It is important to notice the absence of Na-bearing minerals in this unit. Therefore, according the Tsikos and Moore (2005), the presence of Na-containing silicates is indicative of an external source of Na in the form of a saline hydrothermal fluid.

Analysis of aegirine separate from the northernmost Kalahari field by Tsikos and Moore (2005), confirmed a pure-sodic end-member composition of the aegirine-augite series. Tsikos and Moore (2005) have postulated that the development of aegirine in this assemblage, in favour of other Na-bearing silicates, is determined by the presence of two pre-existing minerals, namely: quartz and hematite. This reaction in favour of producing aegirine is outlined below (after Likhoydov 1981):

$$4SiO_2 + Fe_2O_3 + 2NaCl + H_2O \longrightarrow 2NaFeSi_2O_6 + 2HCl$$

Quartz Hematite Aegirine

This reaction has the potential to occur under a wide range of temperatures (from as low as 200˚C (Decarreau *et al*, 2004)), and is sensitive to the concentration of NaCl as well as the pH of the reacting fluid (Tsikos and Moore, 2005; Likhoydov, 1981; McSwiggen *et al*, 1994).

According to Tsikos and Moore (2005), the formation of aegirine in the KMF would essentially hinge on the presence of hematite and quartz, and is likely to postdate earlier processes involving the leaching of carbonate material, and the residual enrichment of Fe and Mn as higher oxides. Due to the higher carbonate content of the manganese units (relative to the Fe-units), earlier leaching of carbonate material would have resulted in a more porous unit, thus facilitating the movement of Na-rich hydrothermal fluid, where it would later encounter quartz and hematite on the margins of the Mn-unit, and react to form aegirine (Tsikos and Moore, 2005). The process of fluid infiltration, and subsequent lateral movement through the Mn-units is depicted in Figure 5 below.

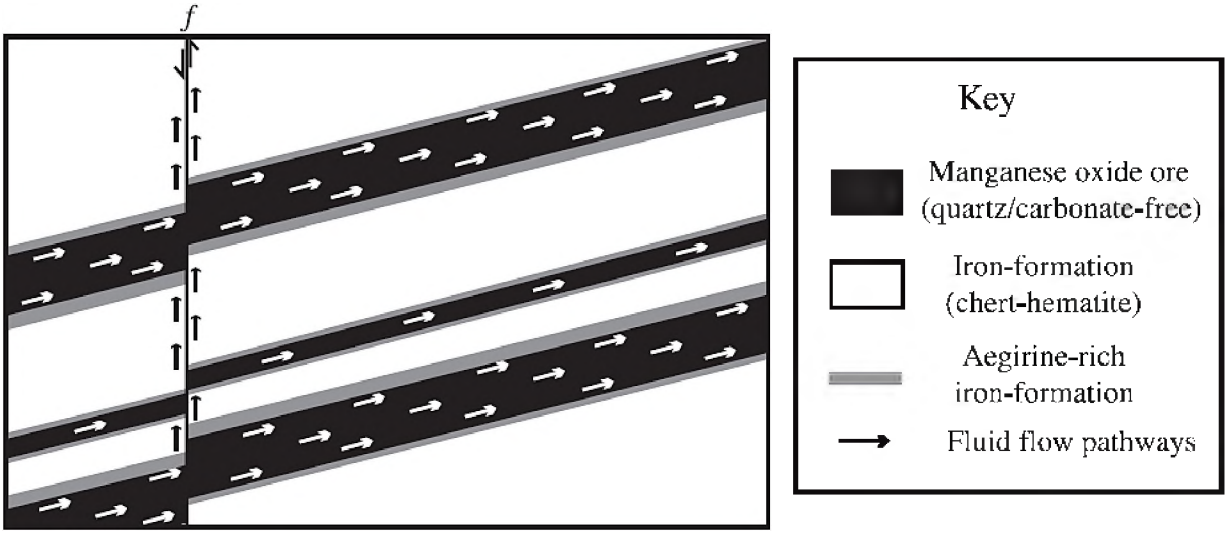

Figure 5: Mechanisms of Na-fluid infiltration and lateral movement, along porous Mn-units. (From Tsikos and Moore, 2005)

These findings are supported by similar assemblages further afield, such as the Devonian lacustrine deposits of Caithness, Scotland (Tsikos and Moore, 2005; Fortey & Michie, 1978), and the Proterozoic iron-formation of the Cuyana Range, Minnesota, USA (Tsikos and Moore, 2005; Grout, 1946; McSwiggen *et al*, 1994). In both of these assemblages, the formation of aegirine has been attributed to either Na-rich hydrothermal fluids, or NaCl-saturated fluids.

In addition to petrographic observations mentioned above, the traditional views on HFSE being relatively immobile indicators of parent-rock have been challenged by recent research undertaken in the region. Geochemical work by Land *et al*, (in review) has highlighted the relatively high concentration of HFSE in the shales of the Mapedi Formation – drawing to the conclusion that the HFSE must have been mobilized by a F-rich brine, able to transport high concentrations of HFSE in solution. This is supported by Shao-Yong *et al,* (2005), who discovered increasing evidence to suggest that these elements can become highly mobile within a number of geological environments, such as magmatic, metamorphic and hydrothermal systems.

A recent study by Fairey (2013), uncovered the presence of a number of exotic species in the context of manganese ores in the PMF. Minerals such as sugilite, armbrusterite, norrishite, arsenotokyoite, barytocalcite and the first African reporting of noelbensonite, paint a picture of the introduction of a number of key elements to these rocks, in order to form assemblages of this nature.

The study of Fairey (2013) is valuable as a means of comparing the alkali-rich assemblages in the context of manganese-ore vs iron-ore (current study) – and this will be in addressed in chapter 5.

1.5 Research aims and objectives

This study will use a variety of analytical techniques to gain insight into the mineralogy and geochemistry of the unusual, stratigraphically consistent Mn/Na/Ba-rich zone – occurring beneath the iron-ore *sensu-stricto* at farm site *Langverwacht*, –20km NW of Postmasburg in the Northern Cape Province of South Africa. The iron-ore intersected at farm *Langverwacht* is conglomeratic in nature, and is underlain by interbedded ferro-manganese, and matrix-supported conglomerate units. These rocks have clear potential to hold important clues concerning the genesis and fluid rock-interaction history of the iron-ores in the region, and may permit comparisons from geochemically similar mineral assemblages further afield at the Kalahari Manganese deposit. Thus, the objectives of the study include:

1. Mineralogical and geochemical characterization of ore-zone and alkali-enriched zone, with emphasis on Mn, Na and Ba-containing phases.
2. Use this information to gain insight into the origin and source of the fluid, including mechanisms of local mobility of the fluid and elements concerned.
3. Compare the results to previous studies, including those from further afield at the Kalahari Manganese deposit.

Chapter 2.

Sample selection, analysis and lithostratigraphy

2.1 Sample selection

After the initial diamond drilling of the boreholes, a combination of logging and assay results brought about the discovery of an enriched assemblage beneath the conglomeratic iron-ore in a number of boreholes. For the purpose of consistency, the 3 boreholes selected in this study are stratigraphically similar, and all contain anomalous amounts of Na, Ba and Mn. The three boreholes used in this study are: SLG002B, SLG537 and SLG017A. Samples were selected on the basis of their relative enrichment in one or more of following target elements outlined above. Samples were selected at regular intervals in the ore-zone, but more randomly in the alkali-enriched zone, in accordance with areas displaying anomalies in the target elements. 19 samples were taken from borehole SLG002B, 15 from SLG537 and 15 from SLG017A. The corresponding depths of the samples are displayed in Table 2 below. The sample depths in red are indicative of samples taken from the ore-zone, and do not contain any anomalous concentrations of Mn/Ba/Na, with the exception of drill core SLG002B, where Mn concentrations vary from 1.016- 2.195 wt.%. The sample locations are displayed beside the corresponding logs found in sub-chapter 2.3.

Table 2: The three boreholes sampled, and the corresponding depths of samples analyzed in each.

	Borehole SLG002B	Borehole SLG017A	Borehole SLG537
Sample no	**Depth (m)**	**Depth (m)**	**Depth (m)**
1	113.71-113.94	119.10-119.27	100.65-100.75
2	118.77-118.97	122.28-122.41	106.02-106.16
3	123.94-124.12	123.30-123.44	110.85-110.96
4	129.41-129.55	126.26-126.39	115.53-115.64
5	133.38-133.53	128.66-128.81	120.28-120.39
6	138.61-138.75	131.34-131.50	126.00-126.15
7	143.26-143.41	135.68-135.84	129.47-129.64
8	147.42-147.58	136.87-137.01	132.13-132.27
9	148.91-149.03	138.45-138.58	133.6-133.72
10	151.86-151.92	142.54-142.63	134.72-134.83
11	153.45-153.57	144.28-144.40	136.53-136.65
12	155.5-155.7	145.58-145.70	137.51-137.64
13	157.65-157.8	144.72-144.85	138.36-138.49
14	158.8-158.91	151.43-151.53	139.74-139.86
15	161.55-161.70	151.83-151.99	144.18-144.28
16	163.50-163.63		
17	166.7-166.82		
18	171.35-171.54		
19	178.75-178.85		

2.2 Sample analysis

A number of analytical techniques were used in this study, in order to extract the most information possible. Petrographic analysis of thin sections under the microscope was carried out using a combination of reflected and transmitted light, to determine mineralogical and textural features of the various units. Scanning electron microscopy (SEM) was conducted at the Rhodes University Zoology Department on many of the samples to supplement the petrographic analysis. The in-house electron probe micro-analyzer (EPMA) was used for mineral identification in some

cases, and to support the petrography with sound analyses of the diverse mineralogy. Analysis of major and trace elements was determined using X-ray fluorescence (XRF) spectrometry.

2.3 Lithostratigraphy and macroscopic observations

2.3.1 Introduction

Through logging of the borehole material, four common and reoccurring lithological units have been identified to represent the entire package of rocks sampled. For the purpose of this study, Fe-clasts which have a massive appearance will be referred to as hematite, while those which contain laminations will be referred to as Banded Iron Formation (BIF) clasts. It's important to bear in mind though, that at least in some cases, the 'hematite' clasts may have been sourced from the Fe-rich portion of a larger BIF clast. The four units are defined below as:

1) Clast-supported conglomerate (conglomerate is used interchangeably with CGT from here on): A unit dominated by Fe-clasts, which contains a matrix consisting of a combination of fine-grained siliceous and Fe-rich material. Due to the level of ferruginization, this unit is also recognized as, and referred to interchangeably as the 'ore-zone'.
2) Matrix-supported CGT: This unit is characterized by more sporadic Fe-clasts, set in a matrix dominated by fine-grained Fe-rich and siliceous material.
3) Ferro-manganese unit (FEM): This unit is dark brown to black, and as the name suggests, it is dominated by manganese material, but also contains a significant Fe-component.
4) Shale: The shale is typically a deep red/brown colour, but also contains a paler beige/white component, and when these two are combined they form what is commonly referred to as 'mottled' shale.

This chapter presents schematic logs for the three drill cores sampled, namely SLG002B, SLG537 and SLG017A, including the depth of each respective sample. Macroscopic examples from each unit outlined above have been included in the descriptions below.

2.3.2 Borehole SLG002B

Seventy meters of core was logged (from 110- 180m), displaying the changes in lithology and most importantly the Mn/Ba/Na-rich units below the ore zone. At the base of the sampled stratigraphy, faulted, deformed and mottled shale exists until ~ 178m. The shale is predominantly mottled in colour, and is highly weathered and brittle in places. A sharp contact exists between the shale and the overlying, matrix-supported conglomerate. This conglomerate is comprised of sub-rounded BIF clasts, medium rounded hematite and chert clasts in a chert-rich matrix, which gives it an overall grey colour. Clast size is variable, from millimeter scale right up to 10cm, with an average of approximately 1cm. The contact between the conglomerate and the overlying ferro-manganese unit (FEM) unit is sharp, and occurs at ~172m. This unit is massive, fine-grained and dominantly black, with the exception of a ~6cm wide bed of red/brown shale (SLG002B/18). The fine-grained ferro-manganese unit forms a sharp contact with the above lying conglomerate at ~170m. This conglomerate is very similar to the previous, below lying conglomerate in terms of its cherty matrix-supported nature, as well as the abundance, size and rounding of the BIF, hematite and chert clasts.

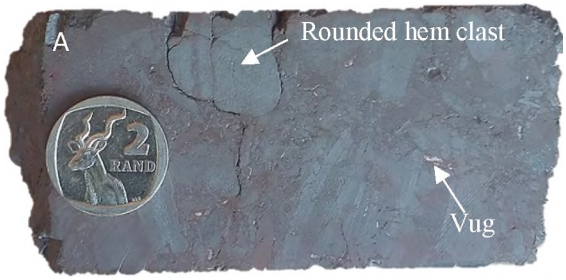

Clast-supported CGT

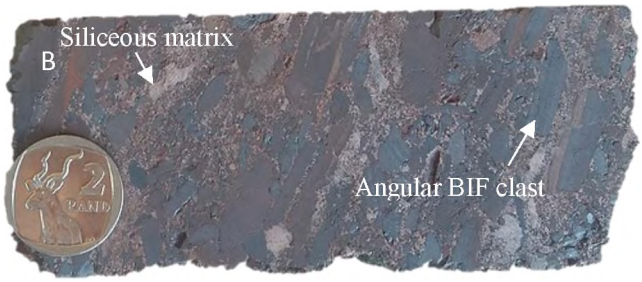

Matrix-supported CGT

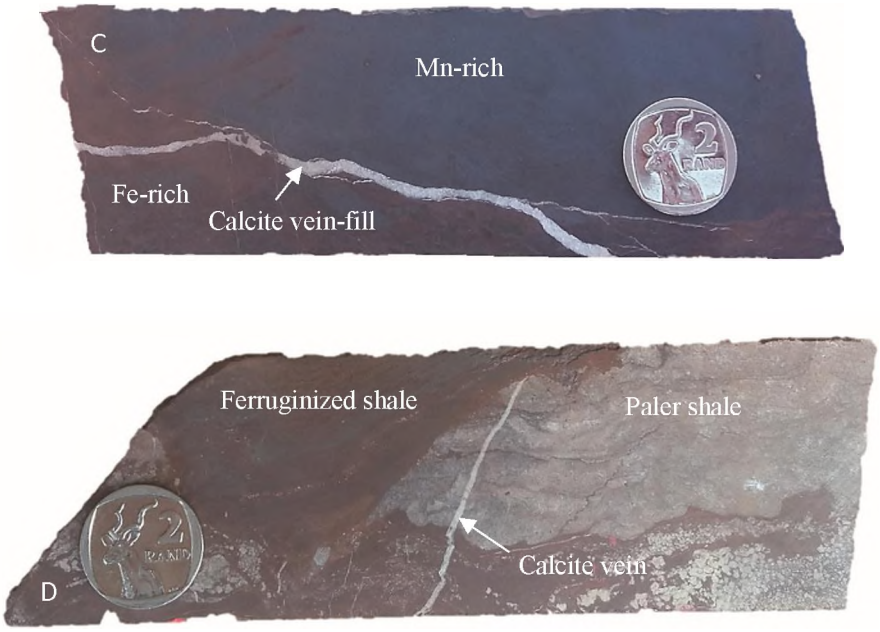

Figure 6: **A**. Typical example of poorly sorted clast-supported CGT, with large Fe-clasts and sporadic vugs. **B**. Matrix-supported CGT containing more interstitial silicates than the clast-supported CGT. **C**. Ferro-manganese unit displaying common veining. **D**. The shale unit displays the 3 common compositions, namely: the red/brown ferruginized end-member (top-left), the paler shale (top-right), and the mottled shale – a combination of both, at the bottom right.

The presence of 1.5cm thick manganese veins in places, is also noteworthy. The contact with the above lying FEM unit is gradational, spanning over roughly 30cm from 164.5-164.2m, with this area containing a mixture of FEM and CGT (BIF & hematite clasts) characteristics. Massive FEM, with sporadic vugs and a minor amount of red shale occur after this, until the unit grades back into CGT for 20cm at ~163.5m. The CGT is matrix supported and contains angular BIF clasts (up to 6cm) along with rounded hematite and chert clasts (up to 5.5cm). At ~159.4m, the CGT unit grades into the overlying FEM unit, over a length of 10cm. This FEM unit is massive and also contains some red shale (more than the previous FEM unit). Once again, the contact with the overlying CGT at ~157.4m is gradational.

This conglomerate contains significantly larger clasts of chert (up to 10cm), some of which appear brecciated, as well as shale remnants. At ~154.2, a large unit of FEM commences upward for almost 10m. This unit is massive, fine grained and also contains remnants of shale, along with vugs of approximately 2mm in diameter. There are also cross-cutting calcite veins of up to 4mm in width. A gradational contact into the above lying CGT occurs at ~144.4m. BIF and

hematite clasts are dominant and their abundance has increased, this conglomerate is now clast-supported. Hence, this CGT is more ferruginized than previous, matrix-supported versions. This conglomerate continues vertically, displaying minor changes in ferruginization for the rest of the sampled stratigraphy. Sporadic vugs (up to 8mm) containing felsic minerals are common. The presence of fine laminations of red-brown shale is also noted at ~121m. The associated log, indicating sample localities and depth is found below, together with the legend.

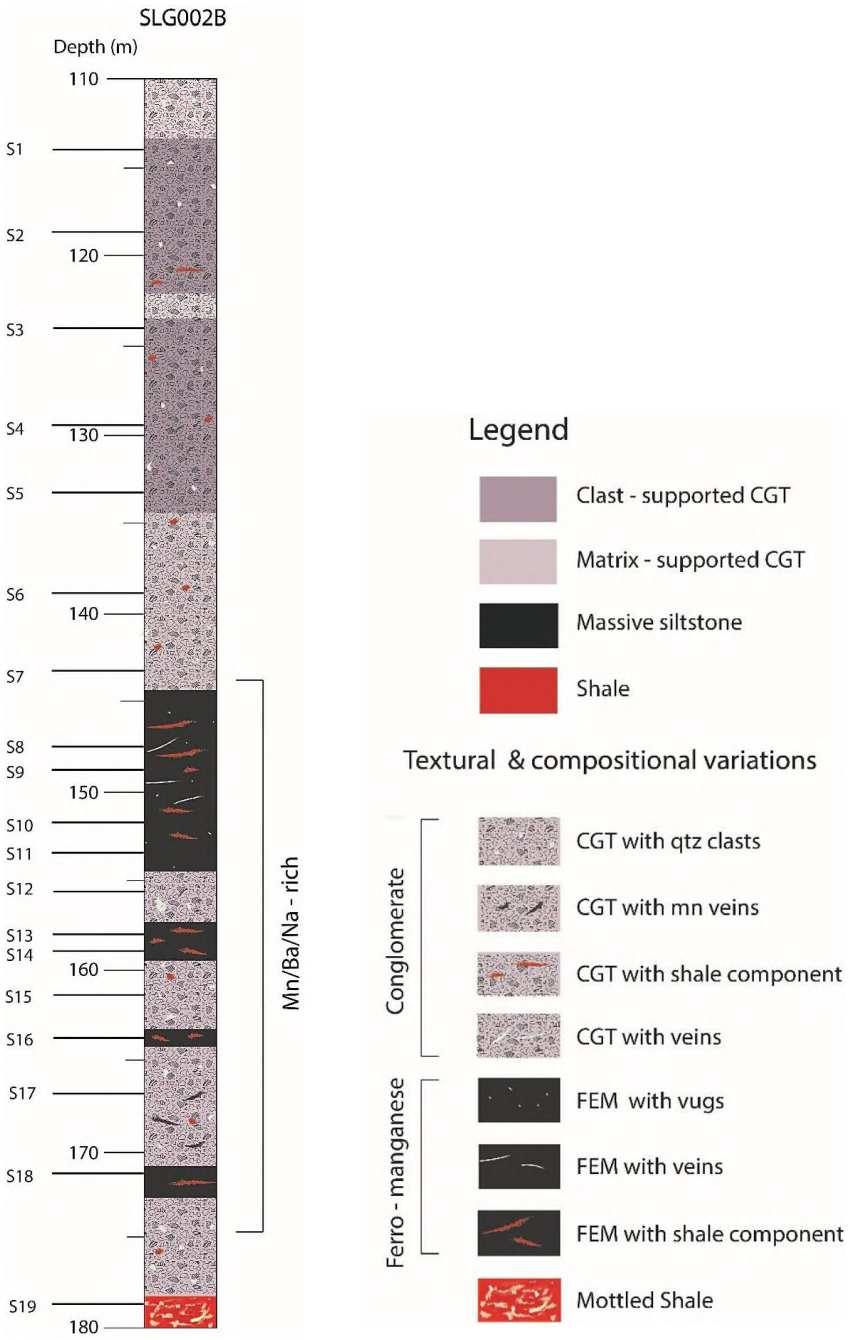

Figure 7: Lithostratigraphy of Borehole SLG002B and associated legend.

2.3.3 Borehole SLG537

Forty-five meters of core was logged for borehole SLG537, from 100- 145m (Figure 8). The bottom of the sampled stratigraphy consists of a massive, fine-grained unit of FEM. This unit is comprised of black manganese-rich material, which alternates with bands of red/brown shale. The FEM unit forms a gradational contact with the overlying matrix-supported CGT at 143.3m, which is comprised of sub-rounded hematite, sub-angular BIF and sub-rounded chert clasts in a quartzite matrix. These clasts are variable in size, reaching up to 3cm. the BIF clasts do appear to become slightly more rounded higher up in this unit. The CGT forms a gradational contact with the above lying FEM unit at 139.68m. This unit of FEM is massive and contains a shale component which gives it a red/brown colour in areas, as well as a mottled colour. Crosscutting veins of calcite are also present, and reach a width of 3mm. A gradational contact overlies the FEM, with a massive, black manganese unit at 138.3m.

A sharp contact at 137.41 marks the start of a narrow unit of matrix-supported conglomerate, which extends until 136m. This unit is dominated by hematite clasts of approximately 1cm, in a quartzite matrix. A sharp contact at 136m gives rise to a narrow unit of massive FEM, that contains a component of brown and cream shale, extending until 135.2m. This is followed by a sharp contact with a narrow (30cm) unit of matrix-supported conglomerate that is overlain by another sharp contact with a narrow FEM unit at 134.83m. This unit is dominated by BIF and hematite clasts, set in a very quartz-rich matrix. Clast size is variable up to 3cm. The hematite clasts are generally well-rounded, while the BIF clasts are sub-rounded. This unit extends for a number of meters until 130.3m, where a sharp contact marks the start of a narrow unit of massive Mn-rich material.

The Mn-rich unit extends until 129.25, after which it grades into a unit of FEM, which is black and massive. This unit grades into the overlying unit of matrix-supported CGT at 128.4m. This CGT is poorly sorted, with clast size being variable up to 8cm, in a matrix of immature quartzite. At 121.35m, the clast size of the CGT decreases slightly. Hematite and BIF clasts are angular to moderately rounded, poorly sorted and are set in a similarly immature quartzite matrix. At 110.4, a gradational contact marks the start of clast-supported CGT (ore-zone). This unit contains

angular clasts of BIF and hematite of up to 4cm, with very limited matrix material. The associated log, indicating sample localities and depth is found below, together with the legend.

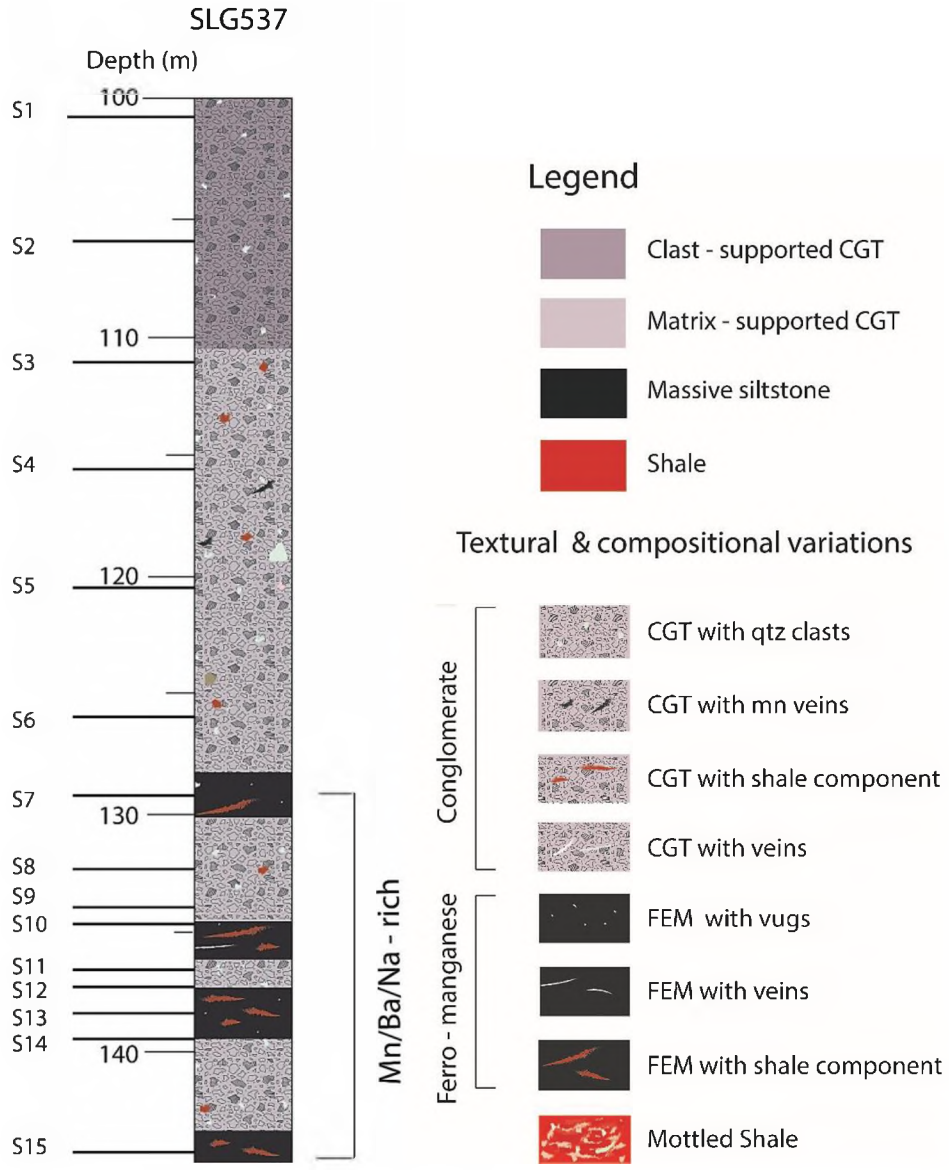

Figure 8: Lithostratigraphy of borehole SLG537 and associated Legend.

2.3.4 Borehole SLG017A

Thirty-three meters of core was logged for borehole SLG017A, from 152-119m (Figure 9). The lowermost unit sampled is the shale, starting at ~153.1m. This unit is fine-grained and shows variability between a lighter coloured 'mottled' shale, and a red/brown more ferruginous type. A gradational contact at ~151.3m sees the introduction of matrix-supported conglomerate in this core. The clasts consist of poorly sorted, well-rounded hematite and chert clasts, along with sub-angular BIF clasts in a quartzite matrix. The overlying FEM unit starts after a gradational contact at ~144.45m. This unit is fine-grained, massive and contains remnants of shale in areas, as well as crosscutting veins of calcite. A gradational contact at 141.5m sees the reintroduction of CGT, dominated by rounded hematite clasts – which are up to 3cm in size. Chert clasts are common and well-rounded, up to 2cm in size. Sub-rounded BIF clasts are common, reaching up to 4cm in length. The presence of crosscutting, felsic veins (0.5mm in width) is also noteworthy (SLG017A/9).

Once again, an FEM unit overlies the CGT, starting gradationally at ~137.2m. This FEM has a significant shale component, as is evident in the amount of red/brown sediment observed in sample SLG017A/8. Vugs (up to 2mm diameter) hosting silicate minerals are sporadically represented in this unit. The overlying unit is a matrix-supported CGT (which follows after a gradational contact at ~133.9m) which is typically comprised of BIF, hematite and chert clasts in a quartzite matrix. This unit is poorly sorted and contains large, well-rounded hematite clasts of up to 5cm. This unit is overlain by a massive, fine-grained FEM unit, which contains a shale component (SLG017A/4). Bedding is observed in this unit, with alternating layers of black, Mn-rich and red/brown shale bands. Vugs of <2mm in diameter are present, however uncommon. ~126.1m marks the start of clast supported CGT. This unit is dominated by sub-angular BIF and rounded hematite clasts with quartz grains in the matrix. Although uncommon, chert clasts are present in this unit. The associated log, indicating sample localities and corresponding depths is found below, together with the legend.

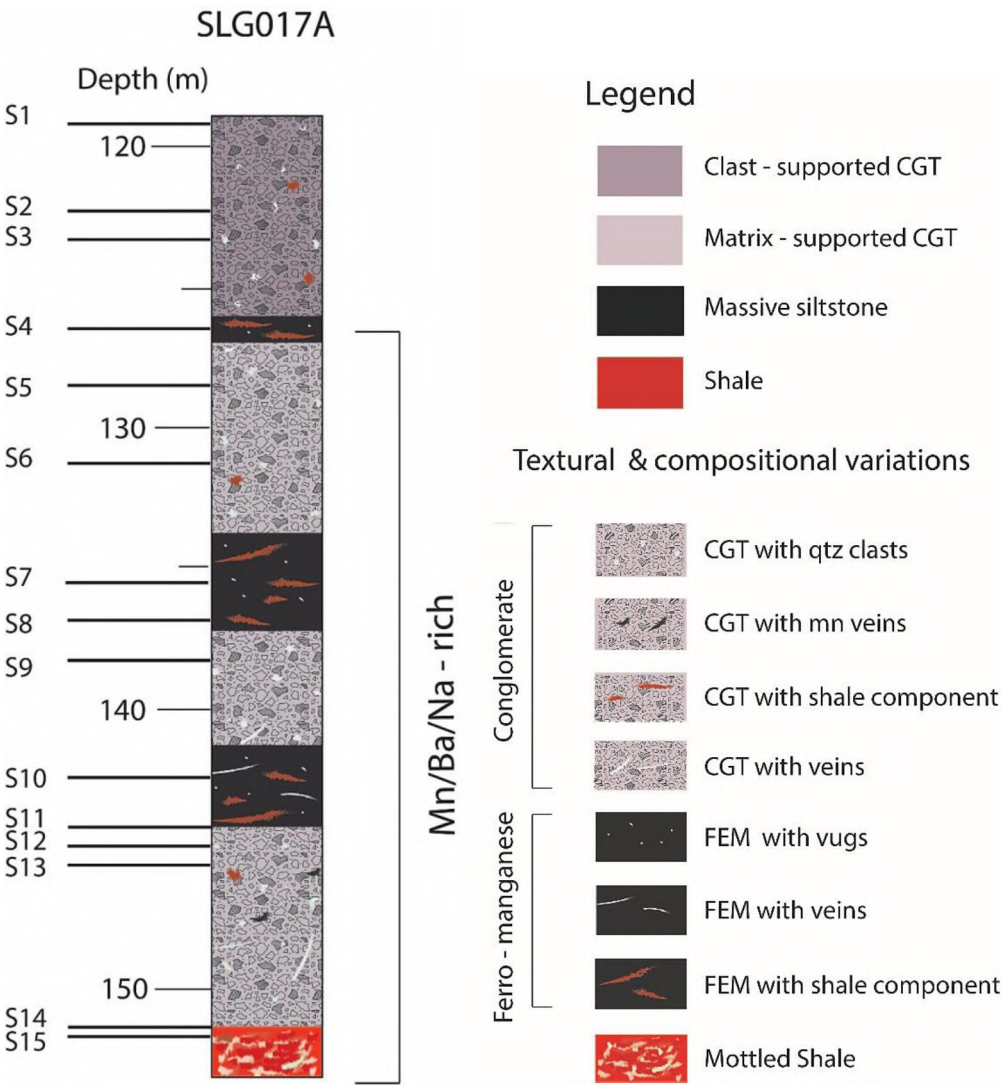

Figure 9: Lithostratigraphy of borehole SLG017A and associated legend.

Chapter 3.

Petrography & Mineral Chemistry

Petrographic and mineral chemistry work has been conducted on 59 polished thin-sections. These were selected on their potential to provide the most complete mineralogy, and hence provide the best understanding of the various lithological units, and perhaps shed light on the processes which have led to the observed anomalies. Samples containing particularly high concentrations of Mn/Ba/Na were favored for analysis. For minerals that were challenging to determine under the microscope, EDS analysis was carried out (on a SEM in Rhodes Zoological department) to give an indication of the elemental composition, followed by Electron Probe Microanalysis (EPMA) with the JEOL JXA-8230 Super probe at the Department of Geology, Rhodes University. Photomicrographs were captured under plain-polarized light (PPL), cross-polarized light (CPL) and reflected light (RL).

3.1 Clast-Supported Conglomerate

This unit is expectedly very iron-rich, with large hematite and BIF clasts dominating. Clast size is variable – up to 5cm. Hematite clasts display more rounding than the more angular BIF clasts – likely due being transported over a longer distance prior to deposition. As observed in Figure 10 below, the BIF clasts display very prominent banding, which is generally length parallel to the elongated clast. The original silica bands have largely been replaced by microplaty hematite – specularite. An interesting feature which is not limited to this unit, but is also featured in Figure 10 below, is the highly fractured nature of many of the clasts, which appear brittle.

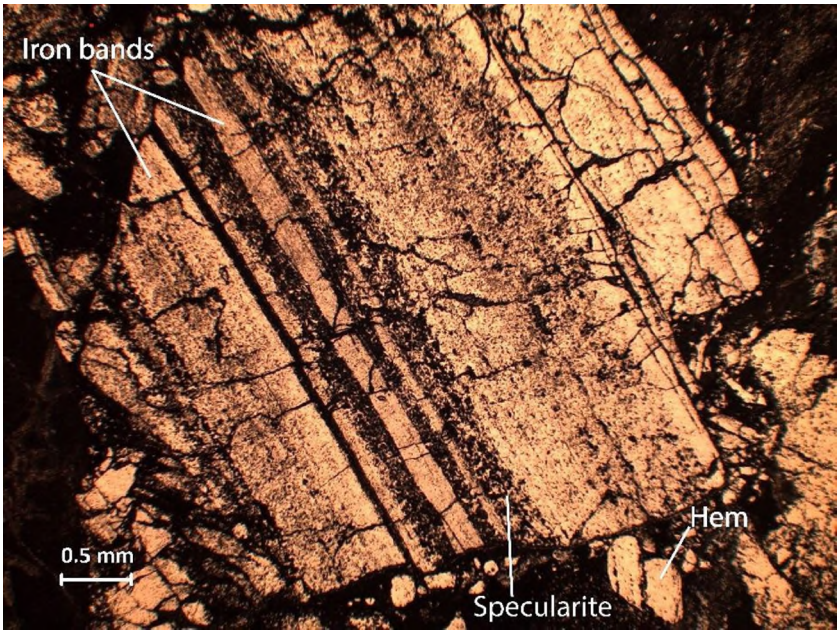

Figure 10: Typical angular BIF clast, with alternating bands of iron and secondary microplaty hematite (specularite) in CPL. The more rounded nature of the hematite clasts is depicted in the bottom right of the photomicrograph.

In some instances, grain boundaries of the iron clasts are lined by veins, which hug the edges of the competent, unfractured clasts. Where fractured, the veins crosscut these clasts, leading to the connection of various veins. Where possible, these veins have pooled and precipitated their solution interstitially. These textures suggest later fluid infiltration. The nature of these veins is observed in Figure 11 below.

An interesting feature of the veins is their consistent enrichment in manganese on the edges of the veins, while the centres of the veins are enriched in calcium. A magnesium-rich component is also present in many of the veins, and forms the very dark outermost part of the vein, as seen in Figure 11 below. This Mg-rich lining is not as consistent as the Mn and Ca zoning, and is sometimes absent on the edge of the vein. These veins are only present in borehole SLG002B, where they contribute largely to overall bulk-rock manganese concentration of 1-3 wt. % in this unit. Manganese is also found in the BIF and hematite clasts, with up to 3 % Mn_2O_3 – an example of this is presented in the Mn map in Figure 12 below. This is supported by similar findings by Fairey (2013), who also reported ~4 wt. % Mn_2O_3 in the hematite of rocks sourced from the PMF.

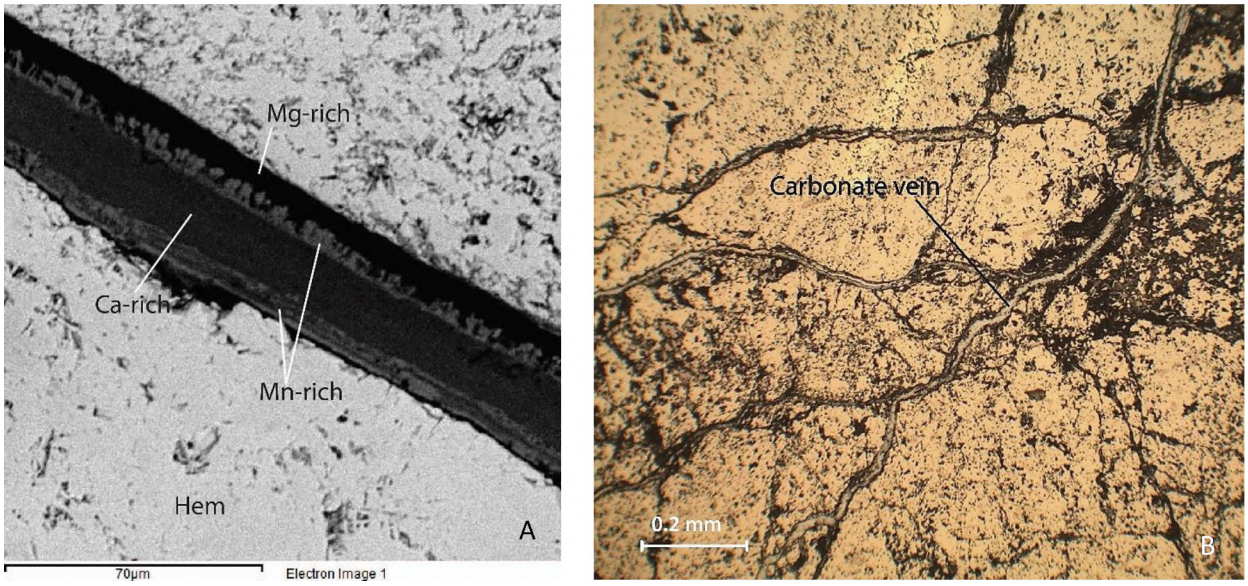

Figure 11: **A**. Backscatter image of a Mn, Ca, Mg-rich vein, displaying the zonation of these elements in space within the vein. **B**. Carbonate vein under reflected light. Sample SLG002B/5.

Table 3 below displays the variability in concentration of Mn and Ca in the carbonate veins, with the Mg and Mn crystallizing first near the edges of the veins, followed by the crystallization of the calcium-rich residual centre. Note the similarity between the composition of kutnohorite and the vein centre.

Table 3: Carbonate vein rim and vein centre, containing varying concentrations of Mn and Ca within the vein. Note that the vein centre has a composition which is almost identical to kutnohorite

Vein rim		
Oxide wt. %	n = 3	Std. Dev.
SiO_2	0.32	0.24
Fe_2O_3	1.34	0.17
MnO	46.86	1.87
MgO	2.52	0.46
CaO	5.59	2.49
CO_2*	43.35	0.49
Total	99.97	0.07
Cations calculated on the basis of 1 CO_3		
Si	0.01	
Fe	0.02	
Mn	0.77	
Mg	0.07	
Ca	0.12	
Total	0.98	
* Calculated based on kutnohorite formula		

Vein centre		
Oxide wt. %	n = 3	Std. Dev.
SiO_2	0.02	0.01
Fe_2O_3	1.30	0.11
MnO	17.53	1.04
MgO	0.66	0.06
CaO	40.17	0.46
CO_2*	40.64	0.38
Total	100.30	0.36
Cations calculated on the basis of 1 CO_3		
Si	0.00	
Fe	0.02	
Mn	0.25	
Mg	0.02	
Ca	0.71	
Total	0.99	
* Calculated based on kutnohorite formula		

Kutnohorite		
Oxide wt. %	n = 3	Std. Dev.
SiO_2	0.21	0.33
Al_2O_3	0.04	0.03
Fe_2O_3	1.16	0.46
MnO	16.16	0.31
MgO	0.76	0.04
CaO	40.34	1.84
BaO	0.02	0.01
CO_2	41.14	0.75
Total	99.83	1.05
Cations calculated on the basis of 2 CO_3		
Si	0.00	
Al	0.00	
Fe	0.01	
Mn	0.23	
Mg	0.02	
Ca	0.72	
Ba	0.00	
Total	0.99	
* Calculated on the basis of kutnohorite formula		

In certain areas, the veins have pooled, precipitating out a larger volume of their solution between the iron clasts. This mineral is confirmed as kutnohorite and is observed in Figure 12 below, where carbonate solution has precipitated interstitially, near the top corner of the main BIF clast. The Mn-rich area within the BIF clast is highlighted in dark blue. Although small, the relative scale of the concentrations of Mn and Ca are present on the right of each respective map. The lowest concentrations are simply black, with an increase indicated by dark blue through to green, followed by yellow, with the highest concentrations depicted in red and pink.

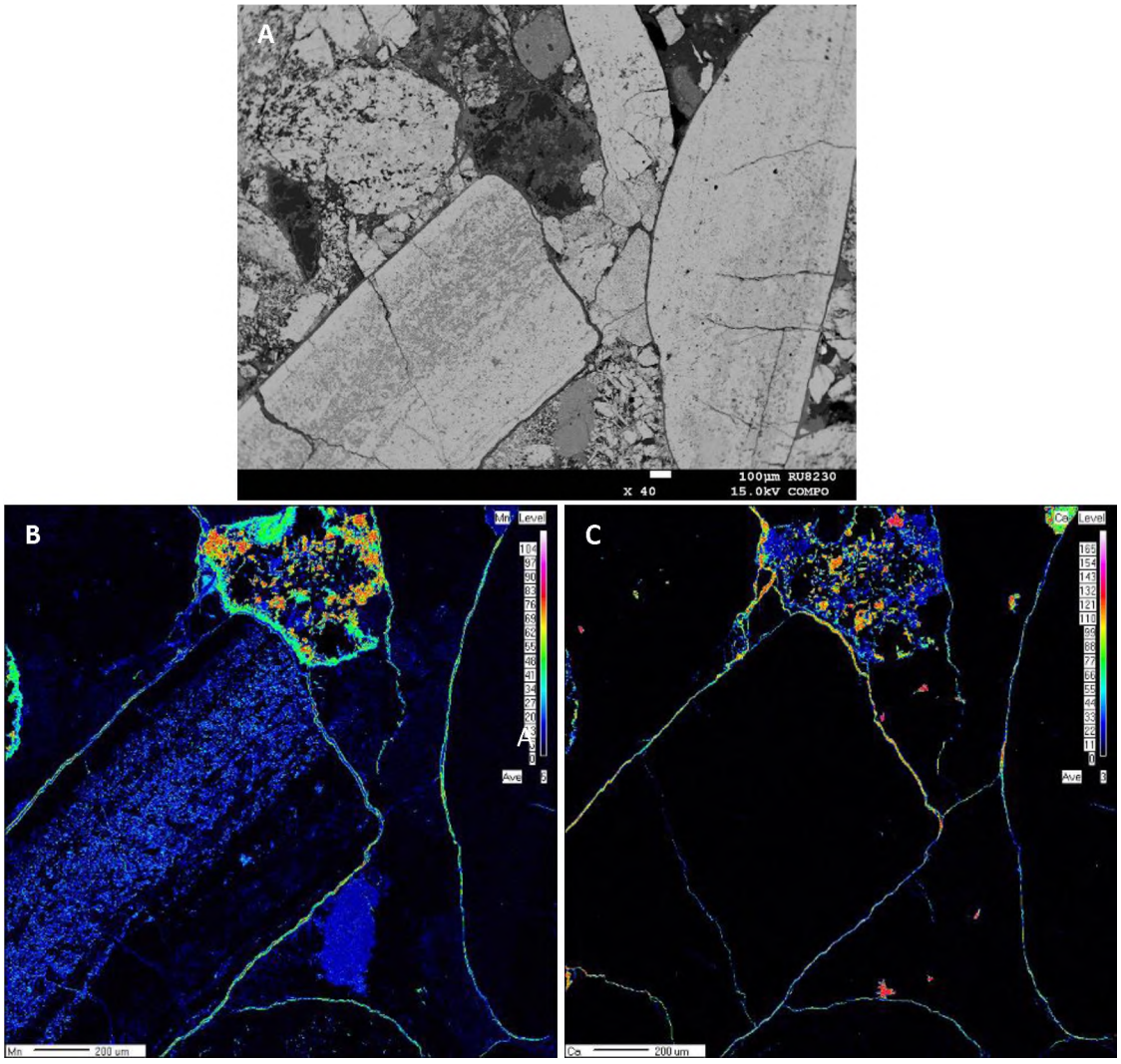

Figure 12: Clast-supported CGT with carbonate veining. Sample SLG002B/5. **A**. BIF and hematite clasts with carbonate veins on the edges, and as fracture-fill. **B**. Manganese map. **C**. Calcium map. Scale in **B** & **C** represents counts/second.

The presence of compositionally variable vugs in this unit is notable. Barite is the most common vug-filling mineral in this unit, and is a pale yellow colour in PPL. Sample SLG017A/2 (Figure 13) below features both aegirine and barite in the same vug, with aegirine concentrated around the walls, while barite is located in the centre of the vug. The aegirine shows textural variation, becoming more lath-like (acmite) moving towards the centre of the vug (Figure 13 (Top)).

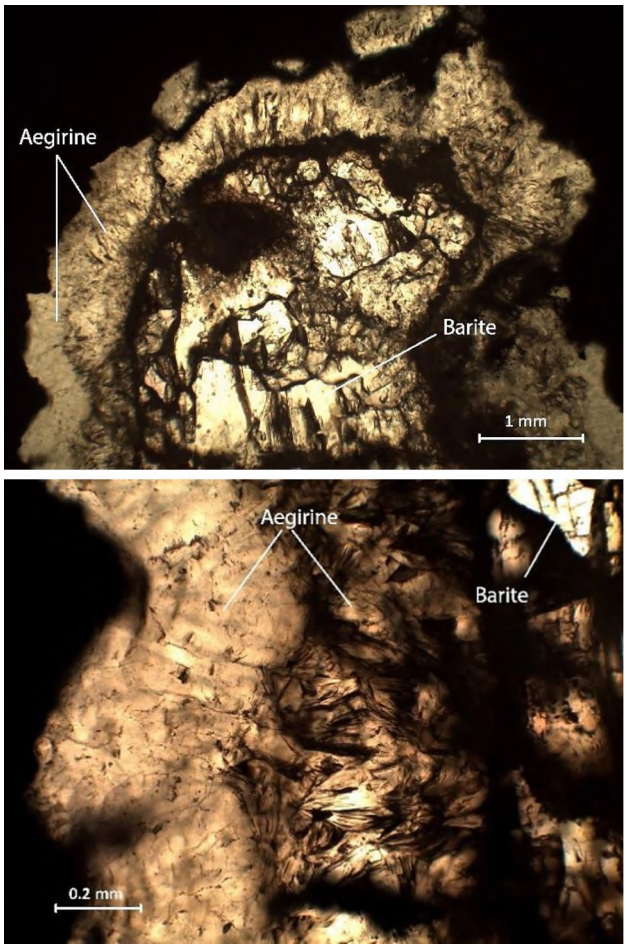

Figure 13: Vug containing K-feldspar and barite. **Top**. Textural variation of aegirine seen in the wall of the vug. **Bottom.** Vug containing aegirine around the rim, and barite in the centre. Both photomicrographs are in plane-polarised light, and the dark background is the Fe-rich matrix. Sample SLG017A/2

Table 4: Average aegirine composition of 4 microprobe analyses from borehole SLG002B.

Oxide wt. %	n = 4	Std. Dev.
SiO_2	52.11	0.43
Al_2O_3	1.49	0.37
Fe_2O_3	32.37	0.09
MnO	0.83	0.27
MgO	0.29	0.10
CaO	0.54	0.31
Na_2O	12.28	0.14
K_2O	0.03	0.01
Total	99.93	0.18
Cations calculated on the basis of 6 O		
Si	1.99	
Al	0.07	
Fe	0.93	
Mn	0.03	
Mg	0.02	
Ca	0.02	
Na	0.91	
K	0.00	
Total	3.97	

Although this zone is essentially iron-ore, the presence of prolific veins of carbonitic composition, along with vugs containing alkali and sulphur-rich minerals is suggestive of a metasomatic influence on these rocks. However, this will be further addressed in chapter 5. A summary of the minerals present in this unit is provided in Table 5 below.

Table 5: Mineral composition associated with the clast-supported CGT

Mineral	Composition
Aegirine	$NaFeSi_2O_6$
Barite	$BaSO_4$
Fluorapatite	$Ca_5(PO_4)$
Hematite	Fe_2O_3
K-feldspar	$KAlSi_3O_8$
Kutnohorite	$CaMn^{2+}(CO_3)_2$
Quartz	SiO_2

3.2 Matrix-Supported Conglomerate

The matrix-supported conglomerate is expectedly less iron-rich, and contains an abundance of silicate, sulphate and carbonate phases. There are typically fewer clasts of hematite and BIF, and although they are similar in terms of clast shape, clast size is generally smaller than that of the clast-supported conglomerate. This unit is can also be vuggy in areas, with a significantly higher density of vugs when compared to the clast-supported CGT. The vugs are compositionally variable.

Aegirine is a very common phase in this unit, and this mineral is widely documented in both the KMF and the PMF. Some examples of the widespread distribution of this mineral include a study by Dixon (1989), who documented aegirine in the manganiferous ore bodies of the Wessels mine (KMF), a study by Tsikos & Moore (2005) in the BIF's near to the Hotazel Formation (KMF) as well as by Fairey (2013), in the karst-hosted manganese deposits of the PMF. In this unit, the habit of aegirine is typically elongated and lath-like, and individual crystals are randomly orientated, often in very high density – forming fine-grained, needle like aggregates. Crystal size is highly variable and typically, one perfect cleavage is displayed. Aegirine is often observed in close association with albite, and common vug-fill in this unit consists of fine-grained aegirine laths on the rims, with albite in the centre – as seen in Figure 14 (A) below.

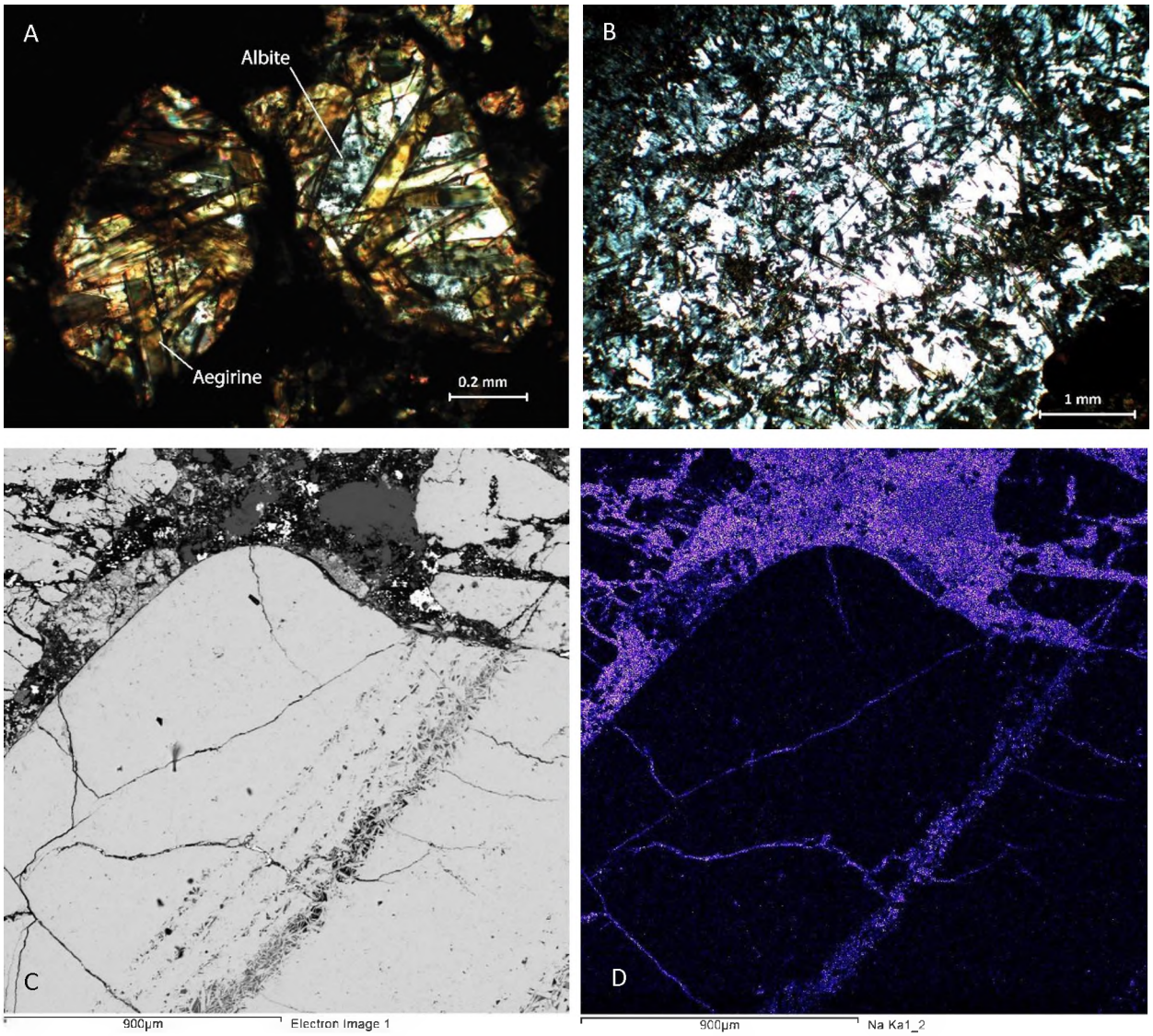

Figure 14: **A**. Aegirine laths dominating the vug-fill, with minor interstitial albite. **B**. Fine-grained, needle like aggregates of aegirine in a groundmass of larger albite crystals. **C**. Laminated BIF clast. **D**. Sodium distribution within BIF clast, and interstitially. Both **A** and **B** are in CPL. Sample SLG002B/12.1. **C** is a backscatter image and **D** is an elemental map (Na) from the EDS. **C** and **D** are from SLG537/13.2.

The distribution of aegirine is not only limited to vugs and interstitial space, but it has also been identified within laminated BIF clasts, with aegirine replacing silica. The extent of the sodium distribution is also highlighted by Figure 14 (B) above. Evidently, sodium is also present in the fractures.

A number of other minerals are also present in vugs of this unit, including; natrolite, calcite, witherite, barytocalcite, hyalophane and fluorapatite (see Figure 15 below). Natrolite is fine-

grained and occurs interstitially in vugs, although it can occasionally be the dominant vug-filling phase. This mineral is sodium-rich, and together with albite, aegirine and serandite, they make-up the Na composition of this unit.

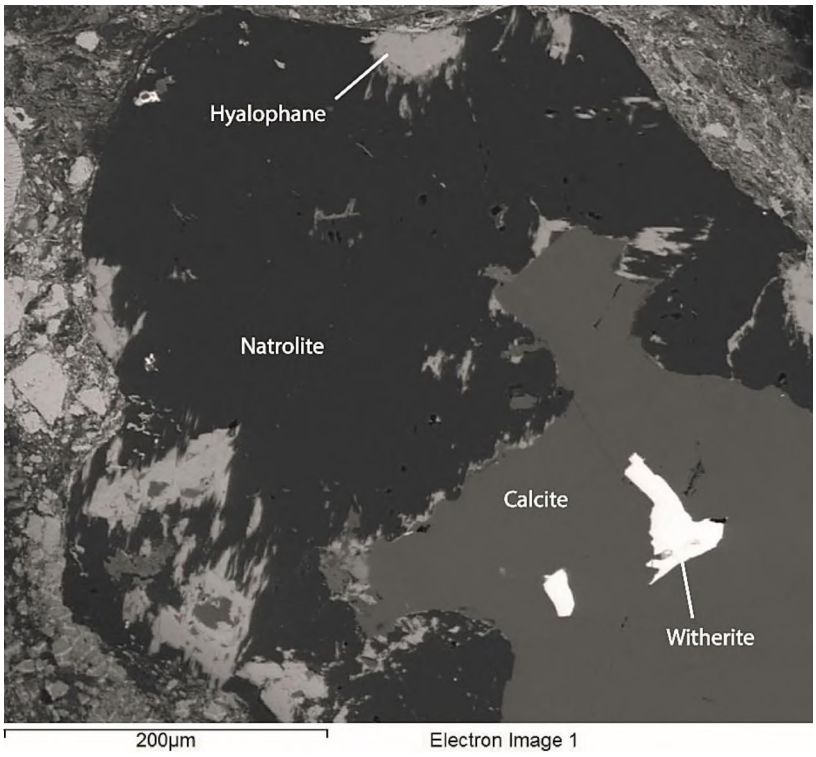

Figure 15: Calcite in close association with witherite. The vug also contains natrolite and hyalophane. Backscatter image from sample SLG537/9.1.

Table 6: Average natrolite composition from 6 microprobe analyses in borehole SLG537.

Oxide wt. %	n = 6	Std. Dev.
SiO_2	51.53	0.13
Al_2O_3	25.46	0.07
FeO	0.21	0.10
CaO	0.01	0.01
BaO	0.02	0.02
K_2O	0.06	0.01
Na_2O	13.01	0.35
F	0.02	0.05
Total	90.33	0.15

Cations calculated on the basis of 10 O	
Si	3.20
Al	1.86
Fe	0.01
Ca	0.00
Ba	0.00
K	0.00
Na	1.57
F	0.01
Total	6.66

Water not determined

Calcite is present in the form of fine-grained crystals and is often associated with barytocalcite and/or witherite – as is evident in Figure 15 above. The barytocalcite has a red/brown colour in PPL and a rough texture typical of carbonates. Witherite is the least abundant of the carbonates in this unit, and typically occurs as inclusions – either in calcite or barytocalcite.

Witherite and barytocalcite are the dominant barium-rich carbonate minerals in this unit, and their average compositions are displayed in Table 7 below.

Table 7: Average composition of witherite from 4 microprobe analyses (left). Average barytocalcite composition from 5 microprobe analyses (right) – both are from borehole SLG537.

Witherite			Barytocalcite		
Oxide wt. %	n = 4	Std. Dev.	Oxide wt.%	n=5	Std. Dev.
BaO	70.59	0.98	MnO	0.03	0.04
FeO	0.04	0.04	BaO	48.34	0.93
CaO	0.38	0.05	CaO	18.10	0.35
SrO	1.32	0.93	SrO	1.02	0.18
CO_2*	27.19	0.09	CO_2*	31.79	0.58
Total	99.51	0.43	Total	99.29	1.41
Cations calculated on the basis of 1 CO_3			Cations calculated on the basis of 1 CO_3		
Ba	0.96		Mn	0.00	
Fe	0.00		Ba	0.49	
Ca	0.01		Ca	0.50	
Sr	0.03		Sr	0.02	
Total	1.00		Total	1.00	
* Calculated based on witherite formula			* Calculated based on barytocalcite formula		

Serandite – $Na(Mn^{2+},Ca)_2Si_3O_8(OH)$, is commonly associated with low-temperature hydrothermal veins, or it occurs as a replacement mineral (Deer *et al.*, 1992). Serandite veining is evident in this unit, and this mineral is observed to replace quartz in vugs, retaining the primary texture of quartz – as observed in Figure 16 below. These findings are consistent with a recent study by Fairey (2013), who also observed serandite replacing quartz in vugs, both pseudomorphously and as 'matted' serandite, with some relict quartz remaining in the vugs.

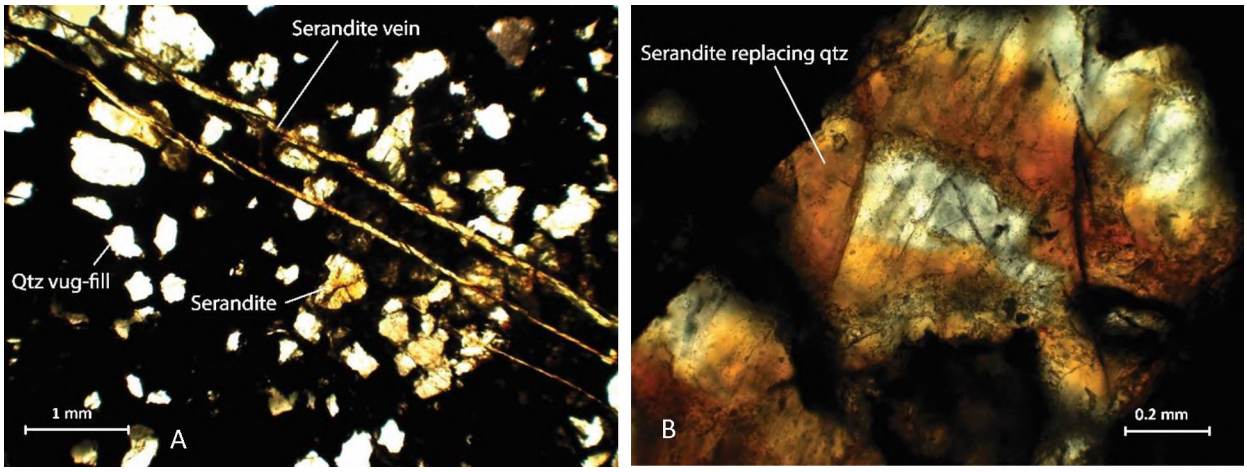

Figure 16: **A**. Typical vuggy matrix, containing quartz. Serandite veining has cross-cut this sample, and even replaced quartz in some of the vugs. **B**. Serandite replacing quartz and retaining the original habit of quartz. Both **A** and **B** are in plane polarized light. Sample SLG017A/12.1

Barite displays one cleavage and forms as vug-fill, either as a single crystal in a smaller vug, or as numerous subhedral crystals in larger vugs, often occurring together with calcite (SLG017A12.2). K-feldspar is limited, but where present, forms as fine grained, interstitial crystals. Flourapatite is an uncommon mineral in this unit, and only occurs as very fine-grained, rounded crystals in vugs. A summary of the minerals president in this unit is provided in Table 8 below.

Table 8 Mineral composition associated with the matrix-supported CGT

Mineral	**Composition**
Aegirine	$NaFe^{3+}Si_2O_6$
Albite	$NaAlSi_3O_8$
Barite	$BaSO_4$
Barytocalcite	$BaCa(CO_3)_2$
Calcite	$CaCO_3$
Fluorapatite	$Ca_5(PO_4)_3F$
Hematite	Fe_2O_3
K- feldspar	$KAlSi_3O_8$
Natrolite	$Na_2Al_2Si_3O_{10}\cdot H2O$
Quartz	SiO_2
Serandite	$Na(Mn^{2+},Ca)_2Si_3O_8(OH)$
Witherite	BaCO3

3.3 Ferro-Manganese unit

The ferro-manganese unit is dominated by a texturally massive matrix of braunite and hematite. Carbonates and silicates are located in crosscutting veins. Calcite, hyalophane and celsian are dominant in the veins; however, they are generally fine-grained due to the thin nature of these veins, making microscopic identification and the corresponding descriptions difficult. EDS and microprobe work on these samples was therefore critical in the determination of some of these minerals. Banalsite, with its composition of $BaNa_2Al_4Si_4O_{16}$, is an uncommon silicate in this unit, but along with hyalophane and celsian, it contributes towards the overall barium bulk-rock

concentration. This mineral is fine-grained, occurring in thin veinlets commonly alongside calcite. The average composition of banalsite from 3 analyses is displayed in Table 9.

Hyalophane is an intermediate member of the celsian-orthoclase series, and is typically associated with sedimentary manganese and ferro-manganese deposits (Mc Swiggen *et al.*, 1994; Deer *et al.*, 1975). Hyalophane has been well documented around the world, from the manganiferous iron ores of Otjosondu, Namibia (Viswanathan and Kielhoru, 1983), to the bedded manganese ores of Nodatamagawa, Kaso, Kaminagano and Shiromaru in Japan, to name but a few (Nakano, 1979; Matsubara, 1985; Kato et al., 1987). The presence of both hyalophane and celsian (K-free feldspar) in late, crosscutting veins is highly indicative of hydrothermal influence on these rocks.

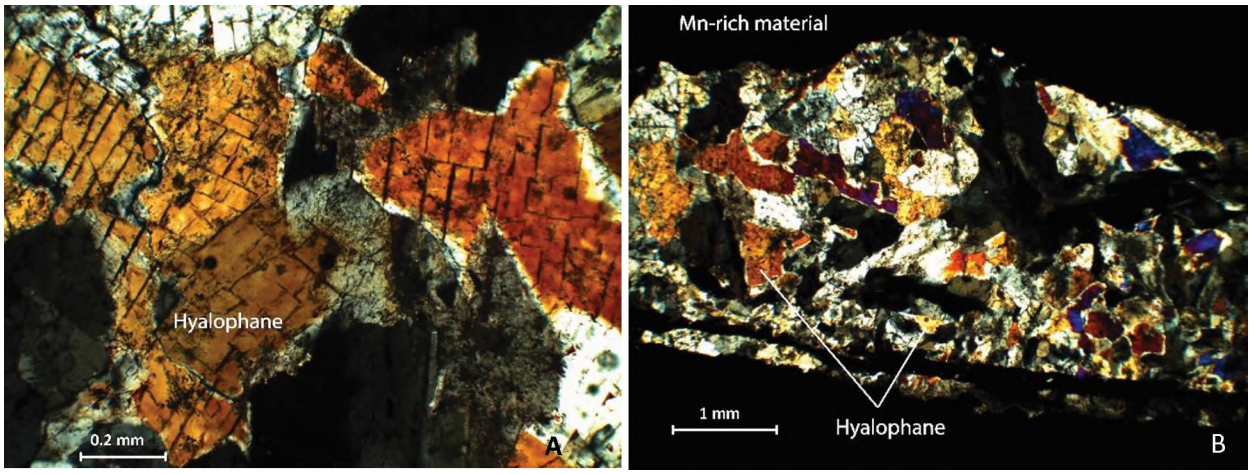

Figure 17: **A**. Hyalophane crystals displaying two cleavages, intersecting at 90°. **B**. Vein of hyalophane crystals crosscutting massive, manganese-rich material. Both **A** and **B** are in CPL. Sample SLG002B/8.

The average compositions of both hyalophane and banalsite are displayed in Table 9 below. Note that hyalophane and banalsite are compositionally quite similar, with the largest difference being that hyalophane contains potassium, and banalsite contains sodium.

Table 9: Average hyalophane and banalsite compositions from 3 analyses in borehole SLG002B.

Hyalophane			Banalsite		
Oxide wt. %	n = 3	Std. Dev.	Oxide wt %	n = 3	Std. Dev.
SiO_2	43.31	0.17	SiO_2	37.20	0.44
TiO_2	0.26	0.04	Al_2O_3	29.59	0.07
Al_2O_3	23.23	0.25	FeO	0.29	0.09
Fe_2O_3	0.22	0.09	MnO	0.17	0.05
Mn_2O_3	0.02	0.02	BaO	22.67	0.27
BaO	27.42	0.17	Na_2O	8.98	0.22
Na_2O	0.13	0.03	TiO_2	0.23	0.03
K_2O	5.77	0.11	K_2O	0.06	0.03
Total	100.36	0.42	Total	99.20	0.36
Cations calculated on the basis of 8 O			Cations calculated on the basis of 16 O		
Si	2.43		Si	4.10	
Ti	0.01		Al	3.85	
Al	1.53		Fe	0.03	
Fe	0.01		Mn	0.02	
Mn	0.00		Ba	0.98	
Ba	0.60		Na	1.92	
Na	0.01		Ti	0.02	
K	0.41		K	0.01	
Total	5.01		Total	10.92	

Braunite is the most common manganese-rich mineral in this unit, and makes the largest contribution to the bulk-rock Mn concentration. Braunite is texturally variable, but is generally present as very fine-grained, crystalline braunite – as seen in Figure 18 (A). The lead manganate, coronadite ($Pb\ (Mn^{4+},Mn^{2+})_8O_{16}$) is present in this unit – occurring rarely – as single, anhedral, fine-grained crystals. Coronadite was first discovered at the Coronado mine, in the Morenci district of Arizona in 1903, and has since been documented in manganese deposits across the world (Hewett, 1971). Coronadite forms a series with hollandite, which is the barium end-member of this Mn-oxide group. Unfortunately, due to the fine-grained nature of these minerals, coupled with poor polishing of thin sections, it was difficult to acquire more analyses on these minerals.

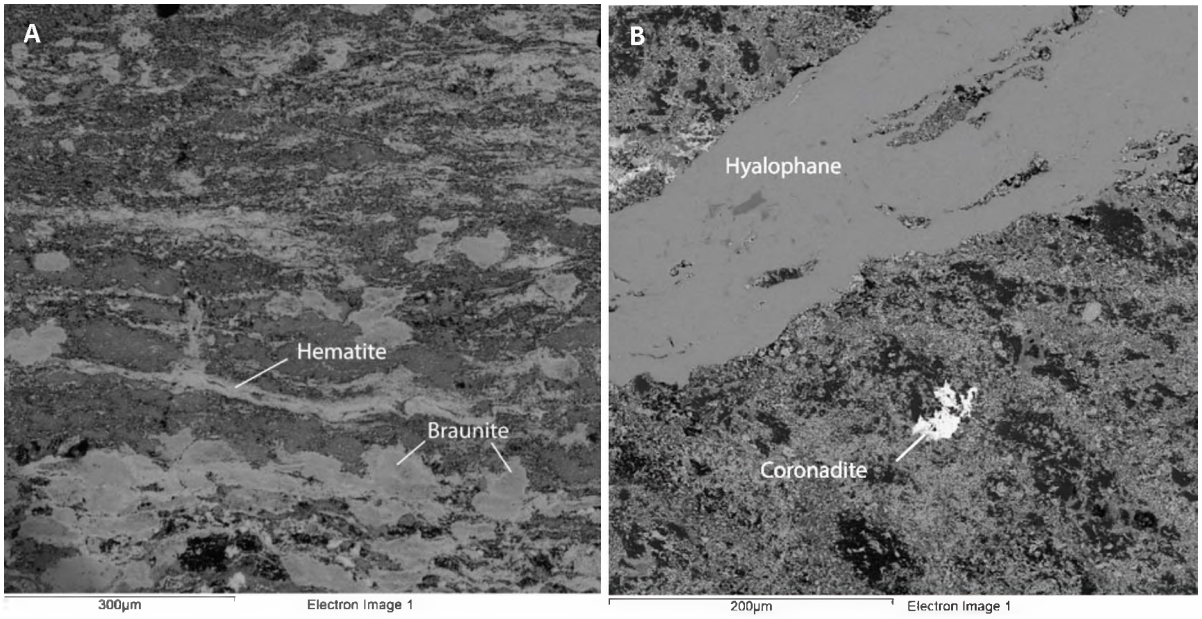

Figure 18: **A**. Fine-grained braunite and hematite in a lutite matrix. The matrix composition is variable, consisting of a mixed composition of Ba, Si, Fe, Al, Mn, Na, K. Sample SLG002B/13. **B**. Fine-grained, anhedral coronadite crystal, situated in a matrix of mixed celsian-hyalophane material. SLG002B/14.

Table 10 below quite clearly highlights the substitution between BaO and PbO, in the solid solution series between coronadite and hollandite.

Table 10: Chemical composition of coronadite and hollandite from borehole SLG002B.

	Coronadite		Hollandite
Oxide wt.%	n = 1	Oxide wt. %	n = 1
SiO_2	1.83	SiO_2	2.67
Al_2O_3	0.99	Al_2O_3	1.56
Fe_2O_3	5.56	Fe_2O_3	5.98
MnO_2	67.28	MnO_2	69.58
MgO	0.03	MgO	0.05
PbO	21.43	PbO	4.28
BaO	3.43	BaO	12.81
CaO	0.20	CaO	0.28
Total	100.76	Total	97.21
Cations calculated on the basis of 16 O for coronadite and hollandite			
Si	0.26	Si	0.36
Al	0.17	Al	0.25
Fe	0.60	Fe	0.61
Mn	6.64	Mn	6.54
Mg	0.01	Mg	0.01
Pb	0.82	Pb	0.16
Ba	0.19	Ba	0.68
Ca	0.03	Ca	0.04
Total	8.72	Total	8.66

* All Mn reported as Mn^{4+}

As mentioned in the lithostratigraphy section of chapter 2, the contacts between the ferro-manganese and the matrix-supported conglomerate are not always sharp, and where they are gradational, minerals typical of the matrix-supported conglomerate are present, such as barite, albite in veins, and minor serandite, which is often associated with aegirine.

Fine-grained barite is located within veins of this unit, displaying two cleavages. Albite, although not particularly abundant, is also a constituent of these veins. Although aegirine and serandite are not located in what would be defined as the strict ferro-manganese unit, their presence in the areas where there are gradational contacts between the ferro-manganese and the matrix-supported CGT units is worth a mention, at least for the purpose of indicating the distribution of their associated cations. A summary of the minerals present in this unit is provided in Table 11 below.

Table 11: Mineral composition associated with the ferro-manganese unit.

Mineral	**Composition**
Aegirine	$NaFe^{3+}\ Si_2O_6$
Banalsite	$BaNa_2Al_4Si_4O_{16}$
Barite	$BaSO_4$
Barytocalcite	$BaCa(CO_3)_2$
Braunite	$Mn^{2+}Mn^{3+}{}_6[O_8\|SiO_4]$
Calcite	$CaCO_3$
Celsian	$BaAlSi_3O_8$
Fluorapatite	$Ca_5(PO_4)_3F$
Hematite	Fe_2O_3
Hollandite-coronadite	$(Ba, Pb\ (Mn^{4+},Mn^{2+})_8O_{16})$
Hyalophane	$(K,Ba)Al(Si,Al)_3O_8$
Natrolite	$Na_2Al_2Si_3O_{10}\cdot H2O$
Serandite	$Na(Mn^{2+},Ca)_2Si_3O_8(OH)$

3.4 Shale unit

The shale unit is typically a fine-grained, massive, red-brown coloured unit. In places, the shale has a lighter component to it, and the term 'mottled shale' is used to describe areas where the more common red-brown shale has mixed with the paler component. This unit is comprised of a variety of minerals, of which hematite is the dominant mineral in the fine-grained, red-brown material. The hematite is finely laminated and often exhibits soft-sediment deformation – as observed in Figure 19 below. The paler component is dominated by calcite, which contains a significant Mn concentration of around 6 wt%. The calcite forms as rounded crystals, commonly containing fine-grained barite as inclusions in calcite. Inclusions of sodium-rich pockets are also common. The calcite crystals are separated interstitially by Na-rich pockets – with a composition close to that of aegirine (Figure 19 (A)).

The shale unit exhibits a number of vein-fill variations, with diverse compositions, including: pure-end member hollandite, crosscutting calcite and Na-rich veins. Where present, veins of hollandite crosscut the primary sedimentary structures, and are up to 4mm in width. The Na-rich veins have been mapped below, and these veins appear to exploit areas where the primary rock has fractured, confirmed by the offsetting observed in Figure 19 (B) below – where the Fe-rich material has been displaced by roughly 0.5mm.

The images presented in Figure 19 (B) and (C) below were taken very close to one another, and the same fe-rich, laminated material is observed in each. The material in Figure 19 (C) is however, noticeably more fractured than Figure 19 (B), and the Na map highlights the fractured nature of this rock, and the associated Na-rich fracture-fill.

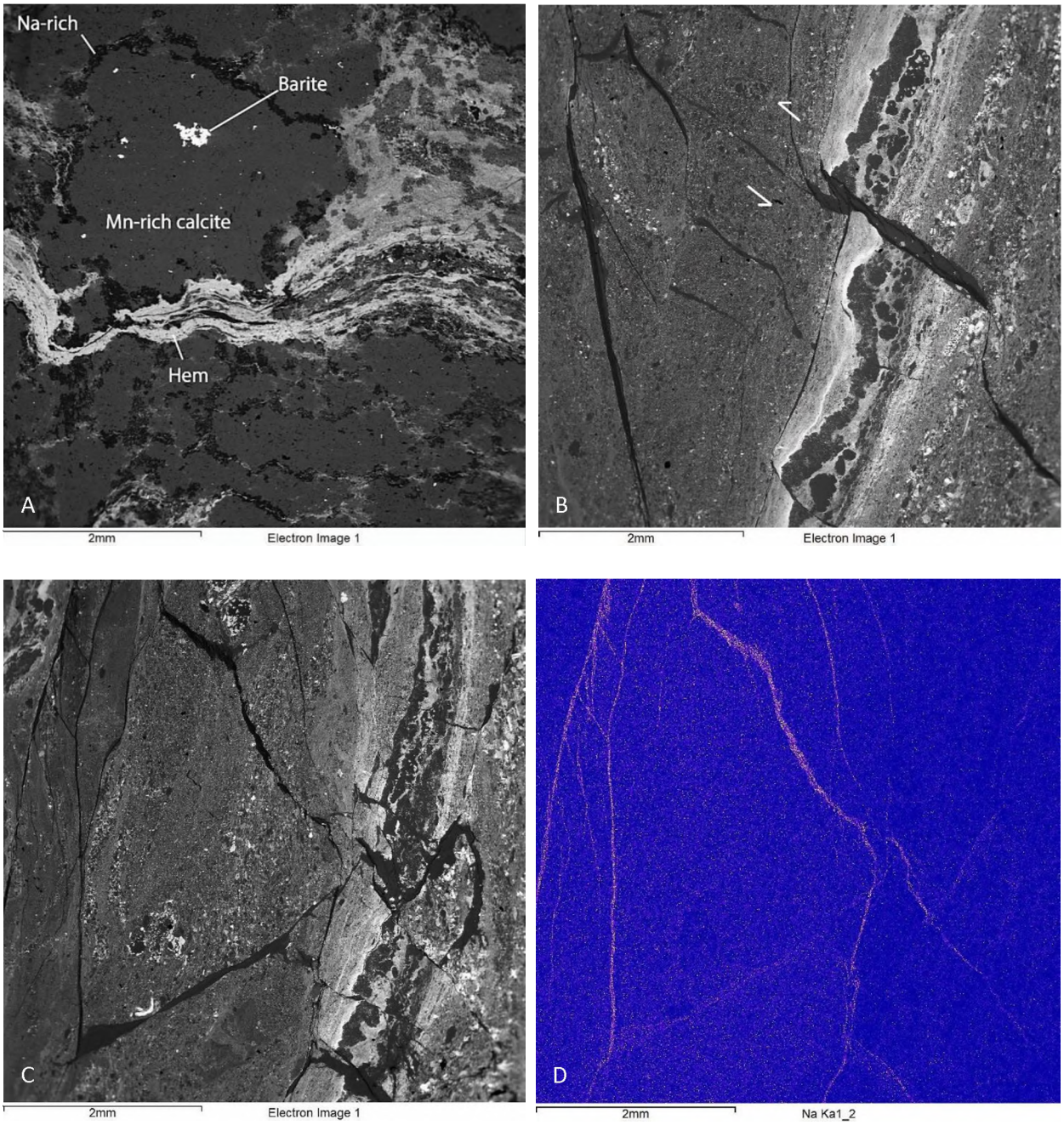

Figure 19: **A**. Interface between Mn-calcite and hematite in the shale unit. **B.** Displacement of Fe-rich material in the shale unit. **C**. Backscatter image asscoaited with Na-map in **D**. Sample SLG017A/8.

As in all of the previously decribed units, once again, barite is present. Barite can occur as an inclusion (Figure 19 (A)), as vug fill, or disseminated in the ferruginized groundmass. The size of the barite crystals is variable, and largely dependant on the location, as the grains are largest when present as vug-fill, and smallest when present in the groundmass.

Table 12: Average barite composition from 3 analyses in borehole SLG002B.

Oxide wt %	n = 3	Std. Dev.
SO_3	33.54	0.04
BaO	65.29	0.26
CaO	0.01	0.01
SrO	0.65	0.41
Total	99.48	0.17
Cations calculated on the basis of 4 O		
S	0.99	
Ba	1.01	
Ca	0.00	
Sr	0.01	
Total	2.02	

The minerals associated with this unit are displayed in Table 13 below. Although much has been made of the presence of sodium in this unit, due to the variable concentrations of sodium when analyzed in both the veins and vugs, it has not been classified as any particular mineral – but rather a component of mixed analysis.

Table 13: Mineral composition associated with the shale unit

Mineral	**Composition**
Barite	$BaSO_4$
Calcite	$CaCO_3$
Hematite	Fe_2O_3
Hollandite	$Ba\,(Mn^{4+},Mn^{3+})_8O_{16}$
K-feldspar	$KAlSi_3O_8$
Quartz	SiO_2

3.5 Key points to take from Chapter 3

- There are 17 distinct minerals which contain one or more of the elements Ba, Na and Mn.
- Significantly, alkali-containing minerals are present in the ore-zone too, albeit to a lesser extent than the enriched-zone.
- The alkali-containing minerals mostly occur in veins (serandite, celsian, hyalophane, banalsite, etc) and vugs (natrolite, aegirine, albite, witherite, barytocalcite, etc).
- Veins and interstitial pockets are highly suggestive of fluid mobility. This will be addressed further in chapter 5.
- Many minerals occur in more than one unit (K-feldspar and barite in all four).

Chapter 4.

Bulk-Rock Geochemistry

All three boreholes were sampled for bulk-rock geochemical analyses. Samples were taken from all four lithological units outlined in chapter 2. The clast-supported CGT (ore-zone) was sampled at regular intervals, of roughly 5 m. Naturally, the ore-zone thickness is not equal in all three boreholes, hence the sample size was slightly variable between boreholes.

With regard to the enriched-zone samples, Fe-clasts were avoided as much as possible, in favour of homogenous matrix material – the likely host of the target alkalis.

All samples were analysed for major elements, trace elements and Rare Earth Elements using XRF at the university of Stellenbosch. Refer to Appendix ii for analytical techniques.

Initially, the geochemical similarity between the three respective ore-zones was determined by comparing the average major and trace element compositions of the samples in each. These values were then normalized to a Kuruman-Griquatown BIF standard – derived from the work of Oonk (2017), as well as Post Archaen Australian Shale standard – from Taylor and Mclennan (1985).

The compositions of the ore-zones in each borehole were then compared to the samples sourced from the enriched-zone, on the basis of their major element, trace element and REE composition. This approach was applied to identify whether or not there is any geochemical link between the ore-zone and the enriched-zone in each borehole, that may provide suggestions as to the genesis of these assemblages.

4.1 Ore-Zone Major Elements

The ore-zone is expectedly Fe-rich, and this is evident in Figure 20 – where Fe_2O_3 is enriched relative to both PAAS and Kuruman-Griquatown BIF. Additionally, relative to the Kuruman-Griquatown standard, the ore-zone shows an enrichment in TiO_2, Al_2O_3 and K_2O in all of the boreholes. Only Fe_2O_3 and MnO_2 display an enrichment relative to PAAS.

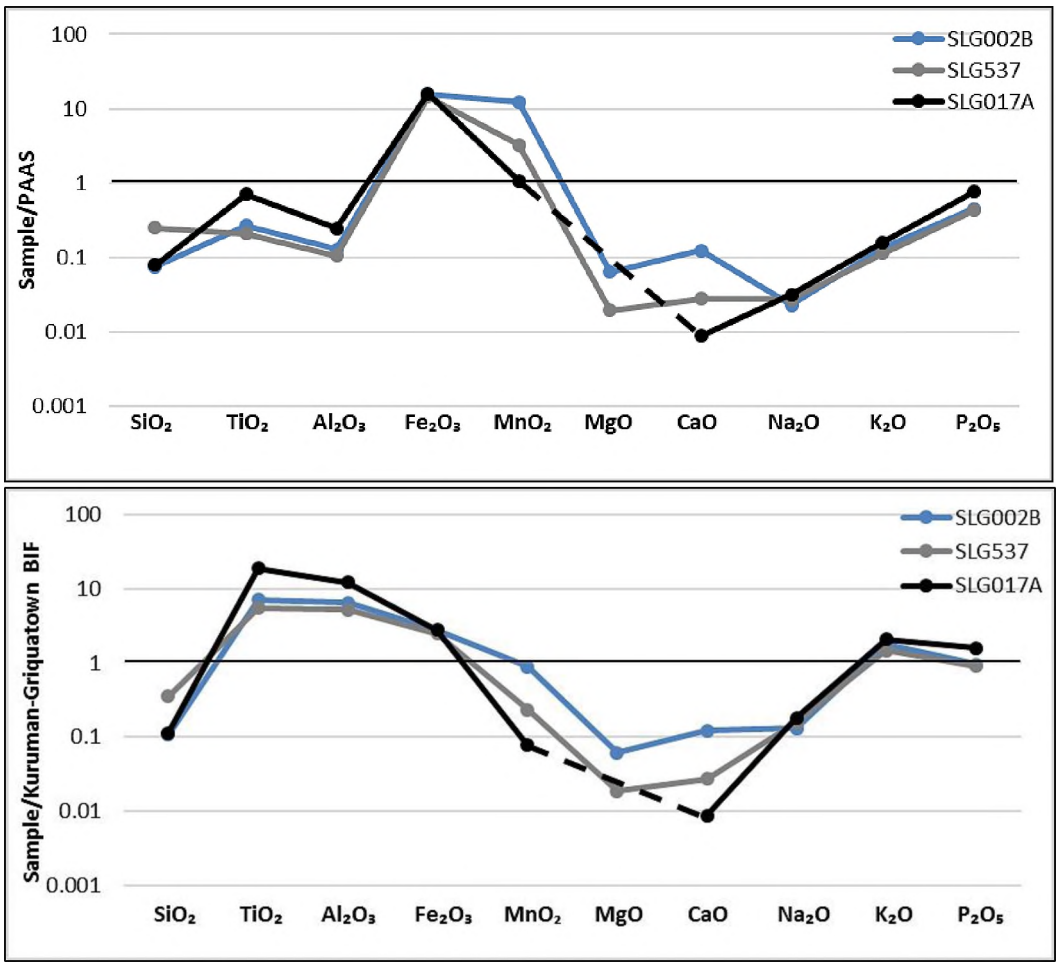

Figure 20: Ore-zone major elements normalized to PAAS (top) and Kuruman-Griquatown BIF (bottom).

Both diagrams above display relatively similar profiles for all major elements, across all boreholes, except for MnO_2, MgO and CaO – where borehole SLG002B has a roughly 5-fold enrichment in these oxides relative to borehole SLG537, and roughly a 10-fold enrichment in the aforementioned oxides relative to borehole SLG017A. This is largely due to the presence of Mn-carbonate kutnohorite in borehole SLG002B, as well as the carbonate veining which is comprised of Mn, Ca and Mg – as presented in chapter 3. The concentration of MgO was below the detection limit for borehole SLG017A, hence the dotted line connecting MnO_2 to CaO.

4.2 Ore-Zone Trace Elements

In a similar fashion to the major elements, the trace elements are also depleted relative to PAAS and more enriched relative to Kuruman-Griquatown BIF. Only Sr (in borehole SLG017A), Ba, and Pb show any enrichment relative to PAAS, or concentrations close to that of PAAS.

However, compared to Kuruman-Griquatown BIF, all trace elements are enriched relative to the standard, except for Rb, Cs (all boreholes) and Sr (boreholes SLG002B and SLG537). The Ba concentration for the respective boreholes in ppm is as follows: SLG002B = 517.980, SLG537 = 677.06, SLG017A = 77.88. It is clear that the ore-zones of all boreholes are significantly enriched in Ba relative to a Kuruman-Griquatown standard of 12.217 ppm Ba.

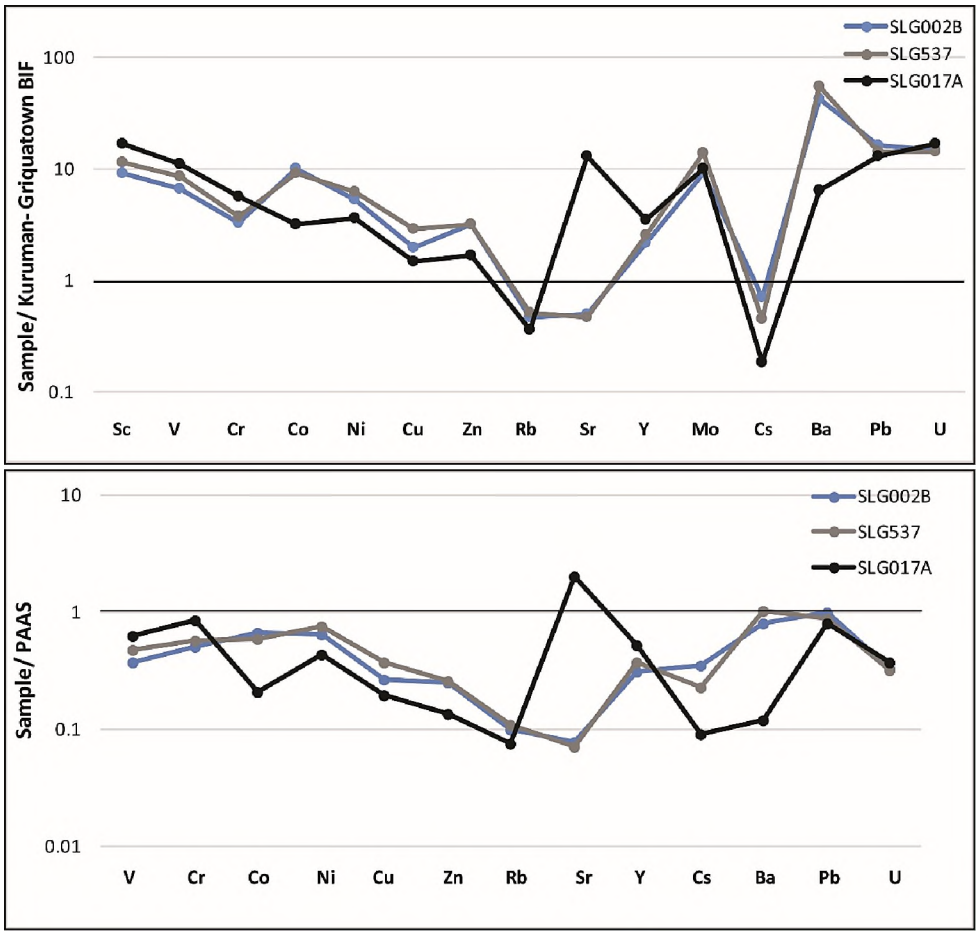

Figure 21: Trace elements of the three respective ore-zones compared to PAAS and Kuruman-Griquatown BIF.

An interesting feature of the plots in Figure 21 above, is the similarity between the profiles of boreholes SLG002B and SLG537, which track each other very closely, while the profile of borehole SLG017A is broadly similar, but does display some large variability relative to the other two.

4.3 Ore-Zone Rare Earth Elements

In a similar sense to the trace elements, the REE's are enriched relative to the Kuruman-Griquatown standard, but depleted relative to the PAAS standard. Relative to the Kuruman-Griquatown standard, the LREE's are all enriched by around 10x, while the HREE's are enriched between 5 and 10x the standard. Importantly, all of the profiles are very flat vs PAAS.

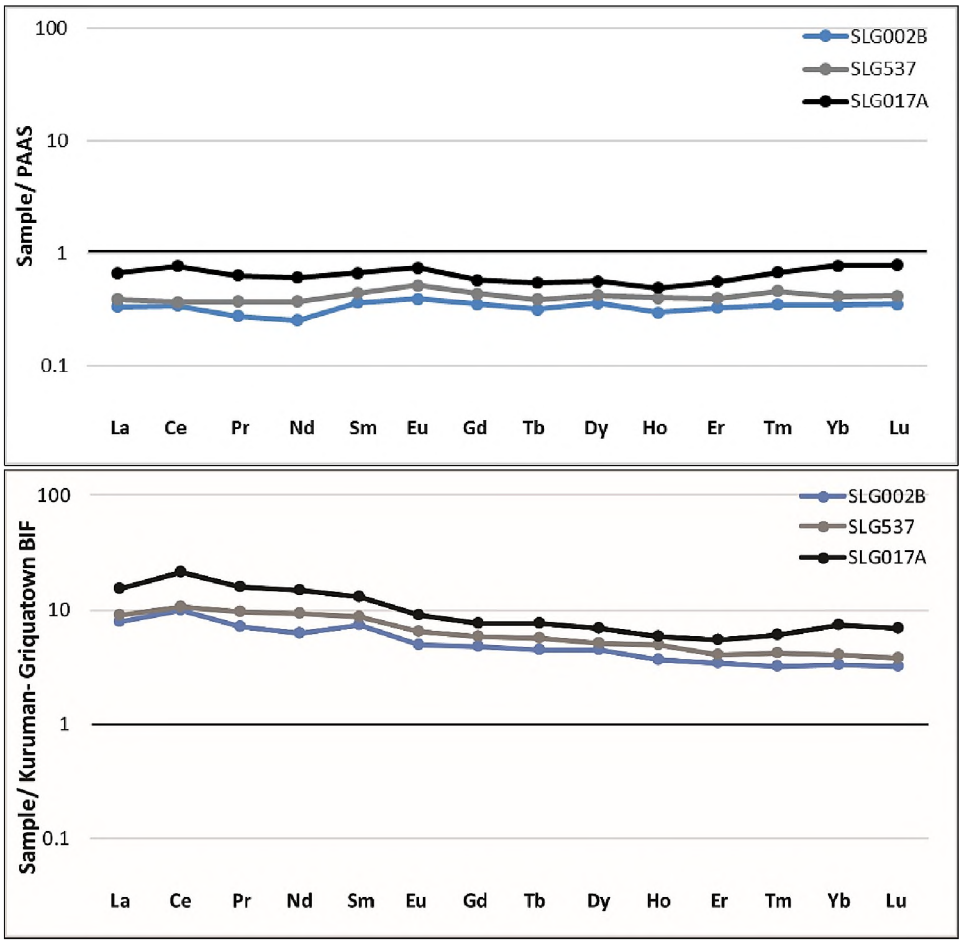

Figure 22: REE's from the 3 respective boreholes vs PAAS and Kuruman-Griquatown BIF.

4.4 Enriched-Zone Major Elements vs Ore-Zone

Due to the heterogeneous lithological composition of the enriched-zone, it has been normalized to PAAS. Figure 23 below presents, from top to bottom, boreholes: SLG002B, SLG537 and SLG017A, respectively. The diagrams present major element profiles from all the sampled units, in each borehole, and are compared to the average ore-zone major element composition for each respective borehole. The green profile in each diagram is the average ore-zone composition for the respective boreholes. The blues are the matrix-supported CGT profiles, the greys are the ferro-manganese units and the red represents the shale units (no shale unit in SLG537).

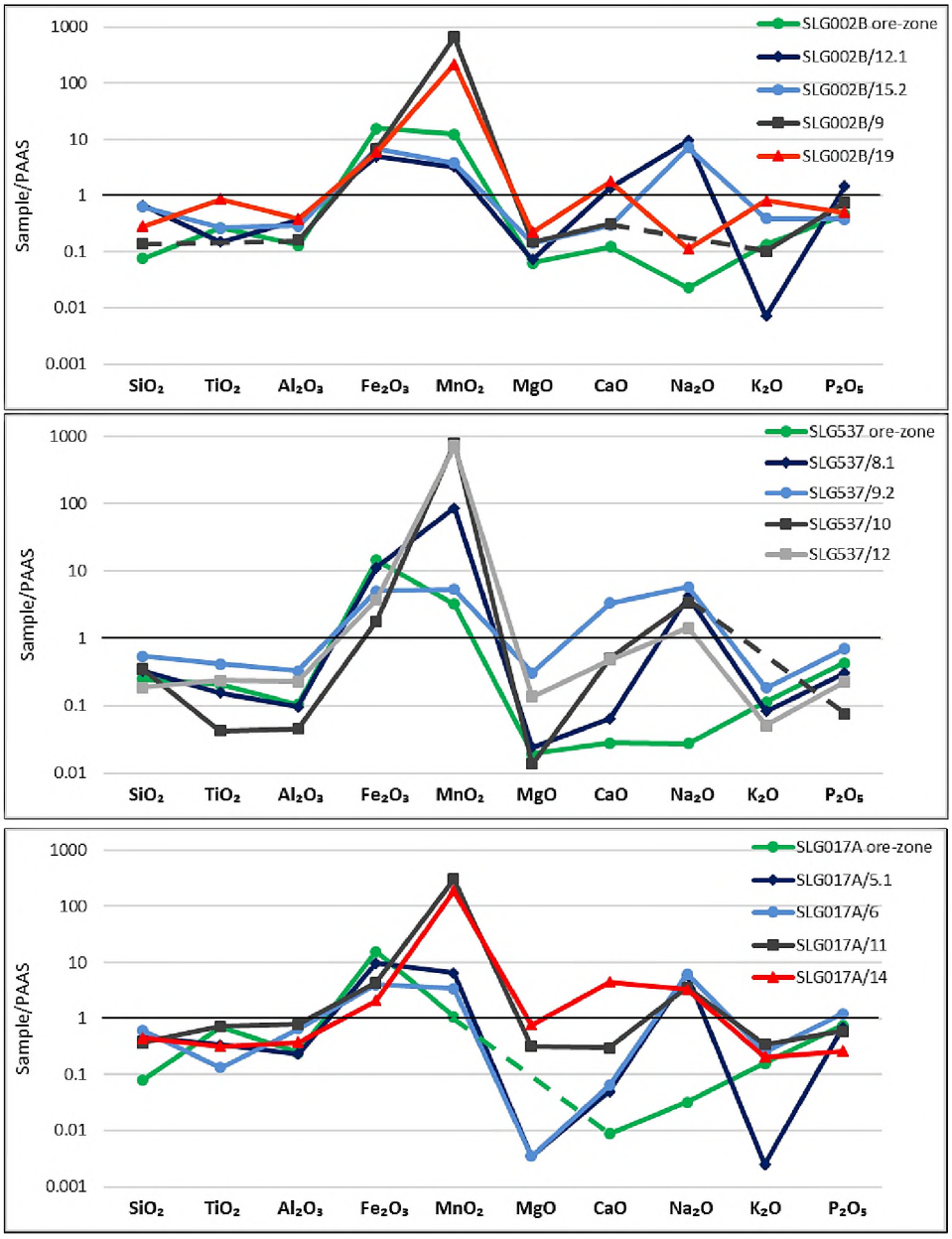

Figure 23: Major Element spider diagrams for the three boreholes normalized to PAAS. Included in each diagram is the average borehole concentration of each major element for the respective boreholes.

Looking at the plots above, it is important to consider that most of the profiles are from completely different lithological units – from a bulk rock perspective. Hence, the profiles are expectedly variable. However, it is evident that there are similarities that can be drawn across the three boreholes, as well as compared to the average ore-zone compositions in each borehole.

Across all three boreholes, there is a depletion in SiO_2, TiO_2 and Al_2O_3, followed by a consistent enrichment in Fe_2O_3 and MnO_2, while the rest of the major elements are largely depleted relative to PAAS.

Interestingly, the profiles of all samples in boreholes SLG537 and SLG017A display an enrichment in Na_2O. However, in SLG002B, there is a depletion in Na_2O in the sample SLG002B/19 (shale) and below the detection limit concentration of Na_2O in sample SLG002B/9 (ferro-manganese). The enrichment of CaO relative to PAAS in some samples comes as a result of the various carbonates found in the associated units.

Comparing the green ore-zone profile to the other profiles in each respective borehole, it is apparent that while the ore-zones are more conservative, they are broadly comparable with the rest of the units. The general profile of the three ore-zones depicts a depletion in SiO_2, TiO_2 and Al_2O_3, followed by an enrichment in Fe_2O_3 and MnO_2 – which is similar to the profiles of the other samples. Following on from MnO_2, the profiles become more erratic, as these major elements reflect larger variations in bulk-rock composition.

Importantly, from the diagrams above, there are noticeable trends, with samples from the same rock units in each borehole displaying similar profiles. One example of this is the high MnO_2 peak seen in the ferro-manganese units of each borehole, as well as in the shale units in boreholes SLG002B and SLG017A

4.5 Enriched-Zone Trace Elements vs Ore-Zone

For the purpose of consistency, the trace element samples have been normalized to PAAS. Trace element concentrations are presented in the same way as the major elements above – and retain the same colour scheme for each respective sample.

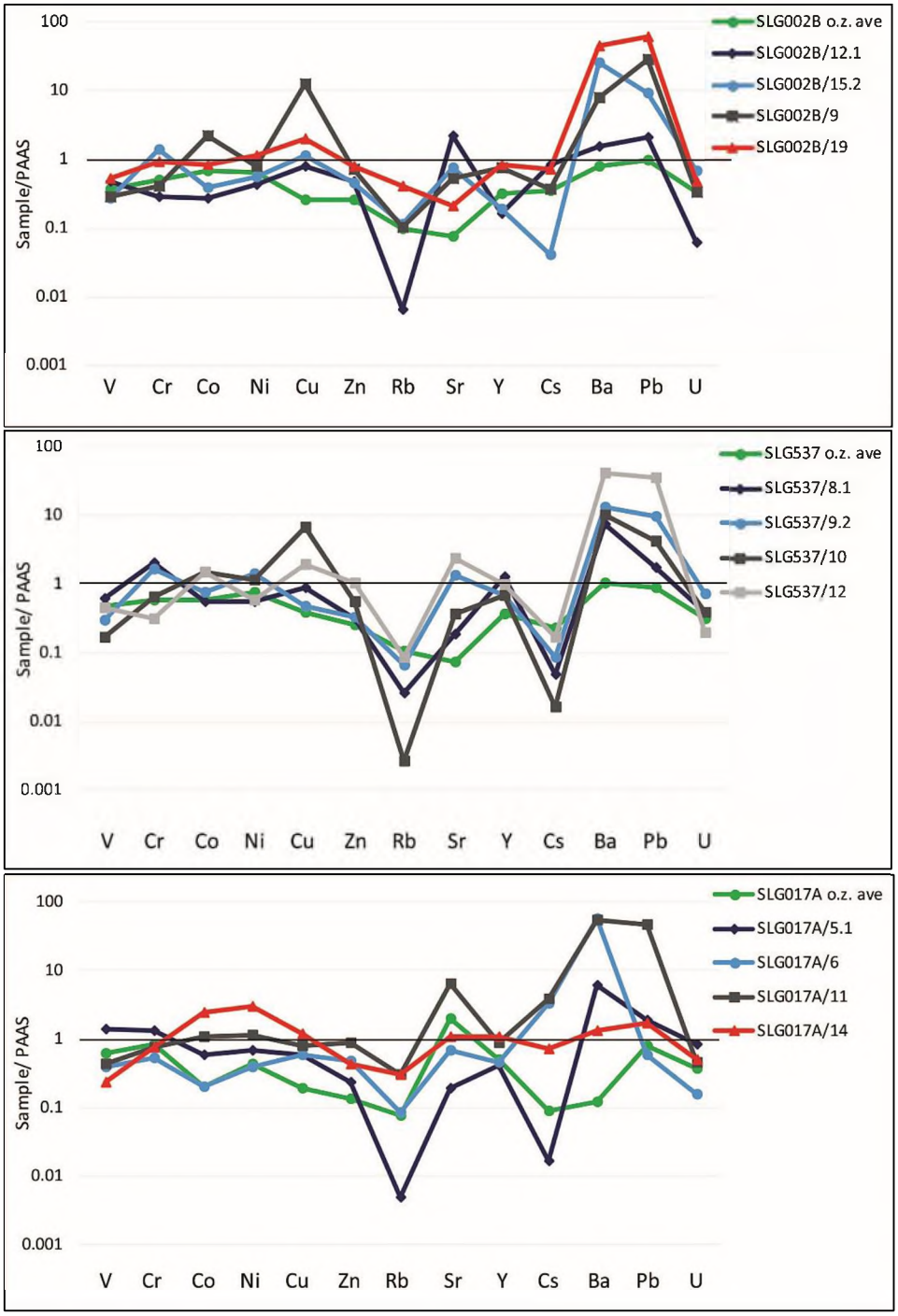

Figure 24: Trace element spider diagrams for the sampled units across the three boreholes. The average ore-zone concentration from each borehole is included.

Again, it is important to bear in mind that the profiles presented in the diagrams above are from different lithological units. They are also single sample analyses, rather than an average across a particular rock unit, therefore, there may also be a degree of sample bias. Having said that, it

would be remarkable to observe any similarities between the various profiles – and yet there clearly are. The exact concentrations of each trace element are not important here – as the accommodation of trace elements would largely depend on the bulk-rock composition, and the pre-existing minerals, along with their 'reactibility' with a hydrothermal fluid. Hence, the overall profiles of the various samples in relation to one-another, as well as the ore-zone average becomes important.

The profiles of the ore-zone averages in each diagram are naturally more conservative than the others (due to the overwhelming dominance of Fe-clasts and general ferruginization), however, the ore-zone profiles records many of the same enrichments and depletions as the other profiles. The degree to which the ore-zone correlates to the other samples is slightly different in each borehole, and evidently, borehole SLG537 displays the closest fit across all samples – including the ore-zone average. In fact, from Sr through to U, the ore-zone is identical to all of the other samples in terms of the general profile of borehole SLG537.

Although the trace elements indicate a broad correlation in terms of their general profile, there are expectedly stronger correlations between samples sourced from the same lithological units, within each borehole, and between correlative units of the other boreholes. Hence, the sub-chapter below presents the major element composition of the various units, and links it directly with the trace elements for that specific unit – affording a more defined composition in each unit.

4.6 Enriched-Zone: Combined Major and Trace Elements

4.6.1 Matrix-Supported CGT

The matrix-supported CGT displays a general enrichment in Fe_2O_3 and MnO_2, and Na_2O relative to PAAS. SiO_2, TiO_2 Fe_2O_3, Na_2O P_2O_5 are relatively conservative and uniform in their concentrations between the various samples and boreholes. MnO_2 is largely conservative, except for sample SLG537/8.1 which contains an unidentified manganese silicate, likely to be parsettensite. Hence, the majority of the oxides are very similar in terms of concentration;

however, MgO, CaO and K_2O display the most variability, with localized variations caused by the incorporation of these elements into a number of different phases.

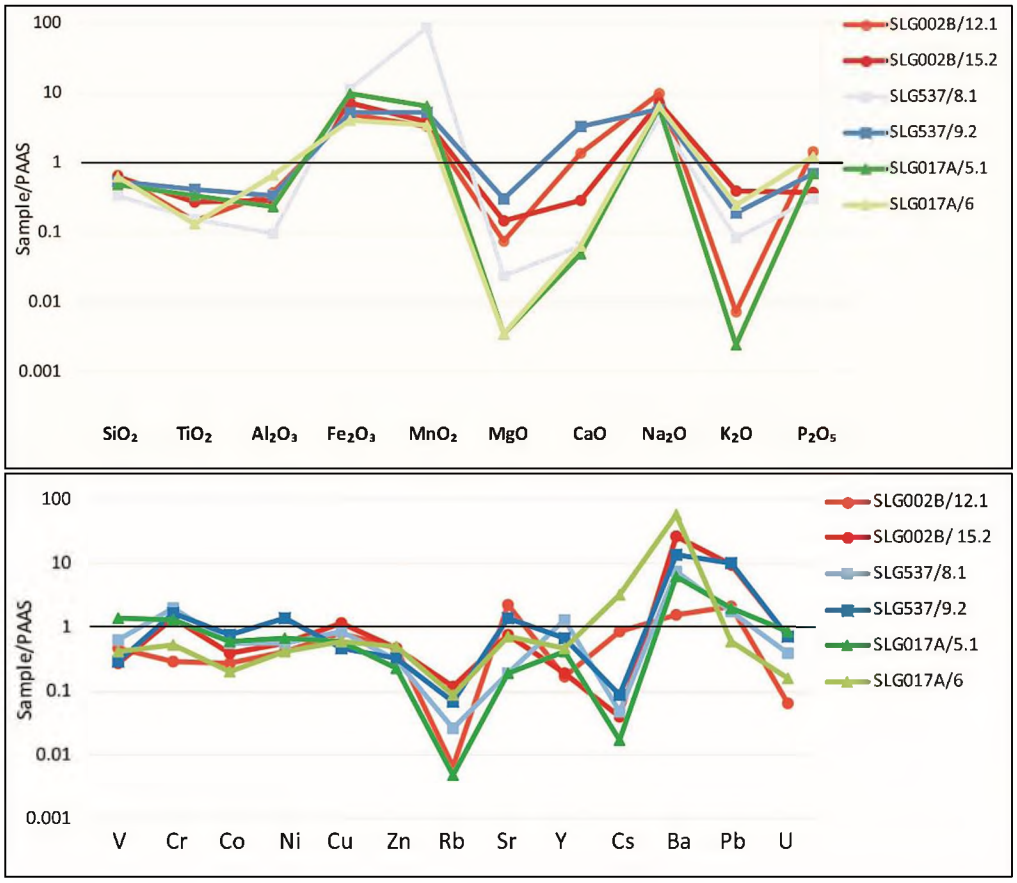

Figure 25: Major and trace element compositions relative to PAAS, for the various samples sourced from the matrix-supported CGT.

The trace elements of the matrix-supported CGT are relatively uniform between samples, and besides for Rb and Cs, they are generally only slightly depleted relative to PAAS. Ba and Pb, however, display a consistent enrichment relative to the standard, and for Ba, this peaks at around 90 times more enriched than PAAS for sample SLG017A/5.1

4.6.2 Ferro-Manganese unit

The ferro-manganese unit is expectedly rich in Mn, confirmed by the MnO_2 peak below – which reaches close to 1000 times the concentration of the standard in samples SLG537/10 and SLG537/12. Fe_2O_3 is enriched in all samples relative to PAAS. Na_2O is enriched in all samples, except for SLG002B/9. The dashed lines are indicative of below detection limit concentrations for TiO_2 in sample SLG002B/9, Na_2O in sample SLG002B/9 and K_2O in sample SLG537/10.

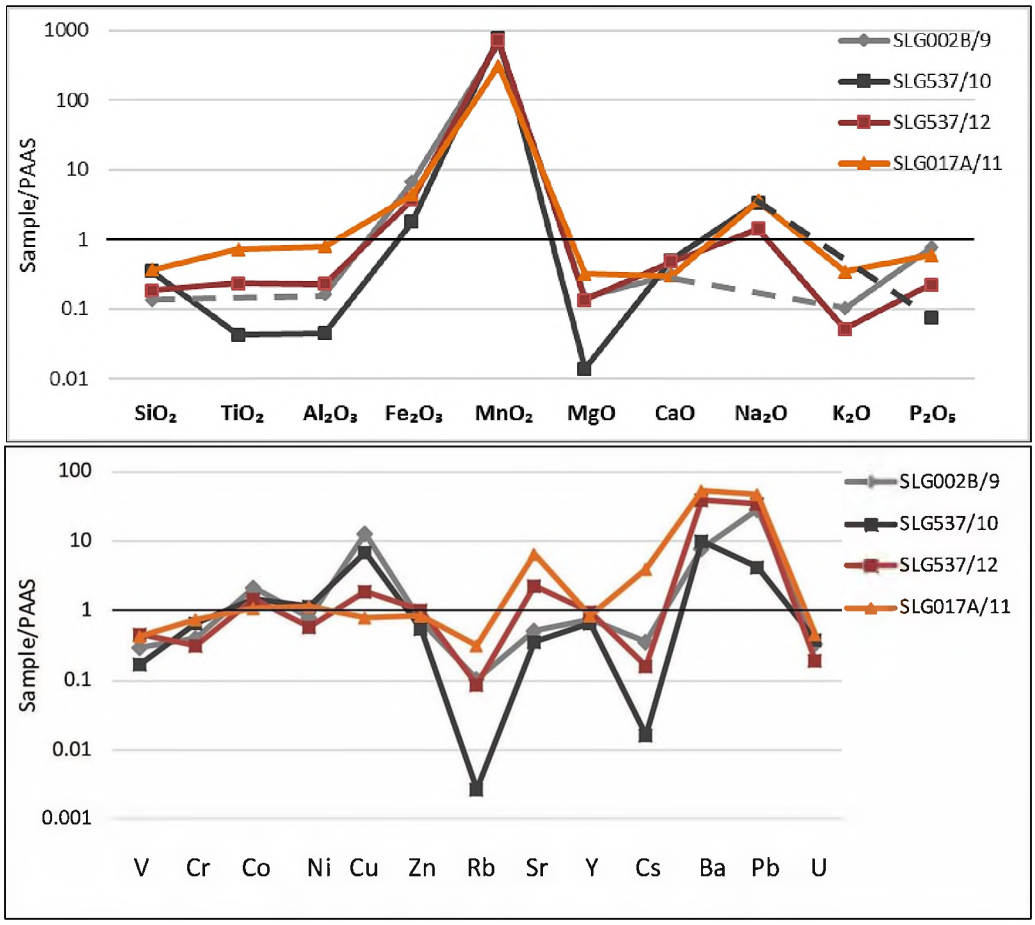

Figure 26: Major and trace element compositions relative to PAAS, for the various samples sourced from the ferro-manganese unit.

The trace elements for this unit are split between relatively conservative elements (V, Cr, Co, Ni, Y and U), and those which display large variability – such as Cu, Rb, Sr, Cs, Ba and Pb.

4.6.3 Shale unit

The shale unit is represented by two samples from different boreholes. Borehole SLG537 does not have a shale component at the base of the sampled stratigraphy.

There is evidently some variability between the two profiles, particularly between Na_2O and K_2O. These are likely to be as a result of sampling bias, where one particular sample contained more of a particular mineral. MnO_2 displays the strongest enrichment relative to PAAS, with both samples exceeding 100 times the concentration of the standard. This enrichment is attributed to the presence of hollandite, as well as the accommodation of Mn into calcite. The enrichment of CaO relative to PAAS is chiefly due to the presence of calcite.

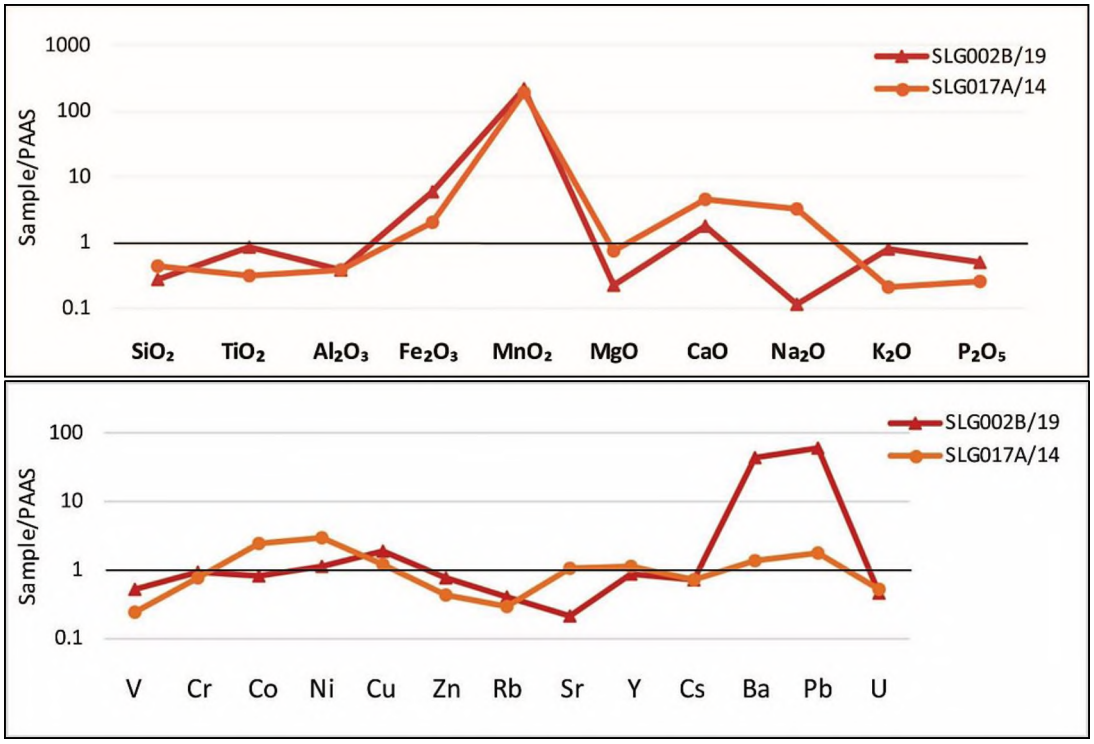

Figure 27: Major and trace element compositions relative to PAAS, for the samples sourced from the shale unit.

The profiles of the trace elements displayed above are noticeably more conservative than their counterparts in the other units – with the majority of elements hovering around the 1 line. This an expected result, considering that a shale unit is being compared to a shale standard. The barium and lead concentrations however, do appear particularly anomalous in sample SLG002B/19, at

around 80 times the concentration of the standard. The profile of SLG017A/14 records the same enrichment in Ba and Pb, just far more conservatively.

4.7 Enriched-Zone REE's vs Ore-Zone

The profiles of the average ore-zone concentrations are evidently more conservative than the samples from the enriched-zone. The profiles are generally flat, with the exception of an Eu anomaly in nearly all samples. A slight depletion in LREE's is present in some individual samples. The difference in concentration of REE's is a function of the different lithological units from which these samples are sourced. Confirmation of this is given by the red profiles (SLG002B/19 & SLG017A/14), which are sourced from the shale unit and have the closest general profile to 1. SLG537 does not contain a shale unit.

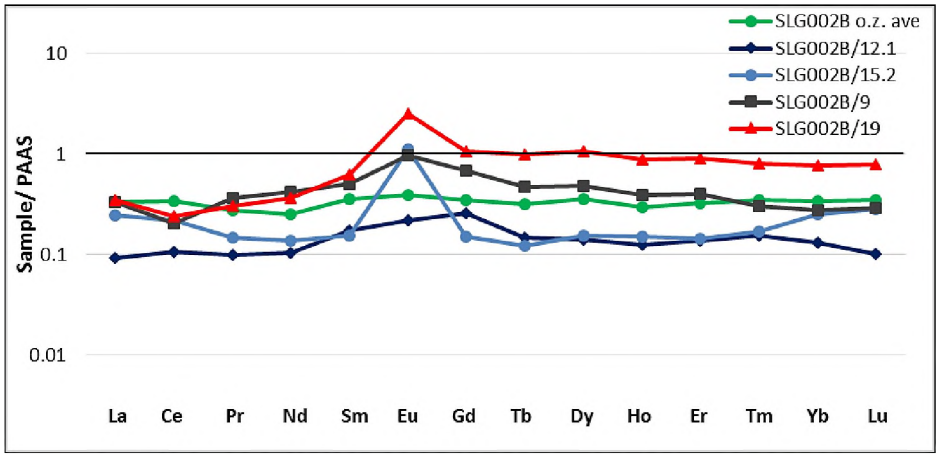

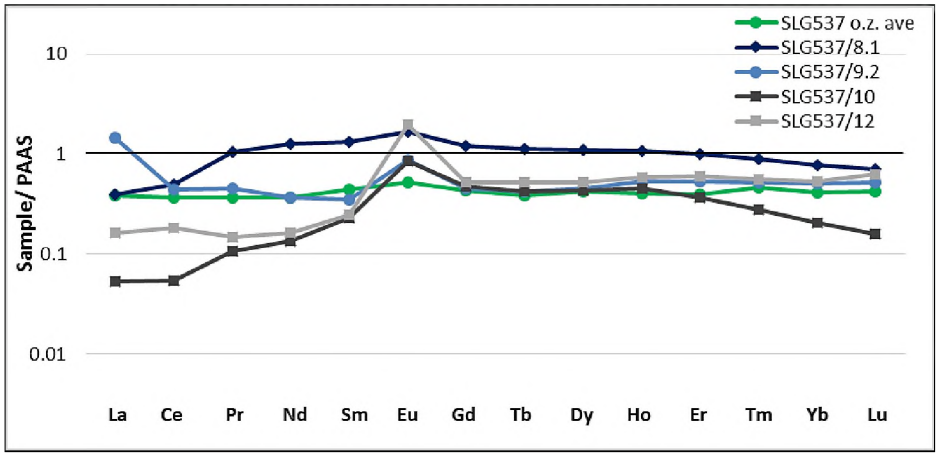

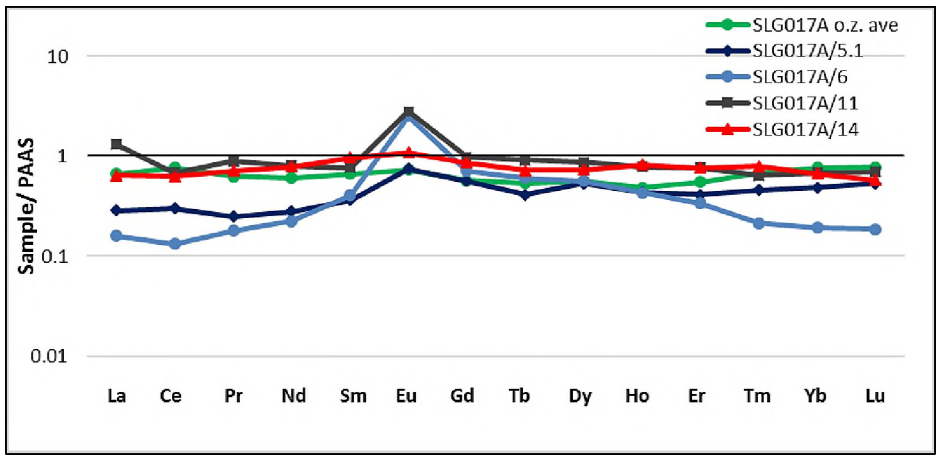

Figure 28: REE profiles relative to PAAS for all three boreholes. Enriched-zone samples are compared to the ore-zone average in each case.

4.8 Enriched-Zone Combined REE's

The vast majority of samples, from all lithological units are depleted in all REE's vs PAAS. In terms of LREE's vs HREE's, the profiles of samples from the matrix-supported CGT are flat, except for the Eu anomaly seen in all but one profile (SLG017A/6).

The majority of samples from the ferro-manganese unit indicate a depletion in LREE's, and all contain a distinct Eu anomaly, as does one sample (SLG002B/19) from the shale unit. The range of HREE concentrations in the ferro-manganese unit is more conservative than that of the matrix-supported CGT. Although there are just two samples from the shale units, the concentrations are expectedly close to 1 across all REE's.

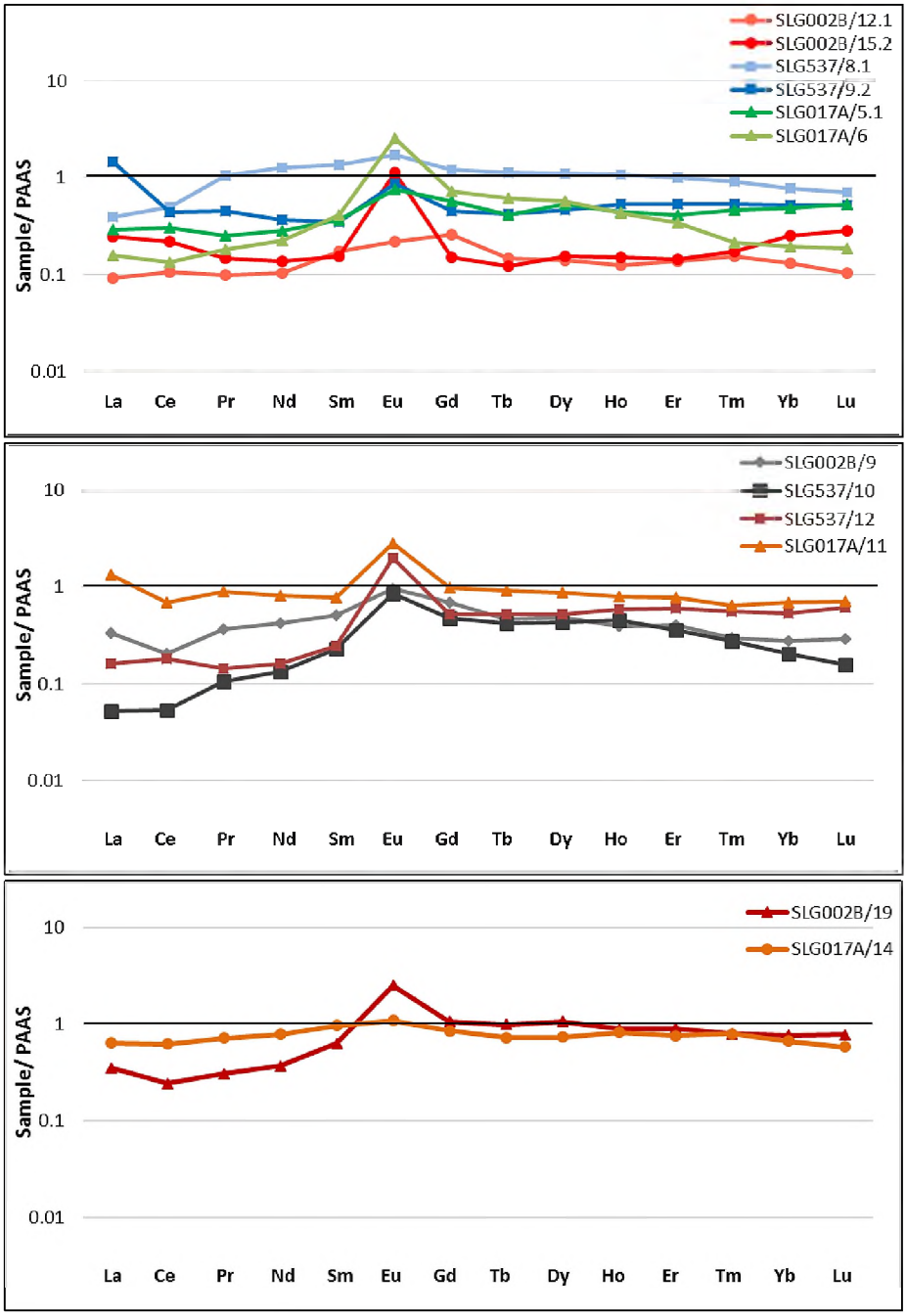

Figure 29: REE profiles relative to PAAS for each lithological unit. Top = matrix-supported CGT. Middle = ferro-manganese unit. Bottom = shale.

4.9 Key points to take from Chapter 4

- The ore-zone trace elements are enriched vs the Kuruman-Griquatown BIF standard, generally by enrichment factors of 5-10x, but sometimes far higher, as in the case of Ba (80x).
- The ore-zone REE's are depleted vs PAAS, but more importantly, the overall profile is very flat – which will be interpreted in the following chapter.
- Comparing trace and Rare Earth Elements between the ore-zones and the enriched-zones in each borehole, one notices that they are broadly correlatable, with the profiles displaying similar enrichments and depletions – even between different lithological units. The implications of this will be addressed in chapter 5.
- There is more consistency between the profiles taken from equivalent lithological units in each of the three boreholes – for major, trace and Rare Earth Elements.
- A number of samples are slightly depleted in LREE's, which will be discussed in the following chapter.

Chapter 5.

Synthesis

Previous work on the Postmasburg Manganese Field has largely focussed on the Maremane Dome, the ores of the eastern and western belts, and their respective mineralogy and models of formation. The presence of a number of minerals indicative of metasomatic processes in both the PMF and KMF, has previously been investigated by a number of authors, with results leading to casual suggestions of a link between the two deposits, in terms of a regional-scale hydrothermal fluid.

Current models on the formation of the PMF ores, such as those postulated by von-Plehwe Leisen and Klemm (1995), and Gutzmer and Beukes (1996a), pay little consideration to the potential influence of hydrothermal fluid on the process of ore-forming or upgrading.

This discussion takes a look at the evidence for the influence hydrothermal fluid in both the enriched zone and the ore zone, and addresses the possible links between the two, whether obvious or cryptic in nature. Comparisons to similar assemblages in the PMF, as well as occurrences in the KMF are made, together with an investigation into the possibility of a common, regional-scale hydrothermal process of formation for the alkali assemblages observed.

5.1 Petrographic evidence for metasomatism

This study has produced a wide-range of mineralogically complex assemblages, across four distinct lithological units. While some minerals appear to be bound to certain units, a large number are relatively pervasive throughout most lithological units. This sub-chapter investigates evidence for metasomatic processes in the context of the ore-zone and the enriched-zone, while also identifying evidence to support a connection between the two. below provides a summary of all minerals documented in the study, and their distribution throughout the various lithological units.

Table 14: Summary of all phases identified in this study

Name	Formula	Clast-supported conglomerate	Matrix-supported conglomerate	Ferro-manganese unit	Shale unit
Aegirine	$NaFeSi_2O_6$		X	X	
Albite	$NaAlSi_3O_8$		X		
Banalsite	$BaNa_2Al_4Si_4O_{16}$			X	
Barite	$BaSO_4$	X	X	X	X
Barytocalcite	$BaCa(CO_3)_2$		X	X	
Braunite	$Mn^{2+}Mn^{3+}{}_6[O_8\|SiO_4]$			X	
Calcite	$CaCO_3$		X	X	X
Celsian	$BaAlSi_3O_8$			X	
Hyalophane	$(K,Ba)Al(Si,Al)_3O_8$			X	
Fluorapatite	$Ca_5(PO_4)_3F$	X	X	X	
Hematite	Fe_2O_3	X	X	X	X
Hollandite	$Ba(Mn^{4+},Mn^{3+})_8O_{16}$			X	X
Hollandite-coronadite	$(Ba, Pb\ (Mn^{4+},Mn^{2+})_8O_{16})$			X	
K-feldspar	$KAlSi_3O_8$	X	X	X	X
Kutnohorite	$Ca(Mn^{2+},Mg, Fe^{2+})(CO_3)_2$	X			
Natrolite	$Na_2Al_2Si_3O_{10}\cdot H_2O$		X	X	
Quartz	SiO_2	X	X		X
Serandite	$Na(Mn^{2+},Ca)_2Si_3O_8(OH)$		X	X	
Witherite	$BaCO_3$		X		

5.1.1 Ore-Zone

The ore zones of the three boreholes are dominated by hematite and BIF clasts, with little matrix material between them. This zone is naturally less permeable than the matrix-supported CGT beneath it. However, despite this, there are still minerals of evidently metasomatic origin existing interstitially – albeit in limited abundance. These are barite, K-feldspar, fluorapatite and kutnohorite.

The barite is located either as individual crystals, or in association with K-feldspar, as is evident in Figure 35. Fluorapatite is commonly found in close association with K-feldspar and barite in vugs. Kutnohorite is only present in the ore zone of borehole SLG002B, where it contributes largely to the consistent Mn concentration of 1-3wt%. The rest of the Mn is located in selected hematite clasts. The separation of the carbonate veins on the basis of composition is captured well in back-scatter imagery Figure 11.(A), with the centre of the vein dominated by Ca, while the edges are more manganiferous. The backscatter imagery is complimented by a map of relative Mn concentration below, where the green edges of the vein are clearly marked out, as is the blue, Mn-depleted, Ca-rich centre.

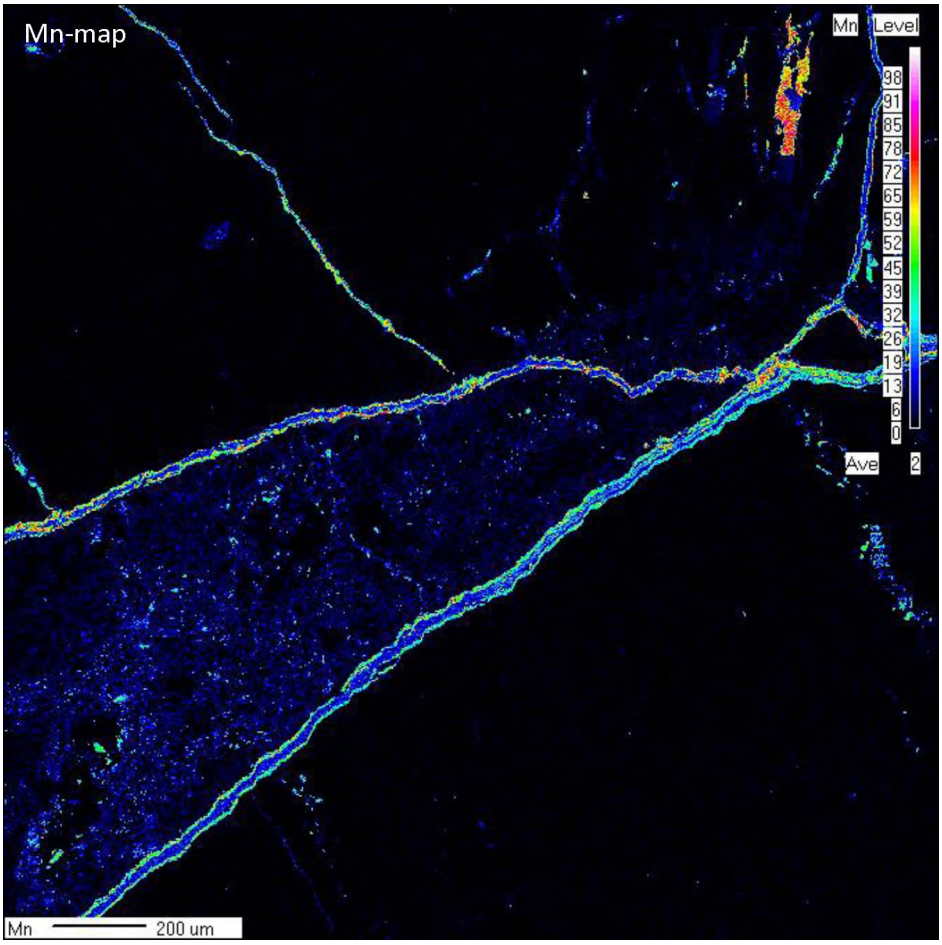

Figure 30: Mn-map indicating the distribution of manganese within the ore-zone, as well as the relative increase in Mn-concentration on the edges of the veins. *Scale represents counts/second.

Naturally, the veins are indicative of fluid movement through the ore zone. The fact that the veins travel along the path of least resistance, i.e. along the edges of the Fe-clasts, and only pass through the clasts where there is a clear brittle fracture, would suggest that this is a later fluid, that was introduced after the consolidation of the clasts into a competent lithological unit – and is likely separate from any process of ore formation. Where possible, the veins have exploited interstitial 'pockets', allowing for the fluid to pool.

5.1.2 Enriched-Zone

The enriched zone is typically more silica-rich and less-well consolidated than the ore zone.

The complexity of the mineral assemblages is evident in the wide variety of mineral species containing the same elements. The elements barium, sodium and manganese are particularly widespread, and have been incorporated in 7, 5 and 5 distinct minerals respectively. From Table 14 above, it is evident that the matrix-supported conglomerate and the ferro-manganese units are the most mineralogically diverse. Therefore, it comes as no surprise that these two interbedded units play host to what has previously been referred to as the 'enriched-zone' of alkalis.

In total, 17 distinct minerals, which host one or more of the target elements (Mn/Ba/Na), have been identified. In addition to this, there is also the solid solution between hollandite-coronadite, occurring in the ferro-manganese unit – in which barium and lead substitute for one another. The ferro-manganese unit also plays host to both celsian, and hyalophane – which is an intermediate composition in the celsian-orthoclase series (Mc Swiggen *et al*, 1994).

Aegirine is very common sodium bearing phase, existing both interstitially and in vugs along with albite. The occurrence of aegirine in close association with albite (Figure 14) has been previously documented in the PMF by de Villiers (1945). Later work on the formation of aegirine in the Fe-rich beds of the Hotazel Formation (KMF) by Tsikos and Moore (1997), lead the authors to the conclusion that the formation of aegirine is likely as a result of sodium-rich hydrothermal fluid flow interacting with dominantly hematite and quartz to form aegirine. Similarly, in this study, aegirine has been identified as a replacement of quartz/chert in laminated BIF clasts of the matrix-supported CGT – as observed in Figure 14.

Serandite has been identified both in veins, as-well-as replacing quartz in vugs (Figure 16). These findings are supported by Deer *et al* (1992), who suggest that this mineral is most commonly associated with low-temperature hydrothermal veins, or it occurs as a replacement mineral.

According to McSwiggen *et al* (1994), the paragenesis of hyalophane is considered to be very restricted, with this mineral typically being associated with sedimentary manganese and ferro-manganese deposits, or with Pb-Cu-Zn-Ba deposits. In a study by Mc Swiggen *et al*, (1994), the

presence of hyalophane and its associated genetic implications within a manganese-rich iron-formation, in the Cuyuna Iron Range, Minnesota, USA was analyzed. This study presents striking similarities to the current study, in the sense that both aegirine and hematite are found alongside hyalophane.

The occurrence of hyalophane in the assemblage has thrown into doubt the original interpretation of a Lake-Superior type deposit, where the presence of hyalophane would be atypical (Mc Swiggen *et al*, 1994). Instead, the authors have postulated that the barium-containing strata bare more resemblance to those associated with bedded manganese and ferromanganese deposits, and stratabound Pb-Zn-Cu-sulphide deposits (Mc Swiggen *et al*, 1994). These sulphide and sulphate deposits are considered to be of hydrothermal origin (Mc Swiggen *et al*, 1994; Page and Watson, 1976) with the source of the Ba in such an environment said to be from underlying oceanic basalts or barium-rich sediments (Mc Swiggen *et al*, 1994; Russel *et al*, 1994; Matsubara, 1985).

The formation of coronadite-hollandite series is indicative of the presence of varying amounts of both Ba and Pb in the ferro-manganese unit. According to Hewett (1971), coronadite is generally associated with supergene deposits, but has also been documented in hydrothermal veins and hot spring deposits. However, in this study, grains of coronadite-hollandite are not located in veins, but occur as fine-grained anhedral crystals within the matrix groundmass. This suggests that the barium was introduced through the veins, with some infiltrating into the groundmass and forming coronadite-hollandite, while the barium in the veins partitioned into the associated sulphide, carbonate and silicate phases associated with this unit – which include: barite, barytocalcite, banalsite, hyalophane and celsian. The latter two of which are the dominant Ba-bearing minerals in this unit. This is depicted very well in Figure 18, where a coronadite-hollandite grain is situated in close proximity (±100 micrometres) away from a vein dominated by hyalophane.

A number of carbonate minerals are present within the enriched zone, namely: calcite, barytocalcite and witherite – in order of abundance. These minerals commonly occur together, and witherite can be present as inclusions in either barytocalcite or calcite – Figure 15. These findings are supported by Deer *et al* (1992), who states that witherite – the second most common Ba-containing mineral on earth – is typically found in association with barytocalcite and barite, and occurrs either in low-temeprature hydrothermal veins, or as a replacement of barite.

Natrolite (Al-Na zeolite) was first described as a vug and fissure-filliing phase in basaltic flows by Cronstedt (1756) (Langella *et al*, 2001). Although zeolites most commonly occur in basaltic settings, they are also known to occur in a wide variety of other geological settings (Langella *et al*, 2001). Natrolite is common to sedimentary deposits, however, it usually occurrs as a result of hydrothermal activity related to igneous processes (Fairey, 2013; Gottardi and Galli, 1985). In this study, natrolite occurrs in vugs, and, where present, is usually the dominant vug-filling phase (Figure 15). This mineral is generally represented by medium-grained, anhedral crystals, and can contain inclusions of hyalophane. Such findings bare strong resemblance to a study by Fairey (2013), in which natrolite was identified as vug-fill in alki-rich rocks associated with the manganese deposits of the PMF.

Banalsite is a barium alumino-silicate typical of manganese deposits, occurring in veinlits and commonly associated with calcite and barite (Campbell-Smith *et al*, 1944). In this study, banalsite is strictly restricted to the ferro-manganese unit. These findings are supported by Fairey (2013) who reported fine-grained banalsite occurring in vugs and veinlets throughout the Mn-ore.

5.2 Implications of petrographic and geochemical observations: ore-zone vs enriched-zone.

As a rule, conglomerates, due to their mode of deposition and general heterogeneity, have the potential to be permeable. In terms of the degree of permeability, factors such as porosity, sorting and composition, amongst others, become important. Due to the increased Fe-clast content in the ore-zone, and the general ferruginization, the ore-zone is typically less susceptible to the movement of hydrothermal fluids than the enriched-zone.

In addition to permeability affecting fluid mobility, in order to make new minerals, the fluid has to be able to react with in-situ minerals to create new phases. Hence, the compositional characteristics of any given unit would largely dictate the metasomatic reaction with the infiltrating fluid. Bearing this in mind, an ore-zone consisting of predominantly oxides and very little silica would be far less likely to be able to produce the assemblages seen stratigraphically

below it, in the enriched-zone, where the silica content is likely to have been far greater – given the matrix-dominated nature of this unit. Therefore, it comes as no surprise that the mineralogy of the ore-zone is far more limited than that of the enriched-zone.

Bulk-rock geochemistry has afforded the opportunity for comparisons to be made between the ore-zone and the enriched-zone on a geochemical level. The major element profiles observed are largely reflective of the mineralogy observed in thin section, and often even subtle variations can be accounted for. One such example of this is the increase in MgO, CaO and MnO_2 in the ore-zone of borehole SLG002B relative to the ore-zones in the other boreholes – which is attributed to the presence of carbonate veins exploiting areas of weakness, and moving through the ferruginized material – often pooling interstitially where possible. Although only a limited number of samples from the enriched-zone were analyzed via X-Ray Fluorescence, the fact that there are clear correlations between many of the trace elements when comparing the enriched-zone to the ore-zone, presents a strong case for fluid mobility through both of these zones.

Ultimately, in each borehole, the profile of the average ore-zone trace elements is largely comparable to that of the other samples, not always in terms of enrichment relative to PAAS, but the general trend of the profile. This is suggestive of a fluid moving through the entire package, and leaving a largely reproducible trace element signature throughout all lithological units.

Expectedly, there are variations in the absolute concentrations of these trace elements both within each lithological unit, and between units. The ore-zone profiles are more conservative, and display less variation relative to samples from other units, and this is highly likely to be a function of fluids moving through a geochemically less-diverse zone, that is less conducive to accommodating introduced trace elements within a limited assemblage dominated by oxides. In the same way, the heterogeneity and increased silica content of the units in the enriched-zone beneath the ore-zone, afford more opportunity for trace elements to be incorporated into both new and existing phases. There can also be variability within the same rock unit, where fluid encounters an area of slightly different composition, and reacts with the pre-existing phases to form small-scale variations within a single unit. This can account for geochemical variations between samples sourced from the same unit. However, one of the most important observations from the ore-zone trace elements, is that the majority of them are enriched between 5-10x relative to the Kuruman-Griquatown standard. This result certainly has strong implications, for if

one simply had to consider an ore-zone protolith of 50% shale, 50% BIF, following upgrading, the trace element composition would only be increased 2x, however this cannot account for a 10-fold (or more) increase in these elements relative to the BIF standard used.

From the outset, it is clear that the behavior of the REE'S is very similar to that of the trace elements in two ways. 1) In both cases, the samples taken from the ore-zones are more conservative than the samples from the enriched-zones. 2) Both the trace element and REE data show enrichment relative to the Kuruman-Griquatown standard, and depletion relative to PAAS.

Additionally, the LREE's show the greatest enrichment, of around 10x relative to the Kuruman-Griquatown standard, and this drops off to between 5-10x in the HREE's. The majority of the profiles are flat relative to PAAS. This is most prominent in the ore-zone samples, which are particularly conservative. Interestingly, when comparing the profiles of the 3 ore-zones, they are remarkably similar to the Mapedi shales, recorded in a study by Land (2013) – as observed in Figure 31 below. Therefore, this is strongly suggestive of a shale protolith for these iron ore assemblages.

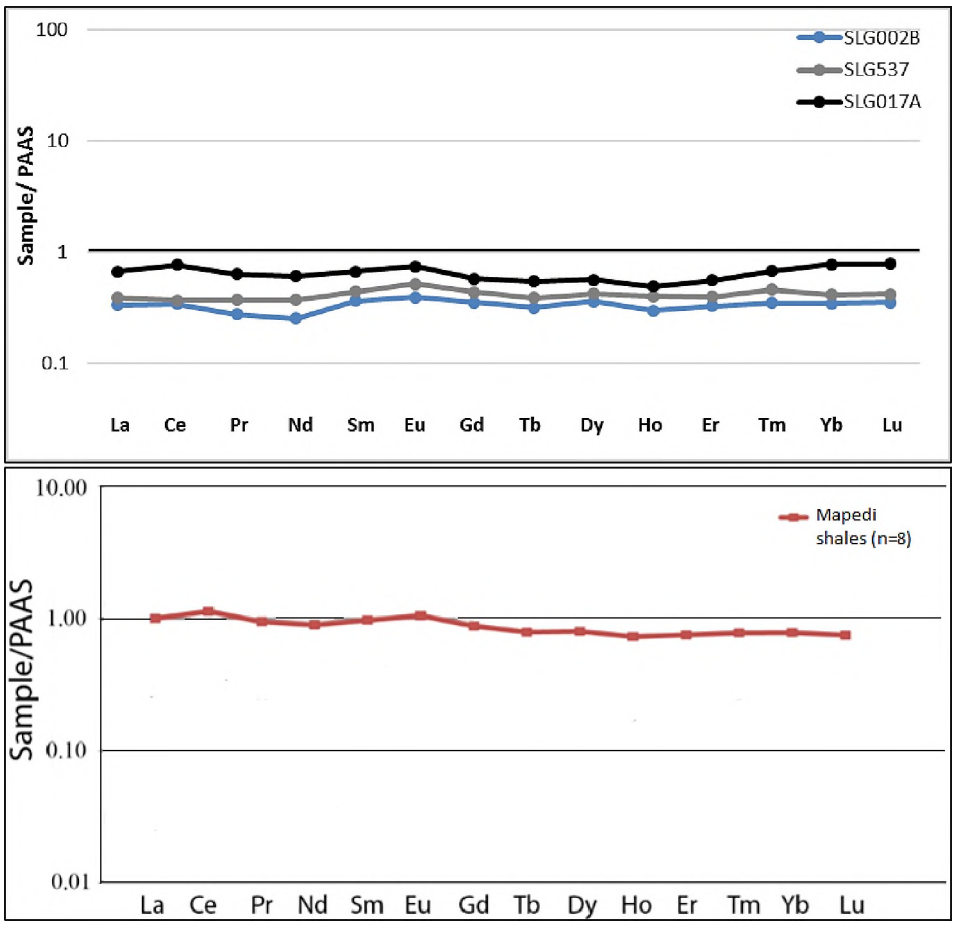

Figure 31: Top. Average REE composition for the 3 respective ore-zones relative to PAAS. Bottom. Mapedi shales relative to PAAS. Modified after Land (2013).

Another observation of interest, is the fact that many of the profiles in the enriched-zone display a depletion in LREE relative to HREE. A study by Gutzmer *et al.* (2008) investigated the controls on REE profiles in iron-ore deposits, and was able to classify deposits into either supergene or hydrothermal processes of formation based on their REE profiles. This study found that all supergene deposits display an enrichment in LREE relative to HREE – likely as a result of greater solubility of HREE in the presence of fluoride, hydroxide and carbonate anions (Nelson *et al.* 2003). The study also found that some deposits which display a depletion in LREE relative to HREE are hydrothermal in origin, but noted that this trend is due to the relative immobility of REE's, hence, they are simply displaying the original BIF pre-cursor signal, rather than an enrichment in HREE. It should be noted, however, that there are examples of

hydrothermal deposits which do not support the findings of the study by Gutzmer *et al*. (2008), such as the Hamersley iron ore deposit (Lobato *et al*. 2007) in Western Australia.

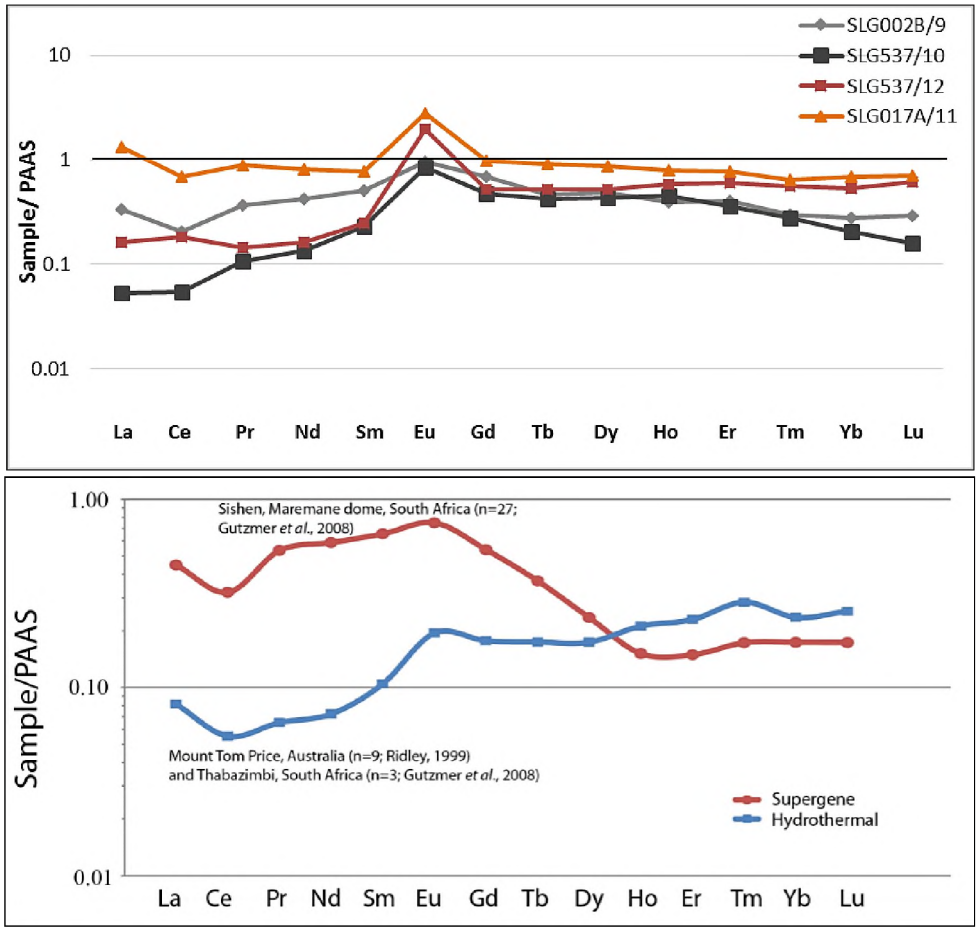

Figure 32: Top. Flat average REE ore-zone profiles. Middle. Depletion of some profiles in LREE's. Bottom. Supergene and hydrothermal models. Sourced from Land, (2013).

While the REE profiles of some of the samples may appear to be similar to that of the hydrothermal model, the author does not believe that these signals are truly hydrothermal, as they are observed throughout all units except for the ore-zone. This signal is displayed most prominently in the FEM unit, but also in one sample of the shale unit. One would not expect a BIF pre-cursor in these units.

5.3 Fluid characteristics and metasomatism

5.3.1 Potential sources of alkalis & metals

The process of metasomatism and ultimately, the formation of the observed assemblages, requires the movement of hydrothermal fluid through the entire package of rocks sampled for this study.

The enrichment in Na, Ba, and Mn has been continually highlighted throughout the study thus far, and, ultimately, the possible source of these elements does require addressing.

Indeed, it is possible that there could potentially be a link between the process of ore-formation/upgrading and the alkali-rich assemblage beneath it, i.e. fluid leaching material out of the ore-zone in a top down sense, and depositing it below, while simultaneously upgrading the ore-zone. Looking at Figure 20, Fe_2O_3 is enriched around 3x relative to the Kuruman-Griquatown BIF standard. However, many of the trace elements in Figure 21 display an enrichment of 5-10x greater than the standard, with some such as Ba, reaching as high as 80x greater than the Kuruman-Griquatown standard. Hence, while fluid leaching may have occurred on a small scale, the magnitude and pervasiveness of the alkali enrichment below, simply cannot be accounted for by such a simplistic 'top down' model, and the author does not believe that the processes of both ore-formation and alkali enrichment are related to the same event.

It is widely accepted that the manganese in these deposits is sourced from the dissolution of Mn-bearing carbonates, which would have formed a residual 'wad' at the base of karstic depressions. Unexpectedly, the highest concentrations of manganese are found within the ferro-manganese unit, which would represent the original 'wad'. However, the presence of manganese within other units, such as Mn-rich calcite in the shale unit, and serandite veining in the clast-supported CGT (to name but a few) is indicative of remobilized Mn – likely to be from partial remobilization of the original residual 'wad', and transported as $MnCl_2$.

Secondary, remobilized iron is commonly transported as chlorine complexes such as $FeCl^+$ and $FeCl_2^0$ – with the latter being favoured at higher temperatures (Heinrich and Seward, 1990). The solubility of iron in hydrothermal settings is controlled largely by the salinity and temperature of

the solution (Fein, 1992). The source of remobilized iron is likely to be local, as is the case with remobilized manganese.

Barium is the most diverse alkali, as it has been incorporated into 7 distinct minerals and one solid-solution series (hollandite-coronadite). Many of the Ba-containing minerals have been found to co-exist in vugs, such as witherite and barytocalcite – where witherite generally exists as an inclusion in barytocalcite. A feasible source of barium would be from the dissolution of evaporites. This could account for the sulphur required for the formation of the widespread barite observed throughout all units, including the ore-zone. However, the fact that barite is commonly found in association with other Ba-containing minerals, suggests that the hydrothermal fluid is sulphur impoverished, and once all the sulphur has been depleted, the barium is incorporated into other minerals. Furthermore, it is possible that the formation of barite may have resulted from the mixing of two or more fluids, with the sulphur coming from evaporites, and the barium, at least in part, coming from another source. This would provide an explanation as to why there is so much excess barium, after the precipitation of barite.

The widespread presence of Na-bearing minerals in these rocks is indicative of a Na-rich hydrothermal fluid. The source of the Na in these rocks is considered to have been derived from the banded iron-formations of the Transvaal Supergroup (Fairey *et al*, 2013). In addition to this, riebeckite and stilpnomelane have been recorded by Beukes and Klein (1990), within the Asbestos Hills Subgroup. The presence of stilpnomelane – $K(Fe^{2+}\ Mg;\ Fe^{3+})_8(Si;\ Al)_{12}(O;\ OH)_{27}$, provides a possible source for the potassium observed in these rocks. Of particular interest, is the k-feldspar in the ore-zones of the three boreholes, where it is commonly associated with barite and fluorapatite in vugs – Figure 35.

The presence of quartz in veins containing barite, is indicative of silica being carried in solution. These findings are supported by Papadopolous (2016), who also documented quartz forming in association with barite in rocks of the Manganore Iron Formation of the PMF. The solubility of SiO_2 is affected by pH, salinity and temperature. Experimental work by Dove and Nix (1997), indicates that the solubility of quartz increases in the presence of Mg^{2+}, Ca^{+}, K^{+}, and particularly Ba^{2+} – which increases the dissolution rate of quartz by 114X compared to deionized water. These experiments were carried out at 200 ˚C – which is an entirely feasible temperature to be associated with the formation of these assemblages.

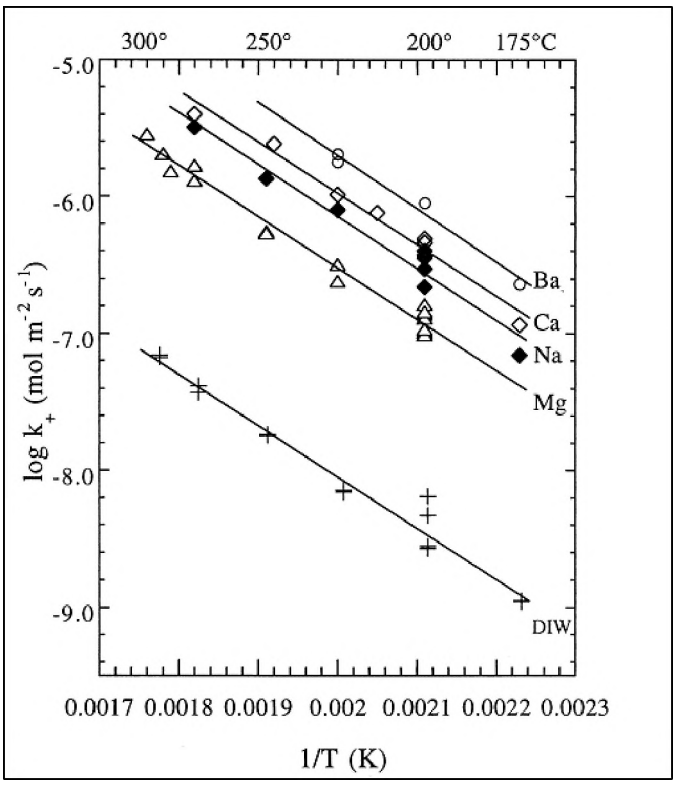

Figure 33: Arrhenius diagram showing the temperature dependence of quartz dissolution rates in DIW (deionized water). 0.05 M MgCl2, 0.05 M CaCl2, 0.04 M BaCl2 (E), and 0.15 M NaCl. All salt solutions have an in-situ pH of approximately 5.7 and an ionic strength of 0.15 except the data displayed for the 0.04 M BaCl2 solutions. (From Dove and Nix, 1997).

The effect of the respective chlorides on the dissolution of quartz is depicted in Figure 33 above. Evidently, temperature also plays a significant role in this, with a linear correlation between temperature and dissolution rate. The solubility of three important elements, transported as chlorides is presented in Figure 34 below.

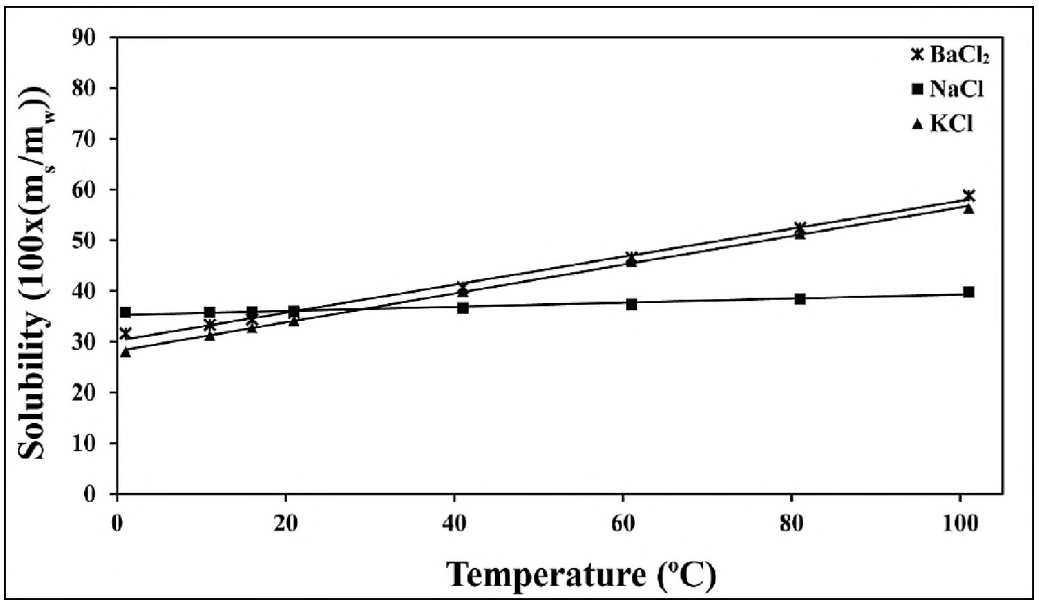

Figure 34: The effects of temperature on the solubility of $BaCl_2$, NaCl and KCl in water. (From Kaye and Laby, 1995).

The solubility of $BaCl_2$ and KCl in water is evidently very similar, with BaCl showing only a slightly greater solubility than KCl at any given temperature displayed. However, both $BaCl_2$ and KCl are more soluble than NaCl at temperatures greater than 28℃, and their response in solubility to temperature rise is far greater than that of NaCl.

In order to make accurate assumptions on the precipitation of fluid contents, one cannot only consider the effects of temperature, but other factors such as Eh, pH and composition should also be taken into account. Such factors are not readily available, but studies such as the one above, especially when supported by in-situ evidence, can provide insight into the fluid characteristics. The similarity in the solubility behaviour of $BaCl_2$ and KCl, would suggest that Ba and K should precipitate together – and this is exactly what is found in the vugs of the ore-zone samples, where the vug composition is limited to K-feldspar, barite and fluorapatite, and does not contain a sodic phase. The nature of these vugs is depicted in Figure 35 below.

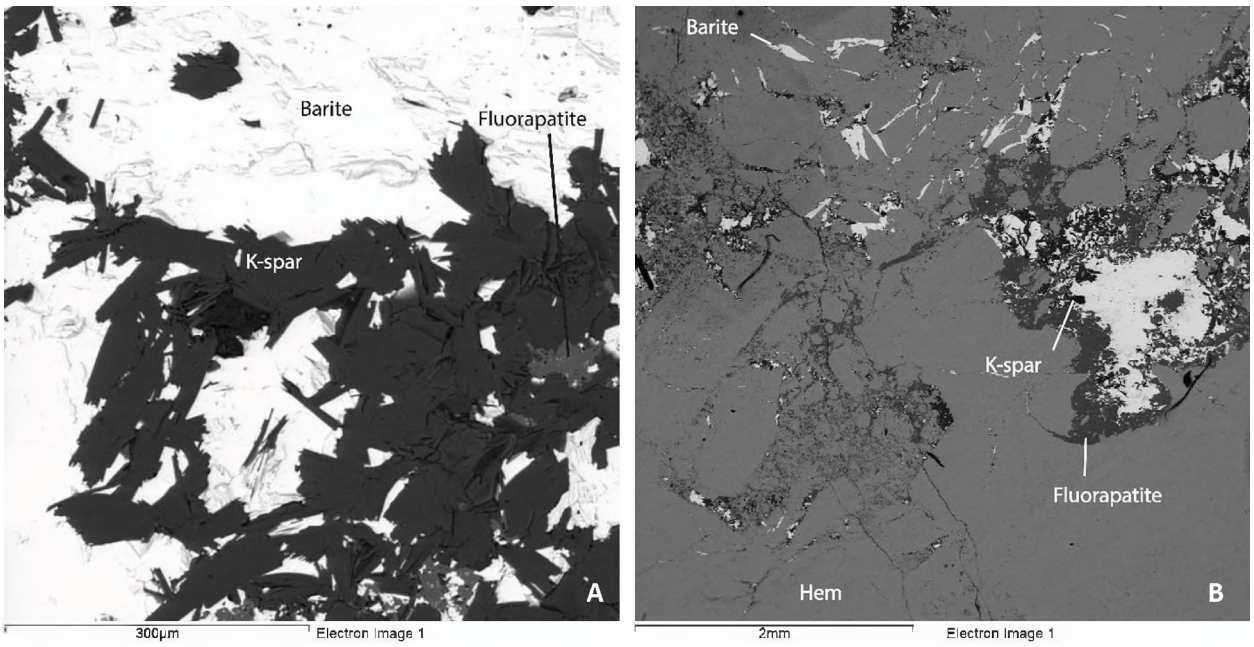

Figure 35: Relationship between K-spar, fluorapatite and barite in ore-zone vugs. **A**. close-up view of these 3 minerals. **B**. Vug-geometry, in a hematite dominant zone. Sample SLG537/1. Both **A** and **B** are backscatter images.

The fluorapatite and K-spar are consistently located on the edges, while the barite is the dominant phase in the centre of the vugs – evidently precipitating later. This supports Figure 34 above, which illustrates a slightly higher solubility of $BaCl_2$ than KCl.

5.3.2 Local-scale metasomatism

Evidently, these rocks have been affected by a process of hydrothermal fluid infiltration and associated alteration. It is likely that warm, deep seated brines moving through the basal rocks had the potential to dissolve minerals from the aforementioned sources, and carry their associated metals and alkalis in solution, as an evolving fluid. The elements Na, Ba, Mn, Pb, K, Ca and Si would have all been present in this solution. These elements may have travelled as chloride salt solutions. This movement would have been aided on a localized scale by two factors. 1) The heterogeneous, conglomeratic nature of some interbedded units. 2) The fractured nature of the non-conglomeratic units.

Vugs and fractures in the competent ore-zone have been exploited by fluids, which have moved through areas of less resistance en route to precipitating their compositions in favourable interstitial areas. Additionally, in the ore zone of borehole SLG002B, late carbonate veins have travelled along hematite clast boundaries, eventually precipitating interstitially as kutnohorite.

Pervasive vugs, veins and fracture-fillings, in the ferro-manganese and shale units have allowed for the movement of alkali-rich fluid through these units – as has been mapped in Figure 19 – which displays the sodic nature of the fracture-fill in the shale unit. Manganese has been remobilized, and incorporated into hollandite veins, as well as Mn-rich calcite in the shale unit.

Geochemical evidence strongly suggests that the fluids have made their way through the entire sampled package – given the similarity between many of the trace elements profiles from various samples and units. Given that the source of the alkalis is likely to be from older, stratigraphically deeper-lying rocks, the fluid is likely to have percolated through these rocks in a largely upward direction. Where enrichments or depletions in a given trace element occur, these are attributed to variations in the host rock, in terms of their reactibility and potential to host certain elements.

5.4 Implications of findings in a regional context

On a regional scale, many individual studies have highlighted the presence of alkali-rich rocks, existing either as 'pockets' or as bed-parallel assemblages. These alkali assemblages are recorded in association with both manganese and iron-ore deposits of the PMF and KMF.

One question which has yet to be satisfied, is that of whether all the individual alkali assemblages have formed as a result of localized episodes of hydrothermal fluid introduction and subsequent alkali metasomatism, or if all of these assemblages are related to the same hydrothermal system. Although there is much more work required before one can confidently argue a regional scale process of formation, it would be unjust not to at least highlight the similarities between the various deposits, and reason through the possibilities.

If one considers the minerals associated with these alkali assemblages, a large number of them are re-occurring in various locations in both the PMF and KMF. Furthermore, considering that many of these are complex minerals and solid-solutions, requiring specific conditions of

formation, it is difficult to fathom how their distribution could be so widespread, but for the presence of a common hydrothermal influence – of largely similar geochemical composition across the entire region, over a relatively short period of time.

Much has already been made of the similarity between the assemblages observed in this study, and those recorded in the study of Fairey (2013) – where the cations and associated mineralogy of the assemblages observed in karst-hosted manganese deposits are largely similar to the current study – and where differences occur, they are likely a function of host rock variability. In addition to this, Costin *et al*, (2011) and Moore *et al*, (2011), have also recorded the particularly high concentration of barium in the manganese ores of the Kathu-Postmasburg region.

In terms of comparisons to iron-ore deposits, a study by Moloto (2017), found Ba concentrations that are significantly enriched relative to the Kuruman BIF standard used – with samples containing a general enrichment of around 100x (but can be up to 1000x), greater than the Kuruman BIF standard. These findings are not dissimilar to this study, and although a slightly different standard is used, the average Ba concentration of between 10-100x greater within the three ore-zones is comparable.

Therefore, it is apparent the same chemical signals have been recorded at multiple sites, on a regional scale – regardless of the localized setting (manganese-ore/iron-ore). Such a widespread hydrothermal influence would surely require the assistance of regional scale tectonic processes and their associated structures, or the presence of unconformities – that are common to both the KMF and the PMF. It is difficult to pinpoint an exact conduit, but Fairey (2013) has identified two possible features. 1) The Blackridge Thrust fault – which is located on the Western Belt of the Maremane Dome, and considered by Gutzmer and Beukes (1996a) to have formed between 1.8 – 1.9 Ga. 2) The unconformity between the Transvaal and Olifantshoek Supergroups. The location of the Blackridge Thrust fault in relation to the Maremane Dome and its associated deposits is displayed in Figure 36 below.

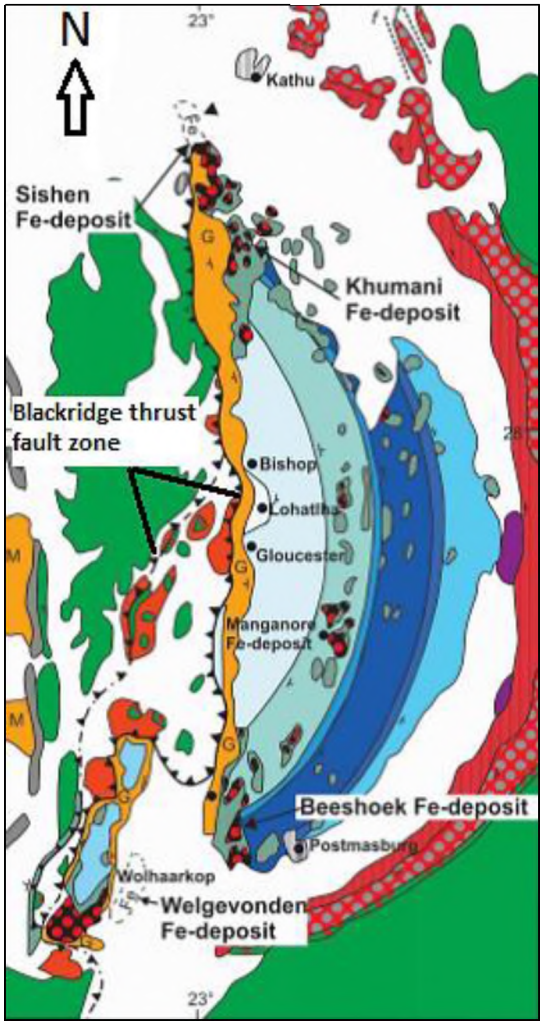

Figure 36: Map of the Maremane Dome and associated iron ore deposits, highlighting the Blackridge thrust fault. Modified after Smith and Beukes, (2006).

The Kheis and Namaqua are two orogenic events which could possibly be related to the hydrothermal fluid event – although dating of these events has proven difficult. Moen, (2006) describes the Kheis orogeny as older, forming around 1.8 Ga – while the Namaqua orogeny formed from 1.1 – 1.05 Ga. A number of attempts have been made to link the mineralogy with a certain event – but studies from different authors have yielded inconsistencies. Sugilite from the Wessels mine (KMF) was dated by Dixon, (1989), resulting in an age of 1350 ± 269 Ma – using Rb-Sr, and an age of 1270 ± 30 Ma using Pb-Pb. On the opposite end of the date spectrum is a study by Fairey *et al*, (2013), who dated limestones of the Mooidraai Formation (upper Transvaal Supergroup) which yielded a date of 590 ± 63 Ma.

Although there are discrepancies regarding the age and relative timing of a regional scale hydrothermal event, the evidence thus far is ever building. The similarities between alkali-rich assemblages across multiple sites cannot be ignored. However, in order to fully understand these processes, further investigation is required, with emphasis placed on certain areas which have the potential to prove or disprove the relationship between these deposits. The details of which are elaborated in sub-chapter 5.5.

5.5 Conclusions

The alkali-rich assemblages of the enriched-zone, have provided an ideal setting for studying and comparing these rocks to both the ore-zone above, as well as similar assemblages observed in the PMF, and further afield in the KMF. The most significant conclusions made during this study include:

1) Petrographic evidence of replacement textures, crosscutting features and a wide range of minerals of metasomatic origin indicate the prevalence of a strong hydrothermal overprint on these rocks.
2) The elevated concentrations of barium, sodium and manganese from the original assays have been attributed to 17 distinct minerals, which host one or more of these elements. The hollandite-coronadite solid-solution series also contributes towards the elevated concentrations of Mn & Ba in the ferro-manganese unit. Na and Ba are interpreted to have been introduced by the hydrothermal fluid, while Mn is likely to have been remobilized from the Mn-rich units by the infiltrating fluid.
3) Mineral chemistry (Probe & EDS) and mapping of veins and fractures has highlighted the strong relationship between these features and the elevated alkali concentrations observed – with hydrothermal fluid exploiting areas of weakness to penetrate and percolate through the various units.
4) Bulk-geochemistry has indicated a broad correlation between the trace element concentrations across all units in each borehole, as well as between the same units from different boreholes – including the respective ore-zones. This is strongly indicative of a hydrothermal fluid influence across all units. Further evidence for this is observed in the

ore-zone trace elements and REE's – which are all enriched by 5-10x relative to the BIF standard used. The REE's are also very similar to the Mapedi shales from Land, 2013 – which suggests a strong shale influence on the protolith of the ore.

5) The results of this study indicate that process of ferruginization and the associated upgrading of the clast-supported unit (ore-zone) is not related to that of alkali-enrichment beneath the ore-zone. This is based on the fact that a top down model would not be able to account for the extent of enrichment observed below, as well as the enrichment factors of certain trace elements being greater than that of Fe_2O_3.
6) Comparing the observed assemblages to those from other studies, the mineralogy is largely similar, even amongst units dominated by manganese ore. The introduced elements which make-up the minerals are evidently similar, and where differences in mineralogy occur, these are likely due to variations in host-rock reactibility and local conditions of mineral formation.
7) Although there is currently no solid evidence, the presence of alkali-rich rocks across the entire region of the KMF and PMF has allowed for questions to arise on the possible existence of a regional scale hydrothermal system. Although similarly undetermined, possible conduits for fluid flow may have involved, at least in part, the Blackridge Thrust Fault, and the unconformity between the Transvaal and Olifantshoek Supergroups.

5.6 Future research

Evidently, there remains a great deal to be understood about the alkali-rich deposits of the PMF and KMF. Although there is evidence to suggest that the alkali deposits on a regional scale are related, this opinion is largely based on the similarities seen between the deposits, in terms of mineralogy and trace element compositions.

However, in order to clarify the source of the deposits beyond doubt, and the possible link between them on a regional scale, more detailed analysis needs to be completed. Suggestions of this include: 1) Geochronology of datable minerals available, such as K-spar in vugs. Such evidence would serve to clarify the timing of the fluid introduction into these rocks. 2) To determine whether these regional-scale alkali deposits are related one another, the source of a

key component such as Ba, or Na would need to be further constrained. A regional-scale study currently underway, which includes analysis of Sr isotopes in the pervasive mineral – barite – could determine whether the source of Ba is the same at all sites. The outcome of this study will provide compelling evidence for whether or not these alkali deposits are related.

References

- Alchin, D., Lickfold, V., Mienie, P. J., Nel, D., & Strydom, M. 2008. An Integrated Exploration Approach to the Sishen South Iron Ore Deposit, Northern Cape Province, South Africa, and Its Implication for Developing a Structural and/or Resource Model for These Deposits. *Reviews in Economic Geology*, **15**, 317-338.
- Astrup J. and Tsikos H., 1998. Manganese. *In*: Wilson M.G.C. and Anhaeusser C.R. (Eds.), *The Mineral Resources of Southern Africa*. Handbook, Council for Geoscience, **16**, 450-460.
- Boggs, S. 2009. Petrology of Sedimentary Rocks. Cambridge University Press. London. 600 pp.
- Beukes, N.J. and Klein, C. 1990. Geochemistry and sedimentology of a facies transition – from microbanded to granular iron-formation – in the early Proterozoic Transvaal Supergroup, South Africa. *Precambrian Research,* **47**, 99-139.
- Beukes, N.J. and Smit, C.A., 1987. New evidence for thrust faulting in Griqualand West, South Africa: Implications for stratigraphy and the age of red beds: Geological Society of South Africa Transactions, **90**, 378-394.
- Beukes, N.J. 1978. Die Karbonaatgesteentes en Ysterformasies van die Transvaal Supergroep en Noord-Kaapland. Ph.D. thesis, Unpublished, Rand Afrikaans University, Johannesburg, 580 pp.
- Beukes, N. J., Gutzmer, J., & Mukhopadhyay, J. 2003. The geology and genesis of high-grade hematite iron ore deposits. *Transactions of the Institute of Mining and Metallurgy B - Applied Earth Sciences,* **112**, B18-B25.
- Boardman, L.G. 1964, Further geological data on the Postmasburg and Kuruman manganese ore deposits, Northern Cape Province, *in* Haughton, S.H. ed., geology of some ore deposits in South Africa: Johannesburg, Geological Society of South Africa, p. 415-440.
- Cairncross, B., and Beukes, N.J. 2013. *The Kalahari Manganese Filed – The Adventure Continues*. Cape Town. Random House Struik.

- Campbell Smith W., Bannister F.A. and Hex M.H., 1944. Banalsite, a new barium-feldspar from Wales. *The Mineralogical Magazine and Journal of the Mineralogical Society,* **27**, 33-47.
- Costin, G. Fairey, B.J. Tsikos, H. Gucsik, A. 2015. Tokyoite, As-rich tokyoite and noelbensonite: new occurrences from the Postmasburg Manganese Field, Northern Cape Province, South Africa. *The Canadian Mineralogist*, **53**, 981-990.
- Dalstra, H., & Guedes, S. 2004. Giant hydrothermal hematite deposits with Mg-Fe metasomatism: A comparison of the Carajas, Hamersley, and other ores. *Economic Geology,* **99**, 1793-1800.
- Decarreau, A., Petit, S.,Vieillard, P., Dabert, N. 2004. Hydrothermal synthesis of aegirine at 200 degrees C. *European Journal of Mineralogy*, **16**, 85-90.
- Deer W.A., Howie R.A. and Zussman J., 1992. An Introduction to the Rock-Forming Minerals (2nd ed.). Pearson Education Limited, Harlow.
- Deer, W. A., Howie, R. A. and Zussman, J. 1975. *An introduction to the rock forming minerals.* Longman, London, 528 pp.
- De Villiers, J. 1960. The manganese deposits of the Union of South Africa: Pretoria, Geological survey of South Africa, Handbook 2, 280 p.
- De Villiers, J. 1956. The manganese deposits of the Union of South Africa. International Geological Congress, 20th, Mexico City, Symposium del Manganeso, p. 40-52.
- Dixon R., 1989. Sugilite and associated metamorphic silicate minerals from Wessels mine, Kalahari manganese field. *Bulletin of the Geological Survey of South Africa,* **93**, 1-47.
- Dove, P.M., and Nix, C.J. 1997. The influence of the alkaline earth cations, magnesium, calcium, and barium on the dissolution kinetics of quartz. *Geochimica et Cosmochimica Acta,* **61**, 3329-3340.
- Eriksson, P.G., Altermann, W. and Hartzer, F.J. 2006. The Transvaal Supergroup and its precursors. In: Johnson, M.R., Anhaeusser, C.R. and Thomas, R.J. (Eds), The Geology of South Africa, Geological Society of South Africa and Council for Geoscience, Johannesburg, 237-260.

- Evans, D. A., Gutzmer, J., Beukes, N. J., & Kirschvink, J. L. 2001. Paleomagnetic constraints on ages of mineralization in the Kalahari Manganese Field, South Africa. *Economic Geology*, **96**, 621 - 631.
- Fairey, B.J. 2013. Genesis of karst-hosted manganese ores of the Postmasburg Manganese Field, South Africa with emphasis on evidence for hydrothermal processes. Unpublished MSc Thesis, Rhodes University, Grahamstown, South Africa.
- Fein, J.B., Hemley, J.J., D'Angelo, W.M., et al. 1992. Experimental study of iron-chloride complexing in hydrothermal fluids. *Geochimica et Cosmochimica Acta,* ***56***, 3179-1390.
- Fortey, N.J. and Michie, U.M. 1978. Aegirine of possible authigenic origin in Middle Devonian sediments in Caithness, Scotland. *Mineralogical Magazine*, **42**, 439-442.
- Gottardi, G. and Galli E., 1985. *Natural Zeolites*. Springer-Verlag, Berlin.
- Gutzmer, J. and Beukes, N.J. 1995. Fault-controlled metasomatic alteration of early Proterozoic sedimentary manganese ores in the Kalahari Manganese Field, South Africa, *Economic Geology*, **90**, 823-844.
- Gutzmer J. and Beukes N.J., 1996a. Karst-Hosted Fresh-Water Paleoproterozoic Manganese Deposits, Postmasburg, South Africa. *Economic Geology* **91**, 1435-1454.
- Gutzmer J. and Beukes N.J., 1996b. Mineral paragenesis of the Kalahari manganese field, South Africa. *Ore Geology Reviews* **11**, 405-428.
- Gutzmer, J. and Beukes, N.J. 1997. Effects of mass transfer, compaction and secondary porosity on hydrothermal upgrading of Paleoproterozioc sedimentary manganese ore in the Kalahari manganese field, South Africa. *Mineralium Deposita*, **32**, 250-256.
- Gutzmer, J., Chisonga, B. C., Beukes, N. J., & Mukhopadhyay, J. 2008. The Geochemistry of Banded Iron Formation-Hosted High-Grade Hematite-Martite Iron Ores. *Reviews in Economic Geology* **15**, 157-183.
- Grout, F, F. 1946. Acmite occurrences in the Cuyana Range, Minnesota. *American Mineralogist*, **31**, 125-30.
- Grobbelaar, W. S., Burger, M. A., Pretorius, A. I., Marais, W., & van Niekerk, I. J. 1995. Stratigraphic and structural setting of the Griqualand West and the Olifantshoek Sequences at Black Rock, Beeshoek and Rooinekke Mines, Griqualand West, South Africa. *Mineralium Deposita* **30**, 152-161.

- Grout, F,F. 1946. Acmite occurrences on the Cuyuna Range, Minnesota. *American Mineralogist*, **31**, 125–30.
- Holland, H.D, and Beukes, N.J. 1990. A paleoweathering profile from Griquland West, South Africa: Evidence for a dramatic rise in atmospheric oxygen between 2.2 and 1.9 by BP. *American Journal of Science*, **90**, 1-34.
- Heinrich, C.A. and Seward, T.M. 1990. A spectrophotometric study of aqueous iron (II) chloride complexing from 25 to 200°C. *Geochimica et Cosmochimica Acta*, **54**, 2207-2221.
- Hewett. D.F. 1971. Coronadite; modes of occurrence and origin. *Economic Geology*, **66**, 164-177.
- Kato, A., Matsubara, S. and Watanabe, T. 1987. Banalsite and serandite from the Shiromaru mine, Tokyo. *Bulletin of the National Science Museum*, **13**, 107-114.
- Kaye and Laby, 1995. *Tables of Physical & Chemical Constants (16th edition 1995). 2.1.4 Hygrometry. Kaye & Laby Online. Version 1.0 (2005).* Available: www.kayelaby.npl.co.uk (20/10/2017).
- Land, J.S., Tsikos, H., Cousins, D.P., Luvizotto, T.Z., Beukes, N.J., (In review). Origin of paleosols and red beds in the Palaeoproterozoic Transvaal and Olifantshoek Supergroups of South Africa: provenance *versus* metasomatic controls. *Geological Journal, Wiley.*
- Langella, A., Cappelletti, P., de' Gennaro, R. 2001. Zeolites in Closed Hydrologic Systems. *Reviews in Mineralogy and Geochemistry* **45**, 235-260.
- Leisen, H. 1987. Geologisch-tektonische Kartierung der Griqualand West and Olifantshoek Sequenzen in der N/Srdlichen Kapprovinz, Siidafrika, auf der Grundlage yon Landsat-Mss-Daten und terrestrisch-photogrammetrischen Aufnahmen. Unpublished Ph.D.-thesis, Ludwig-Maximilian-University.
- Likhoydov, G.G. 1981. Stability of the aegirine-quartz-hematite association as shown by experimental data. *Doklady Academy of Sciences of the USSR, Earth Sciences Section*, **242**, 174-176.
- Lobato, L. M., Figueiredo e Silva, R. C., Hagemann, S., & Thorne, W. 2007. Mineralizing fluid evolution and REE patterns for the hydrothermal Carajas iron ores, Brazil, and for selected Hamersley iron deposits, Australia. *In: 9th Biennial Society for Geology Applied to Mineral Deposits, SGA meeting, Dublin, Ireland*, 1227 - 1230.

- Matsubara, S. 1985. The mineralogical implication of barium and strontium silicates. *Bulletin of the National Science Museum*, **11**, 37-95.
- McSwiggen, P.L., Morey, G.B., and Cleland, M. 1994. Occurrence and genetic implications of hyalophane in manganese-rich iron-formation, Cuyuna Iron Range, Minnesota, USA. *Mineralogical Magazine*, **58**, 387-399.
- Moen, H.F.G. 2006. The Olifantshoek Supergroup. *In*: Johnson M.R., Anhaeusser C.R. and Thomas R.J. (Eds.), *The Geology of South Africa*. Geological Society of South Africa, Johannesburg.
- Moloto, W. 2017. A bulk and fraction-specific geochemical study of the origin of diverse high-grade hematitic iron ores from the Transvaal Supergroup, Northern Cape Province, South Africa. Unpublished MSc Thesis, Rhodes University, Grahamstown, South Africa.
- Moore J.M., Kuhn B.K., Mark D.F. and Tsikos H., 2011. A sugilite-bearing assemblage from the Wolhaarkop breccia, Bruce iron-ore mine, South Africa: Evidence for alkali metasomatism and ^{40}Ar-^{39}Ar dating. *European Journal of Mineralogy,* **23**, 661-673.
- Moore, J. M., Tsikos, H., & Polteau, S. 2001. Deconstructing the Transvaal Supergroup, South Africa: Implication for Palaeoproterozoic palaeoclimate models. *Journal of African Earth Sciences* **33**, 437-444.
- Nakano S. 1979. Intergrowth of barium microcline, hyalophane and albite in the barium-containing alkali feldspar from the Noda-Tamagawa mine, Iwate Prefecture, Japan. *Mineralogical Journal,* **9**, 409-416.
- Nelson, B. J., Wood, S. A., & Osiensky, J. L. 2003. Partitioning of REE between solution and particulate matter in natural waters: A filtration experiment. *Journal of Solid State Chemistry,* **171**, 51-56.
- Papadopoulos, V. 2016. Mineralogical and geochemical constraints on the origin, alteration history and metallogenic significance of the Manganore iron-formation, Northern Cape Province, South Africa. Unpublished MSc Thesis, Rhodes University, Grahamstown, South Africa.
- Page, D. C. and Watson, M. D. 1976. The Pb-Zn deposit of the Rosh Pinah Mine, South West Africa. *Economic Geology*, **71**, 306-327.

- Taylor, D. J., Dalstra, H. J., Harding, A. E., Broadbent, G. C., & Barley, M. E. 2001. Genesis of high-grade hematite orebodies of the Hamersley Province, Western Australia. *Economic Geology* **96**, 837 - 873.
- Tsikos H. and Moore J.M. 1997. Petrography and Geochemistry of the Paleoproterozoic Hotazel Iron-Formation, Kalahari Manganese Field, South Africa: Implications for Precambrian Manganese Metallogenesis. *Economic Geology,* **92**, 87-97.
- Tsikos H. and Moore J.M., 2005. Sodic metasomatism in the Palaeoproterozoic Hotazel iron-formation, Transvaal Supergroup, South Africa: implications for fluid-rock interaction in the Kalahari manganese field. *Geofluids,* **5**, 264-271.
- Tsikos H., Beukes N.J., Moore J.M. and Harris C. 2003. Deposition, diagenesis and secondary enrichment of metals in the Palaeoproterozoic Hotazel Iron Formation, Kalahari Manganese Field, South Africa. *Economic Geology,* **98**, 1449-1462.
- Plehwe-Leisen E. von and Klemm D.D., 1995. Geology and ore genesis of the manganese ore deposits of the Postmasburg manganese-field, South Africa. *Mineralium Deposita,* **30**, 257-267.
- Russell, M. J., Hall, A. J., Willan, R. C. R., Allison, I., Anderton, R. and Bowes, G. 1984. On the origin of the Aberfeldy celsian + baryte + basemetal deposits, Scotland. In Symposium on prospecting in areas of glaciated terrain, Glasgow, Scotland (M. J. Gallagher, ed.), 158-70.
- Shao-Yong, J., Ru-Cheng, W., Xi-Sheng, X.,Kui-Dong, Z. 2005. Mobility of high field strength elements (HFSE) in magmatic-, metamorphic-, and submarine-hydrothermal systems. *Physics and Chemistry of the Earth,* **30**, 1020-1029.
- Smith, A.J.B. and Beukes, N.J. 2006. Palaeoproterozoic banded iron formation hosted high-grade hematite iron ore deposits of the Transvaal Supergroup, South Africa. *Episodes,* **39**, 269-284.
- Truter, F.C., Wasserstein, B., Botha, P.R., Visser, D.J.L., Boardman, L.G., and Paver, G.L., 1938. The geology and mineral deposits of the Olifantshoek area, Cape Province: Pretoria, Geological Survey of South Africa, Explanation to sheet 173, 107p.
- Viswanathan, K. and Kielhorn, H. M. 1983 Variations in the chemical compositions and lattice dimensions of (Ba,K,Na)-feldspars from Otjosondu, Namibia and their significance. *American Mineralogist*, **68**, 112-21.

Appendix I

List of abbreviations

CGT	Conglomerate
CPL	Cross-polarized light
KMF	Kalahari Manganese Field
LOI	Loss on ignition
PMF	Postmasburg Manganese Field
PPL	Plane-polarized light
PPM	Parts per million
Wt. %	Weight percent

Appendix II

i. Sample preparation

Polished thin sections for petrographical and microprobe analysis were prepared in house. Powders for XRF analysis were also prepared in house, using a swing mill containing hardened steel rings. The swing mill was first cleaned with detergent and distilled water, after which it was dried with acetone and pressured air. Quartzite was then run through the mill, to remove any contamination which may have remained. The cleaning process was repeated. The ore-zone samples were crushed first, and these were run for 2.5 minutes each, which was enough to mill the powder to the required standard. Between each sample, a quartzite batch was run to eliminate contamination. With regard to the enriched-zone samples, the matrix material was favoured, in an attempt to eliminate the influence of Fe-clasts where present. Therefore, a drill was used to extract the matrix material, and where applicable, a pencil and mortar. The matrix material was run for 2 minutes in the swing mill.

i.i. Determination of H_2O^- and loss on ignition (LOI)

The H_2O^- (wt. %) and LOI (wt. %) were determined at Stellenbosch University, department of Geology. Silica crucibles were used to hold the powdered samples. The crucibles were initially cleaned with distilled water and then left to dry in an oven at 110°C for 2 hours. They were then left to cool in a desiccator. The crucibles were then weighed to the fourth decimal place. 1.5 grams of sample was placed in the crucibles, after which the mass of the sample and crucible were recorded to the fourth decimal. The sample was dried at 110°C for a minimum of 4 hours then placed in a desiccator to cool. The difference in mass between the sample and crucible before and after drying was recorded, and this represents the H_2O of the sample. Following this, the same samples were ignited for a minimum of 8 hours at 950°C in a blast furnace. The samples were then left in a desiccator to cool. Finally, each sample was reweighed in order to determine the mass of the material lost due to heating (LOI).

i.i.i. X-Ray Fluorescence (XRF)

Glass disks were prepared for XRF analysis using 7.3 g of ultra-high purity trace element and Rare Earth Element-free flux (LiBO2=49.75%, Li2B4O7=49.75% LiI=0.50%) mixed with 0.4g of the pulverized sample. Whole-rock major element compositions were determined by XRF spectrometry on a PANalytical Axios Wavelength Dispersive spectrometer at the Central of Analytical Facilities, Stellenbosch University, South Africa. The spectrometer is fitted with an Rhodium tube and with the following analytical crystals: LIF200, LIF220, PE002, GE111 and PX1. The instrument is fitted with a gas-flow proportional counter and a scintillation detector. The gas flow-flow proportional counter uses a 90% Ar to 10% methane gas mixture. Major element analysis was carried out using a fused glass disk, using a 2.4kW Rhodium tube. The matrix effects in the samples were corrected for by applying theoretical alpha factors and measured line overlap factors to the raw intensities measured with the SuperQ PANalytical software. The concentration of the control standards that were used in the calibration procedures for major element analysis, fit the range of concentration of the samples.

i.v. Electron Probe Microanalysis (EPMA)

Quantitative mineral chemical analyses were obtained by using four wavelength dispersive spectrometers on a JEOL JXA-8230 electron probe micro-analyzer at Rhodes University. The beam was generated by a Tungsten cathode; 15 kV accelerating potential, and 20 nA current. A 1µm beam size was applied; on beam sensitive phases up to 20µm was used. All elements were measured on K-alpha peaks, except for Sr and Ba on L-alpha. Manganese and Fe was measured on high resolution LIFL crystals. Counting times on peaks were 10s, and 10s total on backgrounds. Commercial "SPI" standards were used for intensity calibration. The standards for Mn-bearing silicates and oxides were Almandine (Si), Plagioclase (Al), Pyrope (Ca, Mg, Fe), Hematite (Fe), Metallic Manganese (Mn), and Barite (Ba). Additional standards for other silicates and carbonates were Plagioclase (Ca, Si, Al), Orthoclase (K), Celestite (Sr), Jadeite (Na), Rhodonite (Mn), MgF_2 (F), Kaersutite (Mg, Fe, Ti), and Dolomite (Ca, Mg). The data was collected with JEOL software. An automated ZAF matrix algorithm was applied to correct for differential matrix effects. Oxygen was calculated by stoichiometry. Carbon was not measured.

Appendix III

EPMA Data

Table A: Electron Microprobe data for aegirine.

	Oxide wt.%									Cations calculated on the basis of 6 O							
Sample Number	SiO_2	Al_2O_3	Fe_2O_3	MnO	MgO	CaO	Na_2O	K_2O	Total	Si	Al	Fe	Mn	Mg	Ca	Na	K
002B_12.2	52.59	1.91	32.26	0.52	0.18	0.18	12.45	0.03	100.13	2.00	0.09	0.92	0.02	0.01	0.01	0.92	0.00
002B_12.2	51.77	1.27	32.44	1.03	0.31	0.71	12.22	0.02	99.76	1.99	0.06	0.94	0.03	0.02	0.03	0.91	0.00
002B_12.2	51.98	1.27	32.41	0.93	0.37	0.73	12.18	0.03	99.90	1.99	0.06	0.93	0.03	0.02	0.03	0.90	0.00
002B_12.2	52.42	1.28	32.35	0.92	0.32	0.70	12.25	0.02	100.26	2.00	0.06	0.93	0.03	0.02	0.03	0.91	0.00
Average	52.11	1.49	32.37	0.83	0.29	0.54	12.28	0.03	99.93	1.99	0.06	0.93	0.03	0.02	0.02	0.91	0.00
Std. Dev.	0.43	0.37	0.09	0.27	0.10	0.31	0.14	0.01	0.18								
Minimum	51.77	1.27	32.26	0.52	0.18	0.18	12.18	0.02	99.76								
Maximum	52.59	1.91	32.44	1.03	0.37	0.73	12.45	0.03	100.13								

Table B: Electron Microprobe data for banalsite.

	Oxide wt. %									Cations calculated on the basis of 16 O							
Sample number	SiO_2	Al_2O_3	FeO	MnO	BaO	Na_2O	TiO_2	K_2O	Total	Si	Al	Fe	Mn	Ba	Na	Ti	K
002B_9	36.86	29.61	0.21	0.14	22.96	9.23	0.26	0.05	99.32	4.07	3.86	0.02	0.01	0.99	1.98	0.02	0.01
002B_9	37.06	29.51	0.40	0.15	22.64	8.83	0.20	0.04	98.81	4.10	3.85	0.04	0.01	0.98	1.90	0.02	0.01
002B_9	37.70	29.64	0.27	0.23	22.42	8.88	0.23	0.10	99.46	4.13	3.83	0.02	0.02	0.96	1.89	0.02	0.01
Average	37.20	29.59	0.29	0.17	22.67	8.98	0.23	0.06	99.23	4.10	3.85	0.03	0.02	0.98	1.92	0.02	0.01
Std. Dev.	0.44	0.07	0.09	0.05	0.27	0.22	0.03	0.03	0.36								
Minimum	36.86	29.51	0.21	0.14	22.42	8.83	0.20	0.04	98.83								
Maximum	37.70	29.64	0.40	0.23	22.96	9.23	0.26	0.10	99.53								

Table C: Electron Microprobe data for barite.

	Oxide wt.%					Cations calculated on the basis of 4 O			
Sample number	SO_3	BaO	CaO	SrO	Total	S	Ba	Ca	Sr
017A_9	33.49	65.23	n.d.	0.65	99.38	0.99	1.01	0.00	0.01
017A_9	33.55	65.06	0.02	1.05	99.68	0.99	1.00	0.00	0.02
017A_9	33.58	65.57	0.02	0.24	99.40	0.99	1.01	0.00	0.01
Average	33.54	65.29	0.02	0.65	99.48	0.99	1.01	0.00	0.01
Std. Dev.	0.04	0.26	0.00	0.41	0.17				
Minimum	33.49	65.06	<0.02	0.24	99.38				
Maximum	33.58	65.57	0.02	1.05	99.68				

Table D: Electron Microprobe data for barytocalcite.

	Oxide wt.%						Cations calculated on the basis of 1 CO_3			
Sample number	MnO	BaO	CaO	SrO	CO_2	Total	Mn	Ba	Ca	Sr
537_9.1	n.d.	47.52	17.89	0.89	32.15	66.30	0.00	0.49	0.50	0.01
537_9.1	n.d.	47.26	17.71	0.85	32.22	65.82	0.00	0.49	0.50	0.01
537_9.2	0.05	48.74	18.36	0.96	32.18	68.15	0.00	0.49	0.50	0.01
537_13.1	0.01	49.49	18.56	1.17	30.90	69.23	0.00	0.49	0.50	0.02
537_13.1	0.08	48.72	17.98	1.24	31.50	68.04	0.00	0.49	0.49	0.02
Average	0.05	48.34	18.10	1.02	31.79	67.51	0.00	0.49	0.50	0.02
Std. Dev.	0.03	0.93	0.35	0.18	0.58	1.41				
Minimum	<0.01	47.26	17.71	0.85	30.90	65.82				
Maximum	0.08	49.49	18.56	1.24	32.22	69.23				

Table E: Electron Microprobe data for braunite.

	Oxide wt.%								Cations calculated on the basis of 12 O						
Sample number	SiO_2	Al_2O_3	Mn_2O_3	Fe_2O_3	MgO	CaO	BaO	Total	Si	Al	Mn	Fe	Mg	Ca	Ba
002B_9	8.99	0.63	78.67	7.60	0.03	1.20	0.11	97.23	0.91	0.07	6.05	0.58	0.00	0.13	0.00
002B_9	9.14	0.45	80.78	6.32	0.04	1.36	0.25	98.32	0.91	0.05	6.15	0.48	0.01	0.15	0.01
002B_9	9.05	0.52	80.54	5.57	0.02	1.13	0.21	97.04	0.92	0.06	6.20	0.42	0.00	0.12	0.01
002B_9	8.88	1.17	81.04	4.98	0.06	1.11	0.11	97.35	0.89	0.14	6.21	0.38	0.01	0.12	0.00
002B_9	9.18	0.33	81.58	6.68	0.04	1.29	0.19	99.29	0.91	0.04	6.15	0.50	0.01	0.14	0.01
Average	9.05	0.62	80.52	6.23	0.04	1.22	0.18	97.85	0.91	0.07	6.15	0.47	0.01	0.13	0.01
Std. Dev.	0.12	0.33	1.10	1.01	0.02	0.11	0.06	0.95							
Minimum	8.88	0.33	78.67	4.98	0.02	1.11	0.11	97.04							
Maximum	9.18	1.17	81.58	7.60	0.06	1.36	0.25	99.29							

Table F: Electron Microprobe data for calcite.

	Oxide wt. %								Cations calculated on the basis of 1 CO_3					
Sample number	CaO	FeO	MnO	MgO	BaO	SrO	CO_2	Total	Ca	Fe	Mn	Mg	Ba	Sr
537_9.1	51.08	0.06	0.28	0.02	0.14	0.65	46.50	98.72	0.99	0.00	0.00	0.00	0.00	0.01
537_9.1	51.35	0.03	0.28	0.03	0.02	0.28	46.72	98.71	0.99	0.00	0.00	0.00	0.00	0.00
537_9.1	50.90	n.d.	0.19	0.01	0.11	0.34	46.55	98.12	0.99	0.00	0.00	0.00	0.00	0.00
537_9.1	51.12	0.09	0.25	0.01	0.09	0.42	46.40	98.38	0.99	0.00	0.00	0.00	0.00	0.00
Average	51.11	0.06	0.25	0.02	0.09	0.42	46.30	98.48	0.99	0.00	0.00	0.00	0.00	0.00
Std. Dev.	0.18	0.03	0.04	0.01	0.05	0.16	0.134	0.29						
Minimum	50.90	<0.03	0.19	0.01	0.02	0.28	46.40	98.12						
Maximum	51.35	0.09	0.28	0.03	0.14	0.65	46.72	98.72						

Table G: Electron Microprobe data for witherite.

	Oxide wt. %						Cations calculated on the basis of 1 CO_3			
Sample number	BaO	FeO	CaO	SrO	CO_2	Total	Fe	Ca	Ba	Sr
537_13.1	71.72	<0.002	0.42	0.22	27.20	99.56	0.00	0.02	0.98	0.00
537_13.1	69.54	n.d.	0.34	1.75	27.30	98.92	0.00	0.01	0.95	0.04
537_13.1	70.05	0.06	0.33	2.35	27.15	99.94	0.00	0.01	0.94	0.05
537_13.1	71.06	0.09	0.41	0.97	27.10	99.63	0.00	0.02	0.96	0.02
Average	70.59	0.07	0.38	1.32	27.19	99.51	0.00	0.01	0.96	0.03
Std. Dev.	0.98	0.03	0.05	0.93	0.09	0.43				
Minimum	69.54	<0.002	0.33	0.22	27.10	98.92				
Maximum	71.72	0.09	0.42	2.35	27.30	99.94				

Table H: Electron Microprobe data for natrolite.

	Oxide wt. %									Cations calculated on the basis of 10 O							
Sample number	SiO_2	Al_2O_3	FeO	CaO	BaO	K_2O	Na_2O	F	Total	Si	Al	Fe	Ca	Ba	K	Na	F
537_9.1	51.64	25.41	0.16	<0.021	n.d.	0.06	13.14	0.01	90.43	3.20	1.86	0.01	0.00	0.00	0.00	1.58	0.00
537_9.1	51.34	25.41	0.12	<0.001	0.05	0.07	13.40	0.02	90.41	3.19	1.86	0.01	0.00	0.00	0.01	1.62	0.01
537_9.1	51.58	25.38	0.15	0.01	<0.001	0.06	13.31	n.d.	90.49	3.20	1.86	0.01	0.00	0.00	0.00	1.60	0.00
537_9.1	51.63	25.46	0.28	0.02	0.03	0.07	12.67	0.12	90.28	3.21	1.87	0.01	0.00	0.00	0.01	1.53	0.04
537_9.1	51.62	25.58	0.38	<0.007	0.02	0.04	12.54	n.d.	90.17	3.21	1.87	0.02	0.00	0.00	0.00	1.51	0.00
537_9.1	51.38	25.49	0.16	0.03	0.01	0.08	13.00	n.d.	90.15	3.20	1.87	0.01	0.00	0.00	0.01	1.57	0.00
Average	51.53	25.46	0.21	0.02	0.03	0.06	13.01	0.05	90.32	3.20	1.86	0.01	0.00	0.00	0.00	1.57	0.01
Std. Dev.	0.13	0.07	0.10	0.01	0.02	0.01	0.35	0.06	0.14								
Minimum	51.34	25.38	0.12	<0.001	<0.001	0.04	12.54	<0.01	90.15								
Maximum	51.64	25.58	0.38	0.03	0.05	0.08	13.40	0.12	90.49								

Table I: Electron Microprobe data for serandite.

	Oxide wt. %											Cations calculated on the basis of 8.5 O								
Sample Number	SiO_2	Al_2O_3	FeO	MnO	MgO	CaO	Na_2O	K_2O	F	H_2O	Total	Si	Al	Fe	Mn	Mg	Ca	Na	K	F
537_14	53.15	0.01	0.45	29.19	0.04	9.01	6.46	0.02	n.d.	2.76	101.09	2.88	0.00	0.02	1.34	0.00	0.52	0.68	0.00	0.00
537_14	52.39	0.03	1.01	32.67	0.03	5.61	7.26	0.03	n.d.	2.74	101.77	2.86	0.00	0.05	1.51	0.00	0.33	0.77	0.00	0.00
537_14	52.88	0.01	0.28	32.39	0.01	6.40	6.92	0.01	0.12	2.75	101.77	2.88	0.00	0.01	1.49	0.00	0.37	0.73	0.00	0.04
537_14	53.36	0.01	0.28	28.48	0.02	9.81	6.82	0.02	0.03	2.76	101.61	2.88	0.00	0.01	1.30	0.00	0.57	0.71	0.00	0.01
537_11	52.39	0.00	0.21	30.58	0.01	7.42	7.20	0.05	n.d.	2.73	100.58	2.87	0.00	0.01	1.42	0.00	0.44	0.77	0.00	0.00
Average	52.83	0.01	0.45	30.66	0.02	7.65	6.93	0.03	0.03	2.75	101.36	2.88	0.00	0.02	1.41	0.00	0.45	0.73	0.00	0.01
Std. Dev.	0.44	0.01	0.33	1.87	0.01	1.76	0.32	0.01	0.05	0.01	0.52									
Minimum	52.39	0.00	0.21	28.48	0.01	5.61	6.46	0.01	<0.03		100.58									
Maximum	53.36	0.03	1.01	32.67	0.04	9.81	7.26	0.05	0.12		101.77									

Table J: Electron Microprobe data for fluorapatite.

	Oxide wt. %							Cations calculated on the basis of 13 O					
Sample number	P_2O_5	CaO	FeO	MnO	F	SrO	Total	P	Ca	Fe	Mn	F	Sr
537_9.1	41.52	53.91	0.04	0.02	3.88	1.34	100.71	3.12	5.13	0.00	0.00	1.88	0.07
537_9.1	41.27	53.50	0.01	n.d.	4.12	1.17	100.08	3.12	5.13	0.00	0.00	2.01	0.06
537_9.1	41.41	53.24	0.09	0.02	3.90	1.32	99.97	3.13	5.10	0.01	0.00	1.90	0.07
537_13.1	39.61	52.32	0.04	0.08	5.07	2.52	99.64	3.08	5.15	0.00	0.01	2.54	0.13
Average	40.95	53.24	0.05	0.04	4.24	1.59	100.10	3.11	5.12	0.00	0.00	2.08	0.08
Std. Dev.	0.90	0.67	0.03	0.03	0.56	0.63	0.45						
Minimum	39.61	52.32	0.01	<0.02	3.88	1.17	99.64						
Maximum	41.52	53.91	0.09	0.08	5.07	2.52	100.71						

Table K: Electron Microprobe data for K-feldspar.

	Oxide wt. %									Cations calculated on the basis of 8 O							
Sample number	SiO_2	Al_2O_3	Fe_2O_3	Mn_2O_3	CaO	Na_2O	F	K_2O	Total	Si	Al	Fe	Mn	Ca	Na	F	K
537_11	67.93	17.61	0.27	0.01	n.d.	0.17	n.d.	12.82	98.81	3.10	0.95	0.01	0.00	0.00	0.02	0.00	0.75
537_11	68.03	18.02	0.40	0.02	n.d.	0.11	n.d.	13.09	99.68	3.08	0.96	0.02	0.00	0.00	0.01	0.00	0.76
537_11	68.37	18.00	0.22	0.02	0.01	0.05	0.05	13.06	99.79	3.09	0.96	0.01	0.00	0.00	0.00	0.01	0.75
537_11	67.83	17.93	0.19	0.06	0.02	0.06	0.12	13.82	100.04	3.07	0.96	0.01	0.00	0.00	0.01	0.03	0.80
Average	68.04	17.89	0.27	0.03	0.01	0.10	0.09	13.20	99.58								
Std. Dev.	0.24	0.19	0.09	0.02	0.01	0.06	0.05	0.43	0.53								
Minimum	67.83	17.61	0.19	0.01	<0.01	0.05	<0.05	12.82	98.81								
Maximum	68.37	18.02	0.40	0.06	0.02	0.17	0.12	13.82	100.04								

Table L: Electron Microprobe data for hyalophane.

	Oxide wt. %									Cations calculated on the basis of 8 O							
Sample number	SiO_2	TiO_2	Al_2O_3	Fe_2O_3	Mn_2O_3	BaO	Na_2O	K_2O	Total	Si	Ti	Al	Fe	Mn	Ba	Na	K
002B_14	43.26	0.31	23.05	0.27	n.d.	27.25	0.17	5.70	100.00	2.43	0.01	1.53	0.01	0.00	0.60	0.02	0.41
002B_14	43.18	0.23	23.12	0.27	0.01	27.59	0.13	5.72	100.25	2.43	0.01	1.53	0.01	0.00	0.61	0.01	0.41
002B_14	43.51	0.24	23.51	0.11	0.04	27.41	0.11	5.90	100.83	2.42	0.01	1.54	0.01	0.00	0.60	0.01	0.42
Average	43.31	0.26	23.23	0.22	0.03	27.42	0.13	5.77	100.36	2.43	0.01	1.53	0.01	0.00	0.60	0.01	0.41
Std. Dev.	0.17	0.04	0.25	0.09	0.02	0.17	0.03	0.11	0.42								
Minimum	43.18	0.23	23.05	0.11	<0.01	27.25	0.11	5.70	100.00								
Maximum	43.51	0.31	23.51	0.27	0.04	27.59	0.17	5.90	100.83								

Table M: Electron Microprobe data for kutnohorite.

	Oxide wt. %									Cations calculated on the basis of 2 CO_3						
Sample number	SiO_2	Al_2O_3	Fe_2O_3	MnO	MgO	CaO	BaO	CO_2	Total	Si	Al	Fe	Mn	Mg	Ca	Ba
002B_5	n.d.	0.01	0.64	15.84	0.80	42.31	0.02	40.30	99.92	0.00	0.00	0.02	0.63	0.06	2.12	0.00
002B_5	0.03	0.04	1.51	16.46	0.76	40.06	0.03	41.36	100.25	0.00	0.00	0.05	0.65	0.05	1.99	0.00
002B_5	0.59	0.07	1.33	16.19	0.72	38.66	0.01	41.75	99.31	0.03	0.00	0.05	0.63	0.05	1.92	0.00
Average	0.31	0.04	1.16	16.16	0.76	40.34	0.02	41.14	99.83	0.01	0.00	0.04	0.64	0.05	2.01	0.00
Std. Dev.	0.40	0.03	0.46	0.31	0.04	1.84	0.01	0.75	0.48							
Minimum	<0.01	0.01	0.64	15.84	0.72	38.66	0.01	40.30	99.31							
Maximum	0.59	0.07	1.51	16.46	0.80	42.31	0.03	41.75	100.25							

Table N: Electron Microprobe data for hollandite.

	Oxide wt %					Cations calculated on basis of 16 O			
Sample number	Fe_2O_3	MnO_2	BaO	CaO	Total	Fe	Mn	Ba	Ca
002B_19	0.24	82.93	17.29	0.14	100.60	0.02	7.53	0.89	0.02
002B_19	0.19	80.52	16.95	0.15	97.81	0.02	7.53	0.90	0.02
002B_19	0.15	81.89	15.88	0.17	98.09	0.01	7.56	0.83	0.02
002B_19	0.13	81.15	16.44	0.18	97.90	0.01	7.54	0.87	0.03
002B_19	0.15	81.41	16.46	0.17	98.19	0.02	7.54	0.86	0.02
Average	0.16	16.60	0.17	81.58	98.52	0.02	7.54	0.87	0.02
Std. Dev.	0.02	0.54	0.04	0.90	1.17				
Minimum	0.14	15.88	0.13	80.52	97.81				
Maximum	0.18	17.29	0.24	82.93	100.60				

Appendix IV

Bulk-rock geochemistry – raw data

Table O: Ore-zone major elements.

Sample No.	Fe_2O_3	Mn_3O_4	TiO_2	CaO	K_2O	P_2O_5	SiO_2	Al_2O_3	MgO	Na_2O	LOI	Total
Wt. %												
002B/1	82.90	4.96	0.27	0.17	0.75	0.05	5.83	3.76	0.18	0.03	1.52	100.41
002B/2	91.93	1.85	0.12	0.25	0.43	0.08	2.82	1.71	0.10	0.03	1.14	100.45
002B/3	90.25	1.99	0.15	0.31	0.57	0.08	4.38	2.07	0.18	0.03	1.18	101.18
002B/4	92.08	1.56	0.21	0.17	0.54	0.05	3.80	2.08	0.09	0.02	0.89	101.47
002B/5	91.76	1.82	0.20	0.49	0.40	0.05	3.70	1.55	0.15	0.02	1.40	101.55
002B/6	83.72	2.09	0.19	1.10	0.55	0.05	8.75	1.98	0.40	0.03	2.04	100.88
573/1	97.70	0.25	0.11	0.09	0.23	0.06	1.49	1.18	bdl	0.03	0.42	101.56
537/2	95.90	0.25	0.17	0.07	0.49	0.04	6.93	2.04	0.04	0.07	0.57	106.56
537/3	86.86	0.79	0.17	0.08	0.40	0.04	10.19	1.66	0.06	0.02	0.72	100.98
537/4	68.94	0.41	0.15	0.17	0.46	0.10	26.66	1.68	0.08	0.02	2.37	101.03
537/5	68.24	1.53	0.16	0.07	0.43	0.04	27.67	1.60	0.02	0.01	0.59	100.36
537/6	72.69	0.54	0.12	0.09	0.71	0.06	23.52	2.47	0.08	0.04	0.63	100.94
017A/1	86.71	0.22	0.61	0.03	0.14	0.10	6.49	5.15	bdl	0.01	1.71	101.16
017A/2	92.61	0.18	0.27	0.03	0.71	0.11	3.68	3.15	bdl	0.07	0.67	101.46
017A/3	89.48	0.23	0.62	0.03	1.05	0.09	5.15	4.19	bdl	0.03	0.75	101.61

Table P: Ore-zone trace elements.

Sample No.	V	Cr	Co	Ni	Cu	Zn	Rb	Sr	Y	Cs	Ba	Pb	U
ppm													
002B/1	67.05	68.70	25.80	45.90	15.45	34.95	18.35	12.93	8.09	1.75	327.50	29.20	1.42
002B/2	41.27	47.45	11.27	29.47	10.71	15.39	11.32	21.46	6.08	1.39	1697.61	11.05	0.85
002B/3	45.80	48.30	13.70	32.40	10.40	26.70	20.55	16.75	9.67	2.83	567.50	17.40	0.95
002B/4	70.43	57.60	15.19	37.00	13.94	15.28	13.47	10.87	9.49	1.25	117.20	20.19	1.12
002B/5	49.57	47.04	10.57	29.10	8.70	15.59	12.21	11.84	8.67	2.05	158.02	17.48	0.80
002B/6	61.80	60.75	15.62	37.70	19.50	21.30	19.75	19.25	8.88	3.21	240.05	23.80	1.05
537/1	54.02	30.58	4.92	24.07	8.61	11.07	3.62	11.65	2.54	0.38	624.67	7.02	0.36
537/2	118.22	104.49	17.46	62.78	31.08	38.41	28.13	20.33	15.07	2.60	267.74	28.24	1.57
537/3	76.40	55.10	19.50	43.45	12.39	22.80	13.89	13.78	11.76	1.17	600.50	21.25	1.54
537/4	60.55	57.10	11.05	40.10	28.00	16.55	17.35	11.27	9.10	1.45	200.05	15.62	0.80
537/5	75.05	68.55	18.30	37.00	17.95	26.15	15.95	18.70	13.43	1.17	2172.50	18.45	0.98
537/6	48.95	58.55	10.36	39.95	15.00	15.40	24.85	10.56	7.97	1.40	196.90	14.09	0.70
017A/1	107.25	107.65	4.54	26.70	11.15	10.35	3.61	482.75	13.74	0.39	71.75	18.60	1.28
017A/2	65.50	79.60	3.82	20.85	7.85	10.90	13.35	426.50	9.84	0.65	72.80	11.34	0.73
017A/3	105.55	97.10	5.90	24.30	10.00	13.65	19.30	292.50	18.16	0.60	89.10	17.67	1.47

Table Q: Enriched-zone major elements.

Sample No. Wt. %	Fe_2O_3	MnO_2	TiO_2	CaO	K_2O	P_2O_5	SiO_2	Al_2O_3	MgO	Na_2O	LOI	Total
002B/9	38.15	48.28	bdl	1.05	0.40	0.10	8.89	2.73	0.42	bdl	1.22	101.24
002B/12.1	27.88	0.24	0.10	4.63	0.03	0.19	43.37	6.40	0.21	10.99	5.17	99.20
002B/15.2	39.51	0.28	0.19	0.99	1.56	0.05	41.22	4.85	0.41	8.29	1.22	98.58
002B/19	33.68	16.06	0.60	5.95	3.26	0.06	18.40	6.47	0.64	0.13	8.58	93.84
537/8.1	63.52	6.32	0.11	0.22	0.33	0.04	21.58	1.62	0.07	4.82	0.54	99.18
537/9.2	28.88	0.39	0.29	11.17	0.74	0.09	35.30	5.61	0.88	6.63	9.12	99.10
537/10	10.21	58.49	0.03	1.71	0.00	0.01	22.95	0.77	0.04	3.90	1.19	99.30
537/12	21.29	52.78	0.17	1.63	0.20	0.03	12.13	3.88	0.39	1.63	2.68	96.81
017A/5.1	55.46	0.48	0.24	0.17	0.01	0.09	30.48	3.92	0.00	6.81	0.57	99.01
017A/6	22.84	0.25	0.09	0.22	0.98	0.16	40.26	11.06	bdl	7.20	6.39	89.45
017A/11	24.60	22.90	0.51	1.01	1.37	0.08	23.60	13.33	0.91	4.11	2.78	95.19
017A/14	11.85	14.08	0.22	15.05	0.81	0.03	29.36	6.29	2.19	3.80	14.77	98.47

Table R: Enriched-zone trace elements.

Sample No. ppm	V	Cr	Co	Ni	Cu	Zn	Rb	Sr	Y	Cs	Ba	Pb	U
002B/9	43.67	45.75	49.55	43.45	637.90	59.35	16.28	103.55	19.85	2.17	5150.50	567.00	1.03
002b/12.1	71.65	30.75	6.12	23.05	39.75	39.90	1.02	441.35	4.46	5.01	991.50	42.20	0.19
002b/15.2	40.35	150.55	8.94	29.75	57.15	38.90	18.57	153.35	5.00	0.25	16545.00	180.95	2.15
002B/19	77.74	101.10	19.49	61.80	97.40	66.05	64.65	41.62	23.01	4.32	29545.00	1200.00	1.47
537/8.1	92.83	216.30	12.67	30.10	43.55	26.15	4.16	38.19	34.10	0.29	4737.00	34.69	1.19
537/9.2	44.11	175.55	16.98	75.25	23.50	27.50	10.66	265.75	18.09	0.52	8456.50	193.35	2.23
537/10	25.70	72.00	33.20	63.10	334.75	46.45	0.44	73.20	17.99	0.10	6550.00	83.25	1.19
537/12	66.60	34.90	33.20	31.80	94.60	86.10	13.52	464.95	25.72	0.99	25660.00	675.00	0.60
017A/5.1	207.25	143.25	13.76	37.55	29.25	19.60	0.80	37.62	11.44	0.10	4039.00	38.52	2.60
017A/6	60.17	57.55	4.64	22.15	28.81	40.70	13.78	137.45	12.45	19.56	37060.00	11.77	0.48
017A/11	64.85	84.35	25.03	62.30	40.65	73.75	48.95	1284.00	23.54	23.63	34740.00	938.00	1.45
017A/14	36.02	83.65	55.25	164.25	58.90	37.55	47.85	213.65	29.98	4.34	875.00	35.29	1.60

Table S: Ore-zone Rare Earth Elements

Sample No. ppm	La	Ce	Pr	Nd	Sm	Eu	Gd	Tb	Dy	Ho	Er	Tm	Yb	Lu
002B/1	15.94	40.60	2.27	8.23	1.63	0.30	1.27	0.18	1.51	0.25	0.75	0.10	0.95	0.11
002B/2	7.16	25.96	1.70	5.80	1.18	0.39	1.13	0.16	1.06	0.23	0.61	0.10	0.55	0.12
002B/3	13.75	28.20	2.81	9.90	2.60	0.44	2.16	0.21	2.50	0.31	1.26	0.17	0.68	0.16
002B/4	14.31	23.76	3.16	10.28	2.91	0.65	2.23	0.39	1.71	0.37	1.03	0.19	1.42	0.21
002B/5	12.55	19.32	2.61	9.40	2.11	0.39	1.66	0.29	1.80	0.31	0.91	0.18	1.18	0.16
002B/6	12.41	24.89	2.03	7.49	1.61	0.36	1.34	0.23	1.53	0.31	1.04	0.12	1.04	0.15
537/1	6.28	15.01	1.08	3.99	0.75	0.21	0.71	0.09	0.60	0.09	0.23	0.04	0.34	0.05
537/2	32.11	59.14	6.78	25.24	4.66	0.93	2.48	0.42	2.65	0.61	1.87	0.42	2.24	0.42
537/3	15.22	26.24	3.50	13.35	2.62	0.60	2.08	0.34	2.34	0.45	1.39	0.18	1.39	0.18
537/4	11.20	25.34	2.66	10.27	1.99	0.45	2.26	0.28	1.85	0.35	1.02	0.14	1.04	0.13
537/5	14.85	31.55	3.68	14.95	3.05	0.80	3.24	0.46	3.03	0.58	1.40	0.23	1.20	0.18
537/6	8.65	17.52	1.96	7.27	1.58	0.36	1.44	0.20	1.30	0.30	0.85	0.10	0.79	0.12
017A/1	28.31	53.20	5.78	20.55	3.50	0.58	2.60	0.41	2.50	0.46	1.69	0.25	2.38	0.38
017A/2	20.00	54.65	5.01	17.25	3.45	0.72	1.87	0.33	2.10	0.28	0.96	0.22	1.76	0.23
017A/3	28.35	74.55	5.85	23.70	4.12	1.09	3.52	0.52	3.32	0.71	2.08	0.36	2.39	0.41

Table T: Enriched-zone Rare Earth Elements

Sample No. ppm	La	Ce	Pr	Nd	Sm	Eu	Gd	Tb	Dy	Ho	Er	Tm	Yb	Lu
002B/12.1	3.56	8.52	0.872	3.535	0.9615	0.2345	1.205	0.1145	0.665	0.1245	0.3935	0.063	0.37	0.0445
002B/15.2	9.38	17.45	1.303	4.635	0.86	1.2	0.7	0.0955	0.72	0.1495	0.4145	0.0695	0.71	0.1235
002B/9	12.675	16.31	3.24	14.41	2.825	1.043	3.21	0.363	2.26	0.387	1.15	0.122	0.785	0.127
002B/19	13.49	19.33	2.715	12.495	3.495	2.74	4.985	0.7665	5.025	0.887	2.6	0.325	2.18	0.3385
537/8.1	14.86	39.15	9.163	42.25	7.41	1.82	5.625	0.8615	5.115	1.065	2.85	0.364	2.19	0.303
537/9.2	55.425	35.08	3.985	12.505	1.94	0.93	2.11	0.325	2.135	0.5255	1.515	0.213	1.445	0.225
537/10	2.025	4.335	0.941	4.56	1.29	0.92	2.195	0.328	2.02	0.452	1.035	0.1115	0.575	0.0685
537/12	6.25	14.68	1.2935	5.47	1.38	2.13	2.43	0.4035	2.46	0.5855	1.695	0.226	1.515	0.2685
017A/5.1	11.025	24.04	2.22	9.51	2.01	0.8125	2.655	0.32	2.495	0.432	1.175	0.1855	1.37	0.232
017A/6	6.1	10.62	1.596	7.595	2.255	2.73	3.32	0.469	2.665	0.4305	0.965	0.087	0.545	0.081
017A/11	50.37	54.35	7.93	27.4	4.28	3.03	4.57	0.7075	4.1	0.777	2.2	0.262	1.93	0.304
017A/14	24.55	49.935	6.335	26.695	5.39	1.175	4	0.562	3.43	0.82	2.18	0.3225	1.88	0.251